Christoph Lercher

Surface Induced Polymorphism of Dioctyl-Terthiophene on Silicon Oxide

MASTER THESIS

For obtaining the academic degree
Diplom-Ingenieur

Master Programme of
Technical Physics

Graz University of Technology

Supervisor:

Ao.Univ.-Prof. Dipl.-Ing. Dr.techn. Roland Resel
Institute of Solid State Physics
Graz University of Technology

Graz, June 2013

Deutsche Fassung:
Beschluss der Curricula-Kommission für Bachelor-, Master- und Diplomstudien vom 10.11.2008
Genehmigung des Senates am 1.12.2008

EIDESSTATTLICHE ERKLÄRUNG

Ich erkläre an Eides statt, dass ich die vorliegende Arbeit selbstständig verfasst, andere als die angegebenen Quellen/Hilfsmittel nicht benutzt, und die den benutzten Quellen wörtlich und inhaltlich entnommenen Stellen als solche kenntlich gemacht habe.

Graz, am ……. ……..
(Unterschrift)

Englische Fassung:

STATUTORY DECLARATION

I declare that I have authored this thesis independently, that I have not used other than the declared sources / resources, and that I have explicitly marked all material which has been quoted either literally or by content from the used sources.

……. ……..
date (signature)

Abstract

Despite the recent commercial breakthrough of organic semiconductor thin film applications, the complex mechanisms during thin film growth remain a limiting factor for the achievable performance. It is well known that the inorganic/organic interface and the first few layers of the active material have a tremendous effect on the overall device performance. However, the possibility to influence this interface by the systematic selection of different polymorphs has only been studied for a few systems. In this work, sub-monolayer, monolayer and multilayer films of the model organic semiconductor dioctyl-terthiophene are investigated. X-ray reflectivity and grazing incidence X-ray diffraction techniques are used to gain inside into the morphology, the crystal structure and the alignment of the molecules on an isotropic silicon oxide substrate. The formation of different polymorphs as a function of the film thickness and film preparation parameters is investigated. Optical and atomic force microscopy are employed to complement the results. Four polymorphic phases are found: Directly on the substrate, a monolayer of upright standing molecules is formed. On top of the monolayer the already known b-, as well as the s-phase are present. The preferential crystallization of one or the other phase can be tuned by changing the temperature during the spin-coating process. At high temperatures, the s-phase is favored, while a majority of b-phase is found at low temperatures. Annealing experiments, where the sample is heated above the transition temperature to the smectic G phase and cooled down to room temperature subsequently, demonstrate that the s-phase is predominant at high cooling rates whereas the b-phase is formed at low cooling rates. Predictions about the thermodynamic stability can be made, by comparing the surface induced phases with a single crystal phase.

Key words: polymorphism, surface induced phase, organic semiconductor, thin film, X-ray reflectivity, grazing incidence X-ray diffraction.

Oberflächeninduzierter Polymorphismus von Dioctyl-Terthiophen auf Siliziumoxid

Kurzfassung

Auch nach dem kürzlich erfolgten kommerziellen Durchbruch von Anwendungen auf der Basis von organischen Dünnschichten, bleiben die komplexen Vorgänge beim Filmwachstum ein limitierender Faktor für die erreichbare Leistung. Dabei spielen vor allem die Grenzfläche zwischen anorganischem Substrat und organischem Material und die darauf folgenden ersten Schichten eine wesentliche Rolle. Trotzdem wurde die Möglichkeit, diese entscheidenden Bereiche durch die systematische Wahl von unterschiedlichen polymorphen Phasen zu beeinflussen, erst für wenige Systeme untersucht. In dieser Arbeit werden Submonolagen, Monolagen und dünne Schichten des organischen Halbleiters Dioctyl-Terthiophen analysiert. Morphologie, Kristallstruktur sowie die Orientierung der Moleküle auf einer isotropen Siliziumoxidprobe werden mithilfe der Methoden der Röntgenreflektivität und der Röntgendiffraktometrie mit streifendem Einfall näher betrachtet. Durch unterschiedliche Schichtdicken und veränderte Parameter während und nach der Probenherstellung wird versucht, die Bildung von polymorphen Phasen zu verstehen. Ergänzend kommen optische Mikroskopie und Rasterkraftmikroskopie zum Einsatz. Es werden vier polymorphe Phasen gefunden: Direkt auf der Probenoberfläche wächst die ml-Phase, welche aus einer Monolage mit aufrecht stehenden Molekülen besteht. In weiterer Folge bilden sich auf dieser Monolage die bereits bekannten b- und s-Phasen aus. Indem die Temperatur während des Spin-coating verändert wird, kann gesteuert werden in welcher Phase die weiteren Schichten kristallisieren. Bei niedrigen Temperaturen wird die b-Phase bevorzugt. Dagegen findet man bei höheren Temperaturen hauptsächlich die s-Phase. Durch Aufheizen der Probe über die Temperatur des Phasenübergangs zur crystal-G Phase und anschließendes Abkühlen, wird die Entstehung der Phasen bei unterschiedlichen Kühlraten untersucht. Wieder findet man bei niedriger Kühlrate durchwegs die b-Phase und bei hoher Kühlrate verstärkt die s-Phase. Schließlich ermöglicht ein Vergleich von oberflächeninduzierten Phasen mit einer Einkristallphase Aussagen über die jeweilige thermodynamische Stabilität.

Schlagwörter: Polymorphismus, oberflächeninduzierte Phase, organischer Halbleiter, Dünnfilm, Röntgenreflektivität, Röntgendiffraktometrie mit streifendem Einfall.

Contents

1. Introduction

1.1. Thin films

The preparation of thin films has become a tremendously important technology in the last century. Numerous applications are based on the deposition of a small amount of material on a substrate.

In a first step, the interesting optical properties of thin films were used to make high reflective mirrors and antireflective films. The decorative appearance of those films soon brought them into everyday life as metal coating on glass and other materials. Furthermore the protection of substrates against corrosion and wear with metal films became a common application. Thin film technology also became a necessary tool for the miniaturization of electronic semiconductor devices.

Since the late 70s organic semiconductors are a growing field [1]. Thin films of organic molecules are used as active layer in electronic devices. Therefore the fabrication and characterization of those films made the adaptation of already available techniques necessary.

In the following sections I will give an overview of the different processes and show the different modes how films can grow on a substrate.

1.1.1. Deposition Processes

Because of the huge number of materials, from metals to organic molecules, and the different requirements for the various applications, a number of deposition processes has been developed. Different schemes for grouping them exist but since there are always overlaps and combinations of different processes no one right scheme can be given. I will follow the classification used by Peter M. Martin in his Handbook of Deposition Technologies [2]:

- Conduction and diffusion processes
- Chemical processes
- Wetting processes
- Spraying processes
- Physical vapor deposition processes

For organic electronics, mainly processes of one of the last three groups are used. While samples prepared with physical vapor deposition techniques often show the best film quality and crystallinity, wetting and spraying processes are often used, if a cheap and easy to apply technique is desired. All wetting processes have in common that the material is applied in liquid form first before it becomes solid. The focus here is on this kind of processes, since the samples presented in this thesis are all produced by a wetting process.

The easiest way to produce thin films and one that can be done without any special equipment is to dip a sample into a liquid. By changing the dipping conditions (like withdrawal velocity or temperature) the film formation can be controlled. A modified variant is also used to make self-assembled monolayers known as Langmuir-Blodgett films [3, 4].

An equally simple method is drop casting. There, a drop of material in solution is put on the sample. The solution evaporates and a thin film remains. However it is hard to get a good film quality and repeatability. An alteration of this method is to spin the sample after the drop is placed on it. By varying the parameters (e.g. the concentration of the solution or the rotation speed) the film thickness can be controlled very accurately. Uniform films with a good reproducibility can be achieved. This process, known as spin coating, is used for the preparation of the samples in this thesis and is discussed in more detail in section 3.7.

1.1.2. Modes of thin-film growth

Independent of the deposition process, the nucleation and growth of the thin film always coincides with a phase transition. For the spin coating process this is a phase transition from the liquid phase (the solution) to a solid phase (the thin film). For film growth to take place, stable nuclei have to form first, followed by a growth of these nuclei. In general the nuclei are not in the most stable conformation but rather are formed in the least stable one first. This phenomenon is called the Ostwald rule [5]. Depending on the interactions between the substrate and the growing film, three different growth modes are known after the initial nucleation (see figure 1.1).

The island growth mode (or Volmer-Weber mode) is characterized by a nucleation and following growth of 3D islands directly on the surface. The atoms are more strongly bound to each other than to the surface. This can be expressed in terms of the surface energy. For island growth mode, the surface energy of the deposit (γ_A) and the energy of the interface (γ^*) are bigger than the surface energy of the substrate (γ_B), $\gamma_A + \gamma^* > \gamma_B$. The layer growth mode (or Frank-van der Merwe mode) occurs, if the interaction between the adsorbed atoms and the substrate is bigger than the one between the adsorbed atoms. For the surface energies, $\gamma_A + \gamma^* < \gamma_B$ holds. The binding energy of the next layers decreases continuously and converges to the binding energy of the bulk crystal. An intermediate growth mode is the layer plus island mode (or Stranski-Krastanov mode). There, after one (sometimes also after more than one) layer is closed, the atoms are more strongly bound to each other than to the underlying layer, because of the decreasing influence of the surface. Then, the

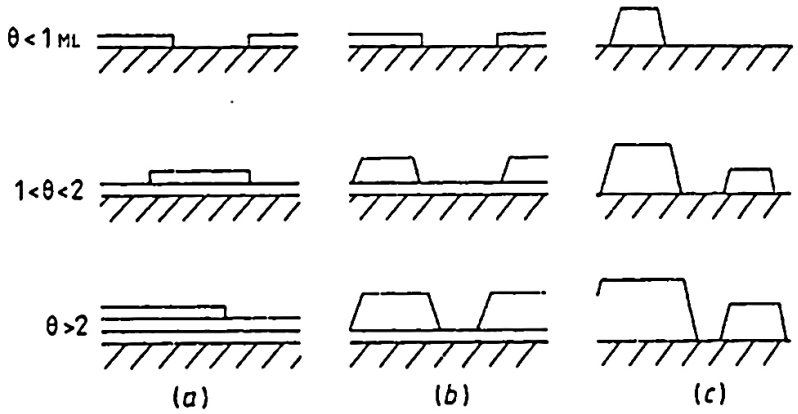

Figure 1.1.: The three different growth modes. (a) layer growth (or Frank-van der Merwe mode), (b) layer plus island growth (or Stranski-Krastanov mode), (c) island growth (or Volmer-Weber mode) for increasing coverage Θ in monolayers. (reprinted from [6])

film continues to grow in island mode. The interface energy depends on the distance to the surface and therefore the energy balance is varied [6].

This model is based on equilibrium phenomena. However, film growth in general is a non-equilibrium phenomenon. Therefore the actual growth is often kinetically determined. Furthermore the model was developed for atomic, ball-shaped, building blocks. Organic molecules can show a different behavior due to their spatial expansion and the deviation from a sphere [7].

Especially for elongated, rod-like molecules there are at least two general possible orientations of the molecule on the surface. The molecule can lie down with its long-axis parallel to the surface or it can stand upright with its long-axis parallel to the surface normal (see figure 1.2). Both configurations have their advantages and depending on the application of the film (for example as organic light emitting device or organic thin film transistor) one or the other might be the preferred one [8].

1.2. Liquid crystals

At the end of the 19th century a new state of matter in between liquid and crystalline was found. Since molecules in this state may be able to flow like a liquid but still have, up to a certain degree, long range positional and orientational order like a crystal, it was called liquid crystalline state (see figure 1.3). Until the 60s of the 20th century, liquid crystals (LCs) were only of academic interest for a small number of scientists, because no market applications were known. This changed completely with the development of the first liquid crystal displays (LCDs) [9]. Until now the main technological application of LCs is all kinds of displays.

Molecules may show LC phases, if the crystallization process is hindered by an

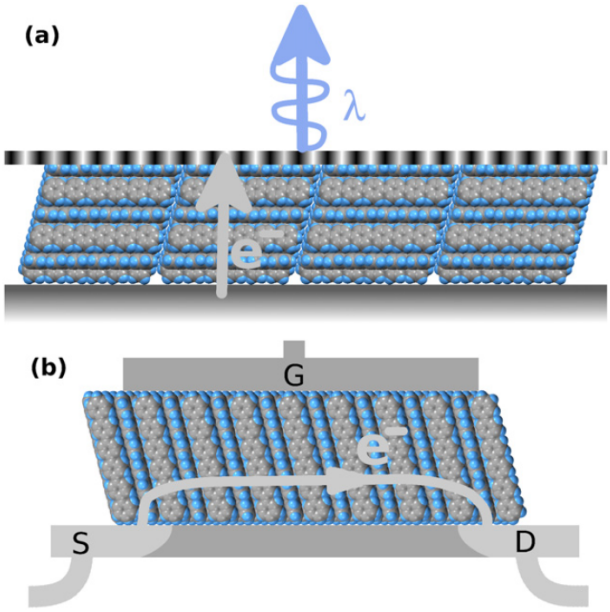

Figure 1.2.: Schematic representation of the two possible orientations of rod-like molecules on a substrate. (a) flat lying orientation, beneficial for e.g. organic light emitting devices. (b) upright standing orientation in an organic thin film transistor. (reprinted from [8])

Figure 1.3.: Definition of a liquid crystal based on the orientational and positional order of the molecules. Liquid crystals are in between a solid crystal and a liquid. They have orientational order but no 3-dimensional positional order. (reprinted from [10])

increasing molecular anisotropy of the molecules. This can be disc-like molecules, like in the dicotic phases explained later, or rod-like molecules with a rigid backbone and a flexible sidechain. Adding alkyl groups to small organic molecules is one way to get liquid crystalline materials.

In the design of molecules for organic electronics, solubility plays an important role. A way to increase the solubility is again to add alkyl groups to the molecules. Consequentially many organic semiconductors show liquid crystal phases. In the last years, this fact was more and more used to improve the properties of organic thin films by exploiting the self-healing and ordering ability of molecules in the liquid crystalline phases [11–13].

Throughout the next section I will show that there are a number of different liquid crystalline phases and I will try to give an introduction into the classification and the nomenclature based on the *International Union of Pure and Applied Chemistry* (IUPAC) recommendations 2001 [14]. DOTT, the molecule investigated in this thesis, shows three different phases (also called mesophases) between the crystal and the isotropic phase. It is important to keep this fact in mind, if the temperature is changed between or during the experiments. A phase transition can have a tremendous effect on some of the properties investigated (e.g. morphology or crystal structure).

1.2.1. Types of liquid crystals

There are two different classes of liquid crystals:

1. **Thermotropic liquid crystals** change from the solid state to the liquid crystal state by heating or from the isotropic state by cooling. Therefore the temperature is the critical variable.

2. **Lyotropic liquid crystals** do not show liquid crystalline behavior when they are pure. Only when dissolved, amphiphilic molecules become a LC. In addition to the temperature, the crystallinity also dependents on the concentration of the solution.

Despite their importance for example in biological systems, lyotropic LCs will not be considered in more detail here.

The essential property of thermotropic LCs is the anisotropy of the molecules. There are two main types of molecules that exhibit LC phases. One is the so called calamitic type, which has a rod-like shape. DOTT falls into this category and therefore the following classification is based on calamitic molecules. The other type is the discotic one. Discotic molecules have a disk-like shape (see figure 1.4) and often exhibit a columnar phase with 2D positional order.

A classification of the different mesophases of a thermotropic LC can be based on the degree of order. All liquid crystals have orientational order (This is also used to define a liquid crystal in general as in figure 1.3). However the positional order can vary from no positional order to 2D positional order.

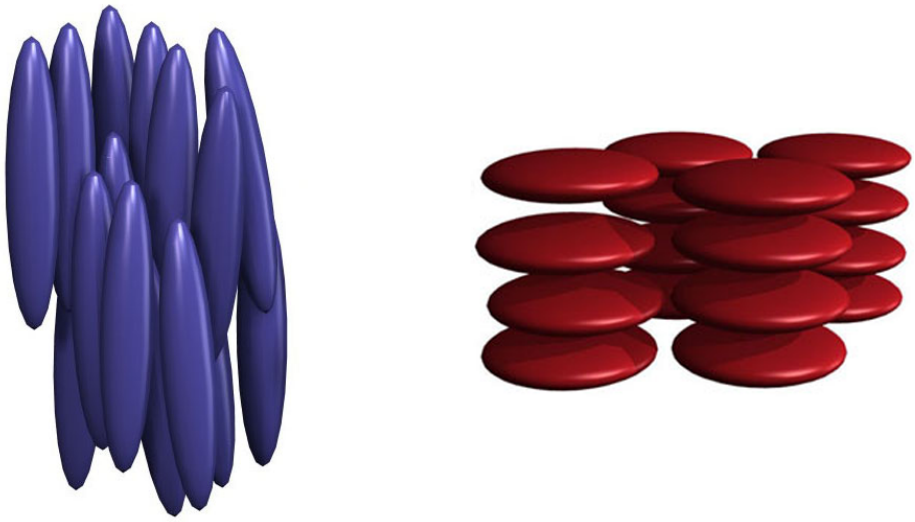

(a) **(b)**

Figure 1.4.: The two main types of molecules for thermotropic liquid crystals. (a) rod-like molecules form calamitic LCs. (b) disk-like molecules form discotic LCs. (reprinted from [15] and modified)

- The most disordered phase is called **nematic** phase. This phase has no positional order. Only the orientation of the molecules is of long range order. The molecules roughly align in the same direction. The average direction is expressed by a vector $\hat{\mathbf{n}}$, called the director. The director can be manipulated by either the surrounding surfaces (for example corrugations on the surface) or by external fields. This effect is used in twisted nematic (TN) displays, which are the most common LCDs.

- By adding a 1D positional order, one comes to the **smectic** mesophases. The orientational order from the nematic phase remains but the molecules become ordered in one dimension. A layered structure evolves with a certain layer distance. Within one layer the molecules behave like a 2D liquid without any long range orientational order. A number of different smectic phases was found and named smectic A (SmA), smectic B (SmB) etc. in the order of their discovery. Some phases originally called smectic proved to be soft crystal phases in the end. Hence the naming is not very systematic. However two sub-groups can be identified.

  1. **SmA** and **SmC** are phases where the centers of mass of the molecules in one of the layers behave like true 2D liquids. The director of the molecules in the smectic A phase is perpendicular to the layers. In the smectic C phase the director is tilted away from the layer normal.
  2. The **SmB**, **SmI** and **SmF** phases already show some in-plane ordering with long range bond orientational order. However translational order is

lost within a few nanometers. A 'hexatic' order is developed with molecules, where the director is perpenticular to the layers (SmB) or tilted (SmI, tilted towards a vertex; SmF, tilted towards an edge of the hexagonal net) [16].

- **Soft crystal** phases are the closest ones to the crystalline state. They have long range positional order in all three dimensions. The difference is that the layers are only weakly bound to each other. Soft crystal B and E again have molecules perpendicular to the layers (compare with SmB) and soft crystal G, H, J and K are tilted (like SmI and SmF). The soft crystal phases E, J and K organize in a herringbone pattern.

The different liquid crystal phases are summarized in table 1.1. They are ordered by the degree of their positional order. The isotropic and crystal states are also shown for orientation. By heating a crystal one would go from the top of the table to the bottom. By cooling from the isotropic phase from bottom to top. Not all intermediate phases have to be present and most materials will only exhibit some of them.

Table 1.1.: Summary of the different liquid crystal phases in comparison with the crystal and the isotropic phase [10].

Phase	Positional order	Orientational order
Crystal	3D	Yes
Columnar LC	2D	Yes
Smectic LC	1D	Yes
Nematic LC	No	Yes
Isotropic	No	No

1.3. Organic semiconductors

Since the demonstration of the first metal-oxide-semiconductor field-effect transistor (MOSFET) based on silicon in 1960 [17], inorganic semiconductors were used as active semiconductor layer for the production of commercial electronic devices. The rapid development and the superior properties of the silicon - silicon-oxide interface relegated organic semiconductors to a mainly scientific matter.

The breakthrough for organic electronics came with the development of conducting conjugated polymers in the 1970s. The demonstration of an organic field effect transistor (OFET) based on the polymer polythiophene by Koezuka *et al.* [18] paved the way for a wide range of applications. The synthesis of high-efficiency electroluminescent materials made the construction of organic light emitting devices (OLEDs) a seminal concept [19, 20]. The first commercial full-color polymer OLED display based on electroluminescent materials was presented by Toshiba in 2001 [21]. Since then OLED displays found their way into modern mobile phones. Bigger displays for

TVs and Laptops are about to become available at competitive prices. Next to the commercial success of organic semiconductors in OLED displays, the development of OFETs for organic electronics and organic photovoltaic cells (OPVCs) goes on.

Despite the well known advantages of organic semiconductor devices (like solution-based processing, compatibility with flexible substrates, tuning of electronic and structural properties by tailored materials, cost-efficient large area production etc. see for example [22]) a number of challenges still keep scientists around the word busy:

- Organic semiconductors are very sensitive and react with oxygen and water. In ambient conditions most devices are destroyed in short times. Therefore devices have to be encapsulated very thoroughly.

- Even when encapsulated, the materials degenerate and therefore the efficiency decreases with time. This is a problem especially for devices with a long average life like OPVCs.

- The performance of most applications is essentially determined by the transported charge per unit time and therefore the current in a material. On a macroscopic scale, the current can by expressed by

$$j = env = en\mu E, \tag{1.1}$$

where e is the electric charge of an electron, n is the charge carrier density and v the carrier drift velocity which again can be written as the mobility μ times the electric field E.

Theoretically the density can be calculated by

$$n_i = N_0 \cdot \mathrm{e}^{-\frac{E_g}{2kT}}. \tag{1.2}$$

Following Brütting [7], calculating the density of a typical organic semiconductor ($E_g = 2,5\,\mathrm{eV}$, $N_0 = 10^{21}\,\mathrm{cm}^{-3}$) gives $n_i = 1\,\mathrm{cm}^{-3}$ which is orders of magnitude smaller than the charge carrier density of silicon ($E_g = 1,12\,\mathrm{eV}$ and $N_0 = 10^{19}\,\mathrm{cm}^{-3}$ give $n_i = 10^{10}\,\mathrm{cm}^{-3}$). This is of course an estimation and impurities in the organic semiconductor, which lead to higher charge carrier densities, are neglected.

There are a number of ways to increase the charge carrier density. The most important ones in OFETs are doping and carrier injection [7].

The second quantity, the mobility μ, has an upper limit that is an intrinsic property of the material. In practice however, μ is mainly limited by the preparation of the active layer and the contacts. As an example, the mobility of differently prepared pentacene films is shown in figure 1.5. The mobility of the different samples is alternated by some orders of magnitude and ranges from values that are considered isolating ($10^{-8}\,\mathrm{cm}^2/\mathrm{Vs}$) for the unordered film up to the mobility of hydrogenated amorphous silicon ($10^{0}\,\mathrm{cm}^2/\mathrm{Vs}$), which is often used as a

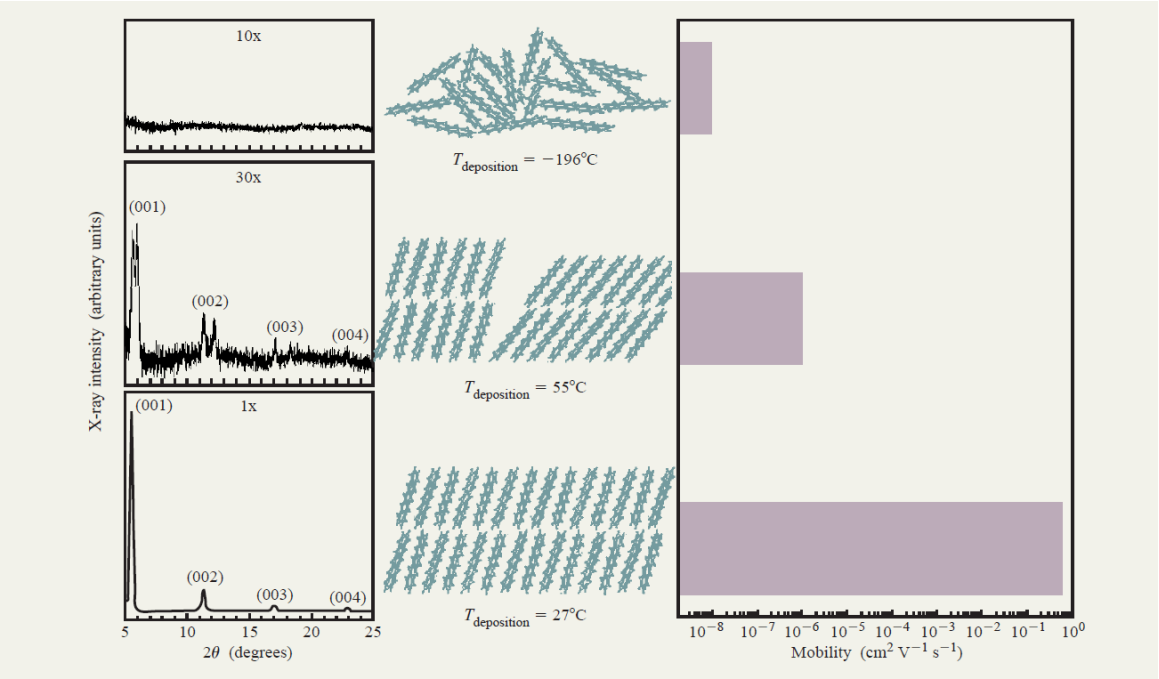

Figure 1.5.: Comparison of pentacene thin films prepared at different sample temperatures $T_{deposition}$. The mobility is dependend on the structural order of the films, which can be seen from the X-ray diffraction patterns. (reprinted from [23])

reference mobility for OFETs. This explains how important it is to understand the growth of organic thin films. The maximum mobility of a material can only be approached in OFETs, if the best orientational order is known and films with this order can be produced. Therefore a typical approach to improve the mobility looks like this [23]:

1. Synthesis or first time use of a new organic semiconductor.
2. The best structure and morphology, with the best performance of the organic thin film is searched. This can be done by altering the deposition parameters (like the temperature, growth rate, deposition process, concentration of the solution etc.) or by a pre-treatment of the substrate until no improvement seems possible.
3. Iteration of the two steps.

1.3.1. Small molecules

Polymers have been the first known organic semiconductors and they have been used in the majority of organic semiconducting devices because they can be processed from solution easily and they have good film-forming properties. However the above mentioned situation, that the device performance strongly depends on the structure and morphology of the films, revealed some disadvantages of polymers.

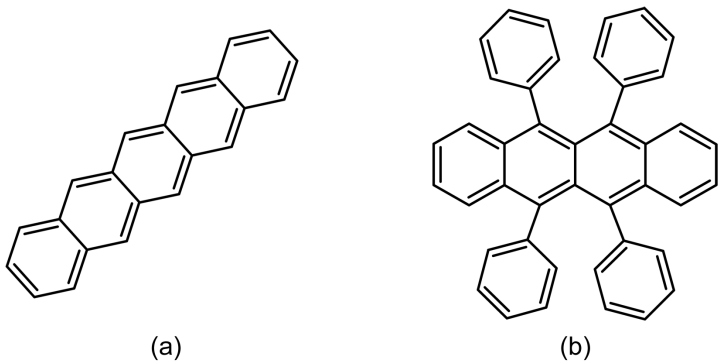

Figure 1.6.: Chemical structure of (a) pentacene and (b) 5,6,11,12-tetra-phenyl-naphthacene, known as rubrene.

- The molecular weight of polymers is a statistical average and there are, to a certain extend, always shorter and longer chains in the material.
- Due to their poor crystallinity, it is harder to control the structure of polymer thin films.
- Polymers are hard to purify.

This made the second class of organic semiconductors, small molecules, more and more interesting for academic and industrial researchers. Small molecules have a well defined molecular structure. Most of them will crystallize easily and it is also easier to purify them.

In the last years, a number of small molecules have shown higher mobilities than a-Si:H and left polymers behind by a factor of ten (see figure 1.7). With elaborate methods it is even possible to produce OFETs consisting of only one crystal [24]. The OFET mobility of rubrene in this single crystal devices is the highest known so far for organic semiconductors. Next to rubrene and pentacene [25] (see figure 1.6 for the chemical structures), the probably most studied organic semiconductor, also oligothiophenes are known to exhibit high mobilities [26].

A major advantage of molecular electronics is the possibility to produce devices with solution-based methods. By easy and cheap methods like spin coating, spin casting or inkjet printing, the manufacturing costs for large area electronics can be decreased by avoiding lithographic techniques.

An obvious requirement for solution based methods is the solubility of the materials used. A way to improve the solubility is to attach terminal alkyl chains to the materials as already mentioned in section 1.2. This was first introduced for the polymer poly(3-hexylthiophene) (P3HT) where a hexyl chain is added to the thiophene ring (see figure 1.8 for the chemical structure).

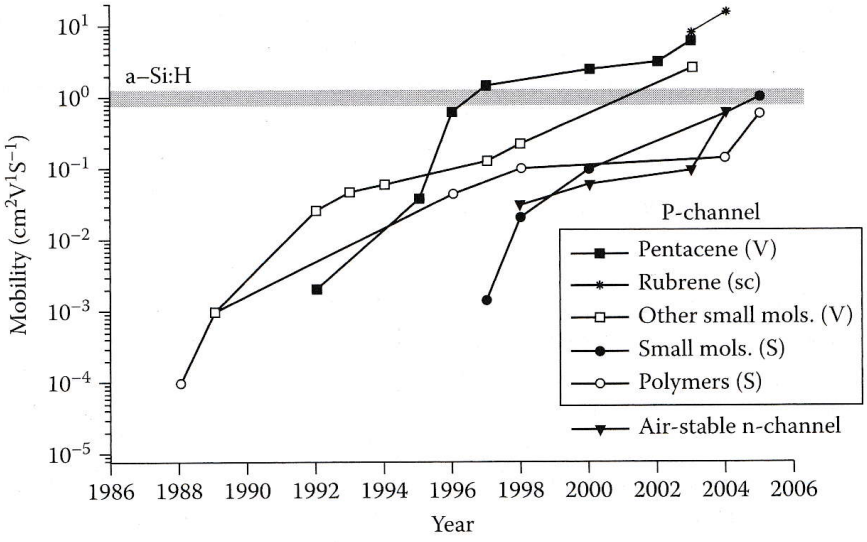

Figure 1.7.: Increase of OFET mobility over time in comparison to the mobility of hydrogenated amorphous silicon (a-Si:H). (V): vacuum deposition, (sc): single crystal, (S): solution deposition. (reprinted from [22])

The same principle was adopted for small molecules. Oligothiophenes of different length, which are nearly insoluble when unsubstituted, with substituted linear alkyl groups at the α- and α'-position not only possess a better solubility but also have better film forming properties. Thin films with higher molecular order can be produced, which in turn leads to higher mobilities [26].

Already in 1996, Dimitrakopoulos *et al.* mentioned a peculiarity of pentacene thin films [27]. In the vicinity of a surface, these films show a number of different polymorphs. Depending on the preparation conditions, surface induced phases can be produced that have different crystallographic unit cells than the bulk phase. This phenomenon was then also observed for other small molecules. Wedl *et al.* [28] report three different polymorphs for dihexyl-terthiophene (DHTT). They can correlate the different phases with the preparation parameters and conclude that the thin film phase is a metastable phase, formed only next to a surface and for growth conditions far from equilibrium (fast crystallisation speed). The material investigated in this thesis, dioctyl-terthiophene, is a very similar one. The only difference beeing the length of the alkyl chains.

In the next section I will introduce the material dioctyl-terthiophene and review some of the results for DOTT thin films.

1.4. Diotyl-Terthiophene

Oligothiophenes, with their conjugated backbone, are model materials for the active layer of organic semiconducting devices. The material α-α'-dioctyl-terthiophene

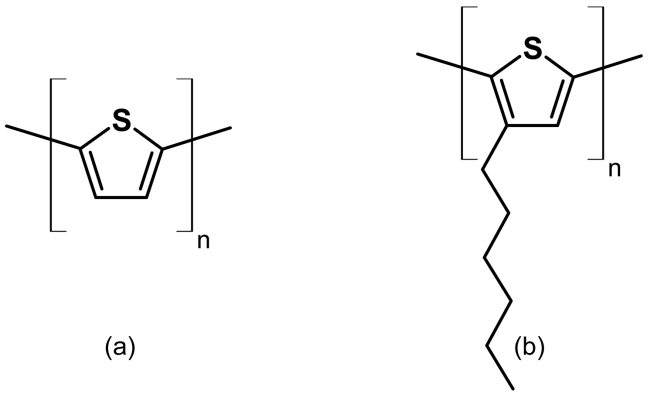

Figure 1.8.: (a) Polythiophene and (b) poly(3-hexylthiophene) also known as P3HT, where a hexyl chain is added to the thiophene ring for solubility.

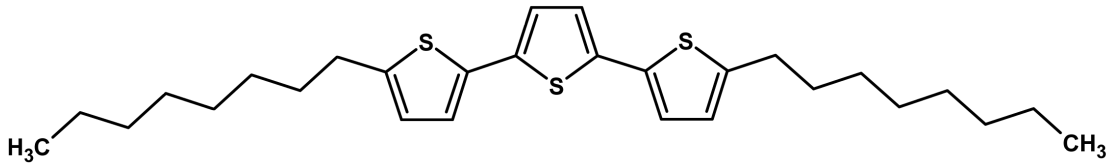

Figure 1.9.: chemical structure of α-α'-dioctyl-terthiophene (DOTT)

(DOTT) was first synthesized by the group of Hanna in 2000 [29]. The chemical structure is presented in figure 1.9. The three thiophene rings in the middle are linked with single carbon-carbon bonds. This makes the molecule flexible and rotations of the thiophene rings are possible. Two octyl groups are substituted at the α and α' position, which is at both ends of the terthiophene-backbone. The alkyl chains increase the solubility and are another flexible part of the molecule. Different orientations of two chains are possible. The appearance of liquid crystalline phases can already be expected from the structure of the molecule.

1.4.1. Liquid crystalline phases

The material used in this thesis was synthesized by the group of Yves Geerts with a high-yield one-step procedure fully explained in [30]. Indeed it shows liquid crystalline behaviour. The thermotropic phases were characterized by differential scanning calorimetry (DSC). DSC is based on the detection of the amount of heat that is required to change the temperature of a sample compared to a reference. At a first-order phase transition, a latent heat, the transition enthalpy, can be measured. A DSC curve is measured by increasing the temperature and simultaneously measuring the amount of heat that is needed for this temperature change. The same can be done in the other direction by cooling the sample. The curve will then be shifted depending on the heating/cooling rate applied.

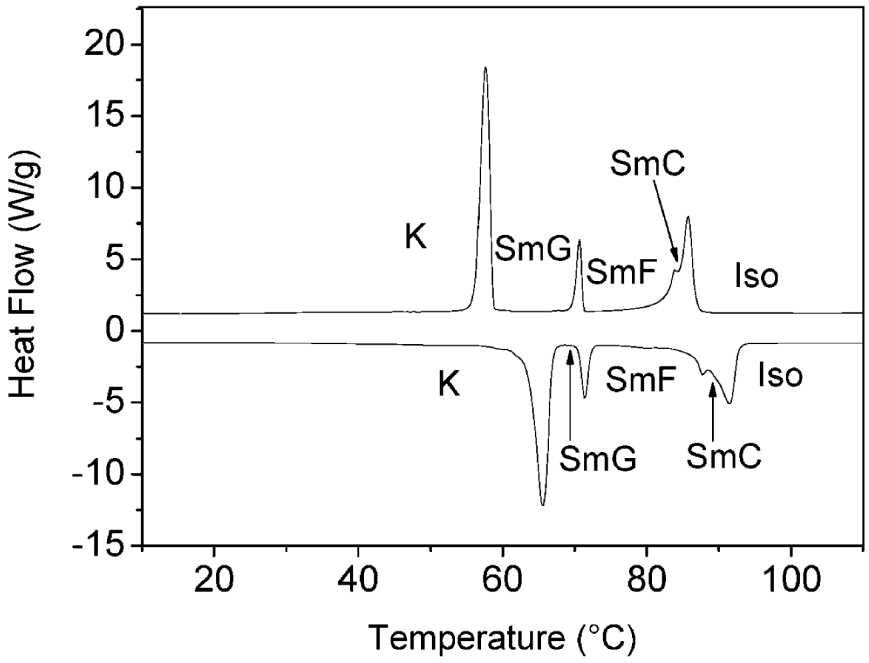

Figure 1.10.: DSC curve of DOTT. A soft crystal G and two liquid crystal phases lie in between the crystalline phase (K) and the isotropic phase (Iso). Exact values for the heating curve are in table 1.2. (reprinted from [31])

The DSC curve of DOTT in figure 1.10 was recorded with a heating rate of 5 °C/min. It shows four phase transitions which are identified as a soft crystal G phase and two liquid crystal phases between the crystalline and the isotropic state. The temperatures and the transition enthalpies can be found in table 1.2. Between the crystalline and the crystal G phase, a large transition enthalpy of 24,4 kJ/mol indicates a substantial change in the molecular order [31].

Table 1.2.: Temperature (T) and transition enthalpy (H) of the four phase transitions between the crystalline (K) and the isotropic state (Iso) of DOTT for a heating rate of 5 °C/min.

	K	-	G	-	SmF	-	SmC	-	Iso
T / °C		64		71		85		90	
H / kJ/mol		-24,4		-3,3		-1,6		-7,3	

1.4.2. Molecular packing

In section 1.1, the orientation of the molecules on the substrate was identified as an important parameter. From the simulation of the molecular packing (which is the orientation of the molecules in the unit cell) and the comparison of simulated and

measured X-ray powder diffraction curves, information about the molecular alignment of DOTT can be obtained. Based on such calculations, Lemaur *et al.* [31] assume a layered structure with a layer thickness of 29,1 Å for the crystal G and 32,4 Å for the crystalline phase. In the crystalline phase DOTT powder adopts a herringbone packing with upright standing molecules, while in the crystal G phase the molecules are tilted. However a lot of reflections in the measured diffraction curves are not explained by the found unit cell. Lemaur *et al.* explain this by the coexistence of different polymorphs. Also the mobility they found for DOTT FETs is very low with μ beeing of the order of $10^{-6}\,\mathrm{cm}^2/\mathrm{Vs}$. Again they conclude that mainly the presence of grain boundaries and polymorphs in the crystal phase is the limiting factor for OFET performance.

Werzer *et al.* [32] investigated DOTT thin films on a SiO_2 surface. By a combined specular X-ray diffraction and grazing incidence diffraction study they find that in the vicinity of a surface, DOTT forms two polymorphic phases already at room temperature. Since one phase seems to be more dominant next to the surface, it is called s-phase, which is short for surface-induced phase. The phase further away from the surface is called b-phase, which stands for bulk phase. Additional phases were found at elevated temperatures (see figure 1.11). While the b- and s-phase are orthorhombic, the other phases at higher temperature all have a tilted unit cell (see table 1.3 for more details).

Table 1.3.: Unit Cells of the b-, s- and crystal G phase of DOTT thin films as reported by Oliver Werzer [32].

temp / K	phase	**a** / nm	**b** / nm	**c** / nm	β / °
298	b-phase	0,773	0,555	6,42	90
298	s-phase	0,763	0,548	6,62	90
340	crystal G	0,912	0,556	6,12	108

They also report of an interface monolayer buried under the film. The formation seems to be independent of the layer thickness. Since only one rod in the grazing incidence diffraction measurements (see rod 11* in figure 1.11) could be assigned to the interface monolayer, the molecular order and unit cell parameters of this layer could not be found.

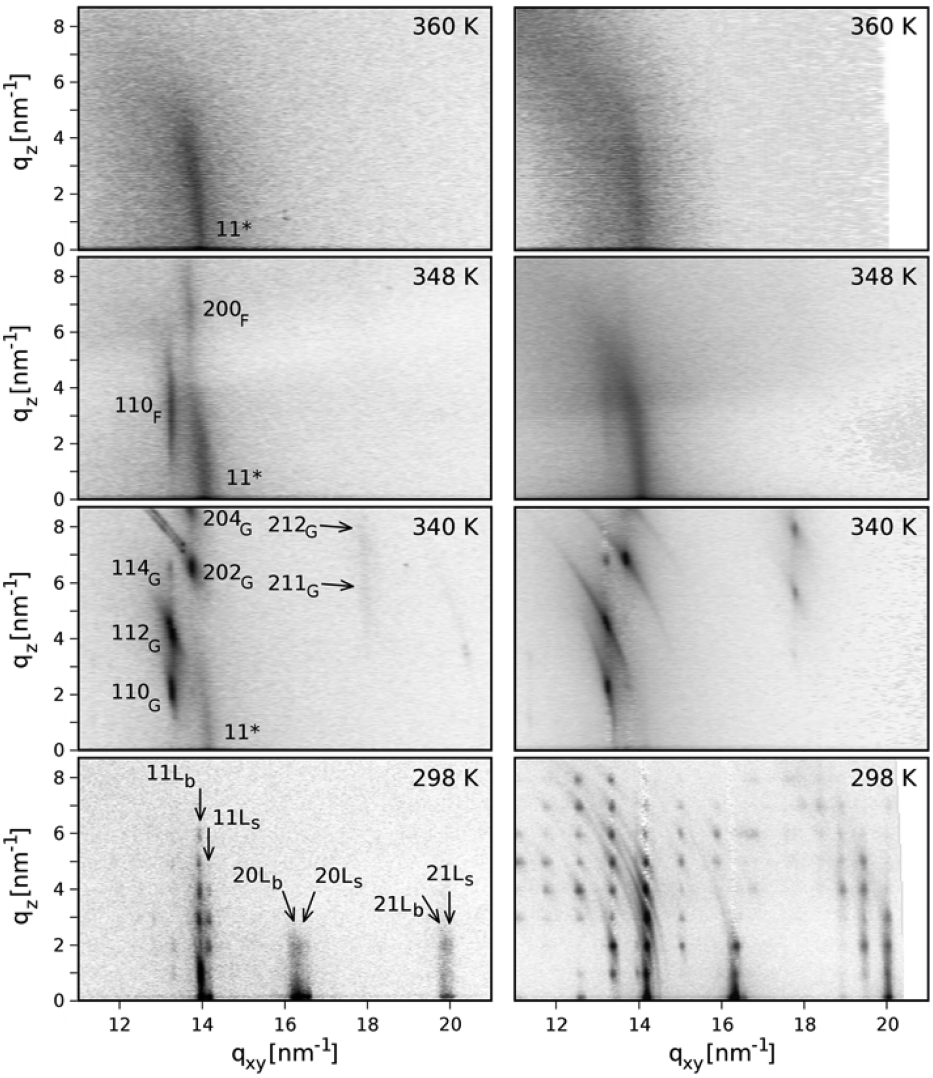

Figure 1.11.: Grazing incidence measurements of 20 nm (left column) and 100 nm (right column) thick DOTT films. Measurements were done at room temperature (bottom row) and up to 360 K (top row). The spots are indexed with their HKL values and the subscript indicates the corresponding phase. The 11* rod is assigned to the interface monolayer. (reprinted from [32])

2. Experimental methods

In this chapter the different methods used to study the DOTT ultra-thin films are introduced. First the focus will be on X-ray based techniques. Therefore the first part contains a basic description of the interaction of X-rays with matter. Some fundamental relations and laws are derived and based on this theory the two X-ray techniques used in this work (X-ray reflectivity and grazing incidence X-ray diffraction) are presented. Then a short introduction into atomic force microscopy and contact angle measurements will be given.

2.1. X-ray scattering

In the last years, X-ray based techniques have proven to be perfectly suitable for the investigation of thin films. One of the advantages, especially in comparison to conventional imaging techniques, is the well known property of X-rays to pass through light materials with only little absorption. Therefore it is possible to investigate not only the uppermost but also the buried layers and interfaces. While passing through a material, the X-rays will interact with it in different ways. In the next section the interactions that occur in the energy range of interest are summarized.

The next sections are based on the textbooks of Jens Als-Nielsen [33], Mario Birkholz [34] and Lothar Spieß [35].

2.1.1. Interaction with matter

X-rays are electromagnetic waves with a wavelength of around $10^{-8}\,\mathrm{m}$ to $10^{-12}\,\mathrm{m}$. A convenient and often adequate description of the propagation of the electric field of X-rays is in the form of a plane wave

$$\mathbf{E}(\mathbf{r},t) = E_0 \cdot \mathrm{e}^{i(\mathbf{k}\cdot\mathbf{r}-\omega t)} \tag{2.1}$$

where $\mathbf{k}$ is the wavevector in the direction of the propagating field.

For the energy range of interest for the X-ray scattering techniques described here, the X-rays interact mainly with the electrons and not the atoms. Three different types of interaction have to be considered.

1. **The photoelectric effect:** An electron is knocked out from the bound states in the atom and characteristic radiation is emitted. This process is *incoherent* and *inelastic*.

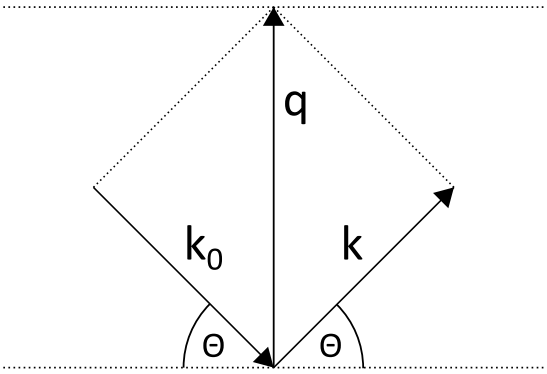

Figure 2.1.: Representation of the scattering vector q as the difference between k_0 and k, the incident and the final wave vectors respectively.

2. **Compton scattering:** The X-ray photon interacts with an electron of which the binding energy is negligible and the electron therefore quasi free. The photon gets scattered and transfers some of its energy to the electron. Compton scattering is *incoherent* and *inelastic*.

3. **Thomson scattering:** The electrons are forced to oscillate like a Hertz dipole. Radiation of the same wavelength as the incoming photon is emitted. This interaction is used in X-ray diffraction. In contrast to the other two processes, Thomson scattering is *coherent* and *elastic*.

For Thomson scattering, the length of the initial wave vector $|\mathbf{k}_0|$ (which is the same as the length of the final wave vector $|\mathbf{k}|$ because it is an elastic process) is defined as

$$|\mathbf{k_0}| = \frac{2\pi}{\lambda}. \tag{2.2}$$

While no energy is transferred in a Thomson scattering event, momentum can of course be transferred. In this case the initial and the final wave vector form a parallelogram as sketched in figure 2.1. From there the following relationship is obvious:

$$\mathbf{q} = \mathbf{k} - \mathbf{k_0}, \tag{2.3}$$

where $\mathbf{q}$ is called the scattering vector. To describe elastic scattering processes, this quantity has a huge advantage and is therefore mostly used in the field of X-ray diffraction: While the scattering angle Θ depends on the wavelength of the X-rays, $\mathbf{q}$ is independend of it and can therefore be used to compare results from experiments with different wavelength directly. From figure 2.1 a relation for $|\mathbf{q}|$ can be derived:

$$|\mathbf{q}| = \frac{4\pi}{\lambda} \sin\Theta, \tag{2.4}$$

where λ is the wavelength of the incoming photon and Θ is the scattering angle.

2.1.2. Crystallography and the reciprocal space

From the diffraction pattern that is obtained from the interaction of X-rays with the periodic crystal structure, one can get information about the atomic or molecular organization in the material. However, the diffraction patterns are not as easy to interpret as for example microscopy images. To understand them, some knowledge about the crystal structure of the material is needed. In this section I will briefly revise the basics of crystallography and introduce the important concept of the reciprocal lattice.

The direct lattice

It would be possible to describe a crystal by writing down all the positions of all the atoms. However, this approach gets infeasible if one tries to do this for a macroscopic crystal with around 10^{23} atoms in only one cubic centimeter. A better way is to make use of the periodic structure of the crystal. One has to find a motif that is repeated throughout the whole crystal. The motif, that consists of some atoms or molecules, is called the *basis*. The periodic structure in which the basis is repeated is then called the *crystal lattice*. The crystal lattice is a point lattice, where each point is the origin for one basis.

The crystal lattice is explained with three lattice vectors that form a parallelepiped called the unit cell. By repeating the unit cell in all directions, all lattice points can be described. This is illustrated in

$$\mathbf{R}_n = n_1\mathbf{a} + n_2\mathbf{b} + n_3\mathbf{c} \tag{2.5}$$

where $\mathbf{R_n}$ are all the lattice points, n_i are integers and $\mathbf{a}$, $\mathbf{b}$, $\mathbf{c}$ are the three lattice vectors [33].

The basis describes the position of the atoms in the unit cell. By using the lattice vectors, the positions can be described by:

$$\mathbf{r}_n = x_n\mathbf{a} + y_n\mathbf{b} + z_n\mathbf{c} \tag{2.6}$$

where $\mathbf{r}_n$ are the positions of the atoms given in fractions $0 \leq x_n, y_n, z_n \leq 1$ of the lattice vectors.

The interplanar spacing

The orientation of a plane in the lattice is described by Miller indices $(h\,k\,l)$. The Miller indices are proportional to the inverse distance of the intersection of the plane with the crystal coordinate system, spanned by the three lattice vectors. The indices $(h\,k\,l)$ describe the orientation of a single plane but also of a set of parallel planes. The distance between two neighboring planes described by the same Miller indices (the *interplanar spacing* d_{hkl}) is an important parameter in the analysis of diffraction patterns. For an orthorhombic system, like DOTT below 64 °C, the interplanar spacing can be calculated by

$$d_{hkl} = \frac{1}{\sqrt{\left(\frac{h}{a}\right)^2 + \left(\frac{k}{b}\right)^2 + \left(\frac{l}{c}\right)^2}} \tag{2.7}$$

The reciprocal lattice

While the lattice described above is called the direct or real lattice, the same lattice can also be described in reciprocal space and is then called reciprocal lattice. This representation is directly related to the real one and the reciprocal lattice vectors ($\mathbf{a}^*$, $\mathbf{b}^*$ and $\mathbf{c}^*$) can be derived from the real ones by

$$\mathbf{a}^* = 2\pi\frac{\mathbf{b}\times\mathbf{c}}{\mathbf{a}\cdot(\mathbf{b}\times\mathbf{c})}; \quad \mathbf{b}^* = 2\pi\frac{\mathbf{c}\times\mathbf{a}}{\mathbf{b}\cdot(\mathbf{c}\times\mathbf{a})}; \quad \mathbf{c}^* = 2\pi\frac{\mathbf{a}\times\mathbf{b}}{\mathbf{c}\cdot(\mathbf{a}\times\mathbf{b})}. \tag{2.8}$$

The points of the reciprocal lattice can again be expressed by a linear combination of the three lattice vectors:

$$\mathbf{G}_{hkl} = h\mathbf{a}^* + k\mathbf{b}^* + l\mathbf{c}^* \tag{2.9}$$

It is worth mentioning that the integers h, k and l are connected to the Miller indices $(h\,k\,l)$. The vector $\mathbf{G}_{hkl}$ is perpendicular to the plane with the Miller indices $(h\,k\,l)$. Moreover, the length of $\mathbf{G}_{hkl}$ is the inverse value of the interplanar spacing d_{hkl}:

$$\mathbf{G}_{hkl} = \frac{2\pi}{d_{hkl}} \tag{2.10}$$

2.1.3. Kinematic scattering theory

To understand in which direction the incoming X-rays get scattered from a crystal and therefore where high scattered intensity is detected as diffraction or *Bragg peaks*, the Laue condition and Bragg's law are derived in the following section. For this purpose the kinematic scattering theory is, despite its simplifications, sufficient. Again the regular arrangement of the atoms in a crystal is used to find a simple and comprehensible result.

First the amplitude of the scattered wave from only one atom is described by the so called *atomic scattering factor* $f(\mathbf{q})$:

$$f(\mathbf{q}) = \int \rho(\mathbf{r})\mathrm{e}^{i\mathbf{qr}}\,\mathrm{d}\mathbf{r} \tag{2.11}$$

where $\rho(\mathbf{r})$ is the charge density of the atom, which is the square of the electronic wave function.

In the case of a simple cubic crystal there is only one atom in the unit cell and the atomic scattering factor describes the whole unit cell. However for unit cells with more than one atom, the contribution of all of them has to be considered by summing over all atomic positions. This leads to the *structure factor* $F(\mathbf{q})$:

$$F(\mathbf{q}) = \sum_{n=1}^{N} f_n \, \mathrm{e}^{i\mathbf{q}\mathbf{r_n}} \tag{2.12}$$

where f_n and $\mathbf{r_n}$ are the atomic scattering factors and the positions of the N atoms (in fractional coordinates) in the unit cell respectively.

As a last step, the unit cell has to be copied to every lattice site. Again this is done by summing over all possible lattice sites. As a final result for the amplitude of the scattered wave we get:

$$E = E_0 \cdot F \cdot \sum_{n_1=1}^{N_1} \mathrm{e}^{i\mathbf{q}\,n_1\mathbf{a}} \sum_{n_2=1}^{N_2} \mathrm{e}^{i\mathbf{q}\,n_2\mathbf{b}} \sum_{n_3=1}^{N_3} \mathrm{e}^{i\mathbf{q}\,n_3\mathbf{c}} \tag{2.13}$$

where N_i are the number of lattice sites in the three directions $\mathbf{a}$, $\mathbf{b}$ and $\mathbf{c}$. The three sums can be converted by considering the formula for geometric rows and by squaring the result one gets the so called Laue or interference function

$$\Im(\mathbf{q}) = \frac{\sin^2\left(\frac{N_1}{2}\mathbf{qa}\right)\sin^2\left(\frac{N_2}{2}\mathbf{qb}\right)\sin^2\left(\frac{N_3}{2}\mathbf{qc}\right)}{\sin^2\left(\frac{1}{2}\mathbf{qa}\right)\sin^2\left(\frac{1}{2}\mathbf{qb}\right)\sin^2\left(\frac{1}{2}\mathbf{qc}\right)} \tag{2.14}$$

The intensity of the scattered wave I is then given by

$$I = EE^* = I_0 \cdot |F|^2 \cdot \Im \tag{2.15}$$

The evaluation of equation (2.14) shows, that the highest intensity is found if the three Laue equations are fullfilled:

$$\mathbf{qa} = 2\pi h; \quad \mathbf{qb} = 2\pi k; \quad \mathbf{qc} = 2\pi l \tag{2.16}$$

A combination of equations (2.8), (2.9) and (2.16) finally gives the famous Laue condition

$$\boxed{\mathbf{q} = \mathbf{G}} \tag{2.17}$$

which shows that only if the scattering vector $\mathbf{q}$ coincides with a reciprocal lattice vector $\mathbf{G}$, non-vanishing intensity will be detected.

Rewriting equation (2.17) with equation (2.3) and squaring the result gives $(\mathbf{k_0} + \mathbf{G})^2 = \mathbf{k}^2$. For elastic scattering, the length of $\mathbf{k_0}$ and $\mathbf{k}$ is the same and $k_0^2 = k^2$. We find $2\mathbf{k} \cdot \mathbf{G} + G^2 = 0$ or, by using that $-\mathbf{G}$ is also a reciprocal lattice vector [36]:

$$2\mathbf{k} \cdot \mathbf{G} = G^2 \tag{2.18}$$

With equation (2.10) this can be written as $2(1/\lambda)\sin(\Theta) = 1/d_{hkl}$ or

$$\boxed{\lambda = 2d_{hkl}\sin(\Theta)} \tag{2.19}$$

which is known as *Bragg's law*. Bragg's law is very helpful in describing the position of diffraction peaks in angular space.

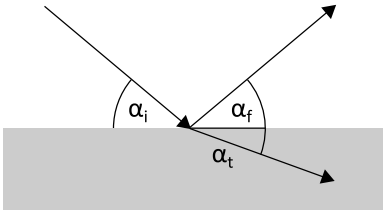

Figure 2.2.: Illustration of the incident beam (with angle α_i), the reflected beam (α_f) and the transmitted beam (α_t).

2.1.4. Refractive index for X-rays

Before the two X-ray scattering techniques used in this work are described in more detail, a peculiarity of those methods has to be looked at. Since the investigated films are ultrathin (even in the submonolayer range) with a thickness (d) of the order of nm, one challenge is to get as much signal from the layers and as little signal from the substrate as possible.

Both of the methods work at very small incident angles to increase the path length (l) of the X-rays in the sample which is $l = d/\sin(\Theta)$. In this region, reflection and refraction play an important role and the simplifications taken above are not valid any more. The effects can conveniently be explained by starting from the Helmholtz equation, which explains the propagation of an electromagnetic plane wave in a material [37]

$$\Delta\mathbf{E}(\mathbf{r}) + k^2 n^2(\mathbf{r})\mathbf{E}(\mathbf{r}) = 0 \tag{2.20}$$

where $n(\mathbf{r})$ is the index of refraction, which is the ratio of the speed of light in vacuum to the one in a material ($n = c_0/c_m$).

The refractive index can be expressed as

$$n(\mathbf{r}) = 1 - \delta(\mathbf{r}) + i\beta(\mathbf{r}) \tag{2.21}$$

where $\delta(\mathbf{r})$ is called the dispersion term and can be expressed by

$$\delta(\mathbf{r}) = \frac{\lambda^2}{2\pi} r_e \rho_e \tag{2.22}$$

with the classical electron radius r_e and the electron density ρ_e and $\beta(\mathbf{r})$ is the absorption term

$$\beta(\mathbf{r}) = \frac{\lambda}{4\pi}\mu(\mathbf{r}) \tag{2.23}$$

with the linear absorption coefficient of the material $\mu(\mathbf{r})$.

For X-rays, $\delta(\mathbf{r})$ is always positive and of the order of 10^{-6} and $\beta(\mathbf{r})$ is of the order of 10^{-8}. Therefore the real part of the refractive index for X-rays is always (but only slightly) smaller than unity. By inspection of Snell's law,

$$n = \frac{\cos(\alpha_i)}{\cos(\alpha_t)} \tag{2.24}$$

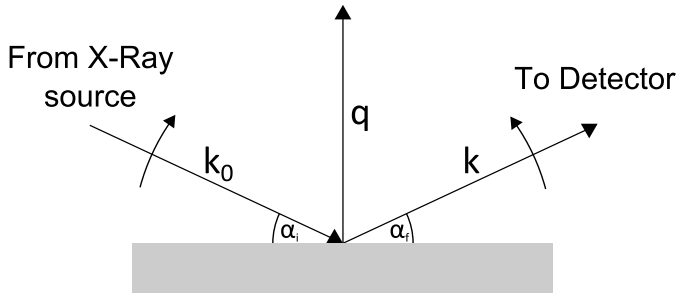

Figure 2.3.: Schematic representation of the geometry of an XRR experiment.

where α_i and α_t are the angle of the incident and the transmitted beam with respect to the surface (see figure 2.2), an interesting feature of X-rays can be explained. In general the beam will go from air or vacuum into a material with a bigger value $\delta(\mathbf{r})$. Therefore, below a critical angle α_c, total external reflection can be observed. By neglecting absorption and very small terms, a simple relation for α_t can be found

$$\alpha_t = \sqrt{\alpha_i^2 - 2\delta} \tag{2.25}$$

For total external reflection $\alpha_t = 0$ and we find the following condition for α_c

$$\alpha_c = \sqrt{2\delta} = \lambda\sqrt{\frac{r_e\rho_e}{\pi}} \tag{2.26}$$

If CuK$_\alpha$ radiation ($\lambda = 1,542\,\text{Å}$) is used, the critical angle α_c of silicon oxide is around $0,22\,^\circ$ and of DOTT it is around $0,16\,^\circ$.

2.1.5. X-ray reflectivity

X-ray reflectivity or XRR is an X-ray scattering technique where the X-ray source and the detector are moved simultaneously in specular condition, which means that the angle of the incoming and the outgoing wave are the same $\alpha_i = \alpha_f$ (see figure 2.3). The scattering vector ($\mathbf{q}$) is perpendicular to the surface. Moreover the investigated angular range is from zero degrees up to only a couple of degrees. In section 2.1.4 it is shown that the critical angle falls into this region and therefore information about δ and β is contained in the scattered waves. This, and the fact that due to the grazing angles only the volume close to the surface is probed, makes XRR a suitable method for the investigation of thin or ultrathin films.

The measured quantity in the experiment is the intensity of the reflected X-rays. By using the fact that the tangential component of the electric field has to be continuous for the incoming, the reflected and the transmitted wave it is possible to derive the ratio between the incoming (I_0) and the reflected intensity (I_R) from the Fresnel coefficients [34]:

$$I_R(\alpha_i) = I_0 \cdot \left| \frac{\alpha_i - \sqrt{\alpha_i^2 - \alpha_c^2 - 2i\beta}}{\alpha_i + \sqrt{\alpha_i^2 - \alpha_c^2 - 2i\beta}} \right|^2 \tag{2.27}$$

from equation (2.4) one gets

$$\begin{aligned} q_z &= 2\,|\mathbf{k}|\sin(\alpha_i) \\ q_c &= 2\,|\mathbf{k}|\sin(\alpha_c) \end{aligned} \tag{2.28}$$

and equation (2.27) can be transformed to

$$I_R(\mathbf{q}) = I_0 \cdot \left| \frac{q_z - \sqrt{q_z^2 - q_c^2 - \frac{32\pi^2 i\beta}{\lambda^2}}}{q_z + \sqrt{q_z^2 - q_c^2 - \frac{32\pi^2 i\beta}{\lambda^2}}} \right|^2 \tag{2.29}$$

In figure 2.4 a simulation for a semi infinite SiO_2 substrate shows the typical characteristics of equation (2.29). There are three distinct regions which are separated by the critical angle Θ_c or in this case q_c.

1. $q_z < q_c$: The total external reflection causes a plateau with nearly constant reflectivity.
2. $q_z > q_c$: The amount of the reflected intensity decreases because more and more intensity is transmitted into the material. For high q_z the slope scales like $\frac{q_c^4}{16 q_z^4}$.
3. $q_z \approx q_c$: In the region around the critical angle, a transition from region 1 to region 2 occurs.

For a real surface, the roughness will not be zero as assumed here and the slope is even steeper [34].

Reflectivity of a Single layer

A situation of practical and technological interest (which is also observed for DOTT in this thesis) is the formation of a single layer with a thickness (d) on top of a substrate. Next to the reflection on the uppermost surface, also reflected waves from the interface, which then get transmitted at the surface, contribute to the total detected intensity. Since some intensity is always reflected back into the single layer, an infinite series of reflections has to be summed and the phase shift has to be considered to get the full intensity. The first three contributions to this series are labeled A, B and C in figure 2.5a and result from the following sequence of reflection and transmission:

A: The incident wave gets reflected at the interface (0→1). The amplitude of the reflected wave is named r_{01}.

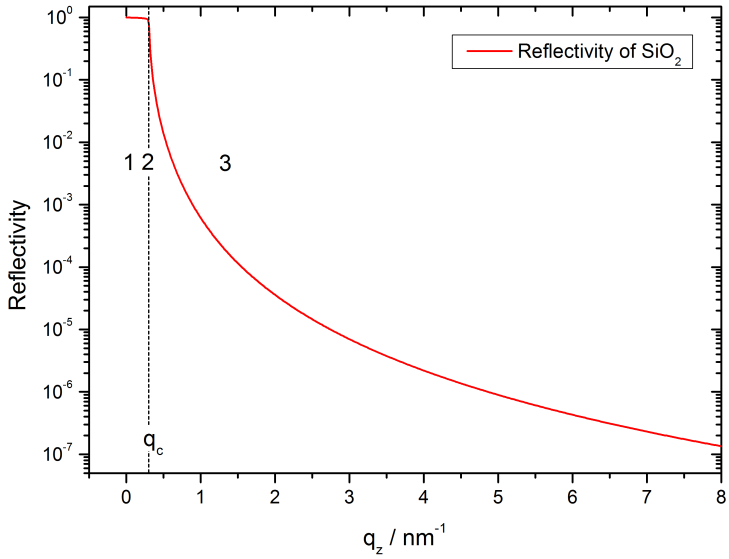

Figure 2.4.: Simulated XRR measurement for a semi-infinite SiO_2 substrate with a roughness of $\sigma = 0$.

B: The wave is first transmitted at (0→1) with amplitude t_{01}, reflected at (1→2, r_{12}) and finally transmitted at (1→0, t_{10}).

C: Here it is transmitted at (0→1, t_{01}), reflected at (1→2, r_{12}), reflected at (1→0, r_{10}), reflected at (1→2, r_{12}) and then transmitted at (1→0, t_{10}).

As already mentioned, a phase factor has to be considered. Therefore, for every reflection or transmission event, a factor of $p = \mathrm{e}^{iqd}$ is multiplied with the amplitude. The summation of the amplitudes of the reflected waves looks like

$$r_{sum} = r_{01} + t_{01}r_{12}t_{10}p^2 + t_{01}r_{12}r_{10}r_{12}t_{10}p^4 \cdots \tag{2.30}$$

By including all the higher order reflections, a geometric series can be found. Further transformation (see [33] for more details) leads to the simple equation for the amplitude of the reflection from a single layer:

$$r_{sum} = \frac{r_{01} + r_{12}p^2}{1 + r_{01}r_{12}p^2} \tag{2.31}$$

In figure 2.5b, the characteristic features of the reflectivity from a single layer can be seen. One finds a similar behavior as for the reflection from a substrate, but on top of the $1/q^4$ decrease there are oscillations, that were first described by H. Kiessig in 1931 [38] and are called *Kiessig fringes* after him. The inverse of the period of the fringes is proportional to the thickness (d) of the layer. This can be used to determine the thickness with high precision [33].

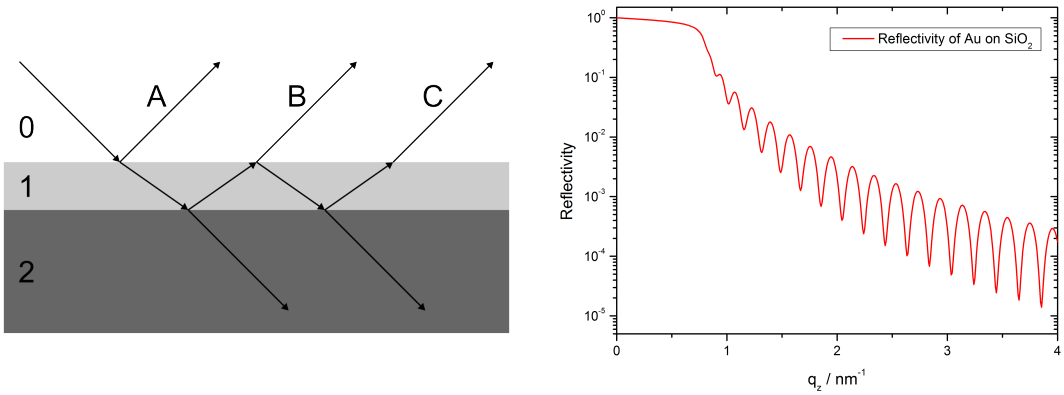

(a) (b)

Figure 2.5.: (a) Reflection and transmission from a single layer on top of a semi infinite substrate. The detected intensity is the sum of an infinite series of reflections of which the first three are shown here and are labeled A, B and C. (b) Simulated XRR measurement with a 30 nm thick gold layer on top of a SiO_2 substrate.

Reflectivity from Multilayers

If not only one but more layers are on top of the substrate, the basic ideas described above are still valid. However the summation over all possible waves reaching the detector gets more complicated. X-rays may be detected after a number of transmission and reflection events from different layers.

For the fits in this work, a method developed by L. G. Parratt in 1954 [39] is used. It is based on the exact result of equation (2.31). A recursive procedure extends the convenience of this equation for multilayer systems:

The method starts from the layer next to the surface. If n layers are on top of the surface, it is defined that this layer is the n'th layer. It is again supposed that the substrate is infinitely thick. Then no multiple reflection from the n'th layer/substrate interface is possible and the Fresnel relation is the exact result for the reflectivity of the n'th layer:

$$r'_{n,substrate} = \frac{k_n - k_{substrate}}{k_n + k_{substrate}} \tag{2.32}$$

The reflectivity for layer $n-1$ is then described by equation (2.31):

$$r_{n-1,n} = \frac{r'_{n-1,n} + r'_{n,substrate} p_n^2}{1 + r'_{n-1,n} r'_{n,substrate} p_n^2} \tag{2.33}$$

This approach is repeated recursively for the next layers up to the uppermost layer and the total reflectivity amplitude r_{01} is the expected result [33].

Parratt's recursive method is implemented in most available software for fitting XRR measurements, like in PANalytical X'Pert Reflectivity, which is used for the fits

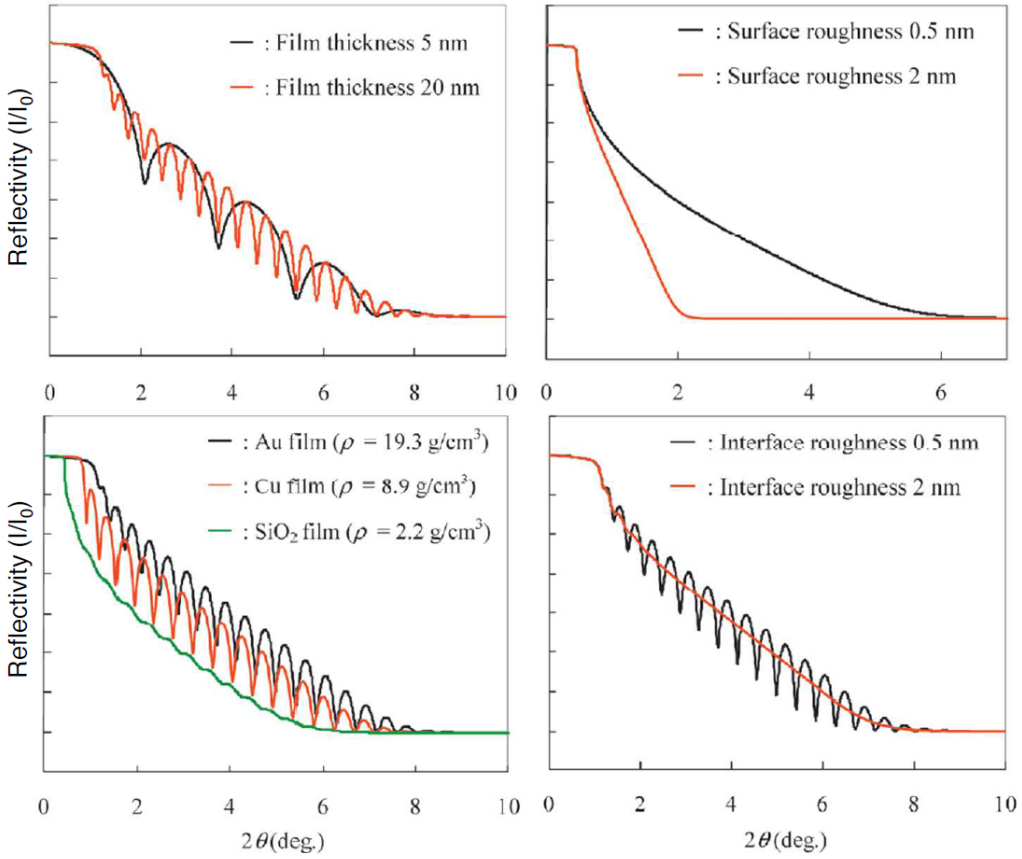

Figure 2.6.: Overview of the influence of the different properties of the layers on the reflectivity. From top left to lower right: Film thickness, surface roughness, electron density of the layer and interface roughness. (reprinted from [40] and modified)

in this work. From fitting the measurements one gets information about the thickness of all layers down to the nanometer range as well as the electron densities of the layers. In figure 2.6 it is shown that also the surface and the interface roughness have an influence on the reflectivity and can therefore be determined in the fits.

2.1.6. Grazing incidence X-ray diffraction

The second surface sensitive X-ray technique used in this work, grazing incidence X-ray diffraction (GIXD), is based on the principles of section 2.1.3, but the incident angle α_i is kept close to the critical angle α_c. At grazing angles close to the critical angle, the penetration depth is very low and therefore the surface sensitivity high. Equation (2.1) can be used to get information about the penetration depth. Inside the material we have the transmitted electromagnetic wave

$$\mathbf{E}_t(\mathbf{r}, \mathrm{t}) = t \cdot \mathbf{E} \cdot \mathrm{e}^{i(\mathbf{k_t}\cdot\mathbf{r}-\omega \mathrm{t})} \tag{2.34}$$

By using Snell's law (equ. (2.24)), equation (2.21) and the fact that the x-component

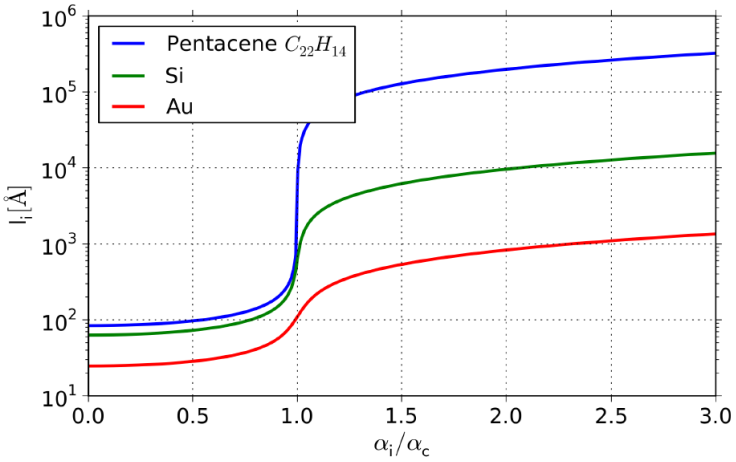

Figure 2.7.: Penetration depth l_i of Pentacene, Silicon and Gold as a function of the incident angle. (reprinted from [41])

is constant

$$\mathbf{E}_t \propto t\mathrm{e}^{i(k_0\cos(\alpha_i)x+\mathrm{Re}\{k_{t,z}\}z)}\mathrm{e}^{-\mathrm{Im}\{k_{t,z}\}z} \tag{2.35}$$

can be derived. For small angles and neglecting absorption we find for the z component of the wavevector:

$$k_{t,z} = k\sqrt{\alpha_i^2 - \alpha_c^2} \tag{2.36}$$

If the incident angle is below the critical angle ($\alpha_i < \alpha_c$), $k_{t,z}$ gets imaginary. The wave is damped exponentially and the resulting wave is traveling parallel to the surface. The penetration depth of this so called *evanescent wave* is

$$l_i = \frac{1}{\mathrm{Im}\{k_{t,z}\}} \tag{2.37}$$

which is plotted in figure 2.7 and shows that below α_c the penetration depth is of the order of 1-10 nm [37].

Because the incident and the outgoing wavevector ($\mathbf{k_0}$ and $\mathbf{k}$) are almost parallel to the surface of the sample, this is also true for the scattering vector $\mathbf{q}$. From section 2.1.3 it is known that $\mathbf{q}$ is perpendicular to the probed lattice planes. Therefore GIXD is perfectly suited to investigate the in-plane crystallographic structure of the thin films. This makes it a complementary method to XRR, where the out-of-plane film thicknesses are probed.

A schematic measurement setup is shown in figure 2.8a. The detector is moved around the sample with the in-plane angle φ and to some extend also with the out-of-plane angle β. The intensity of each point is usually transformed from angular space into reciprocal space and plotted in a so called *reciprocal space map* with the in-plane

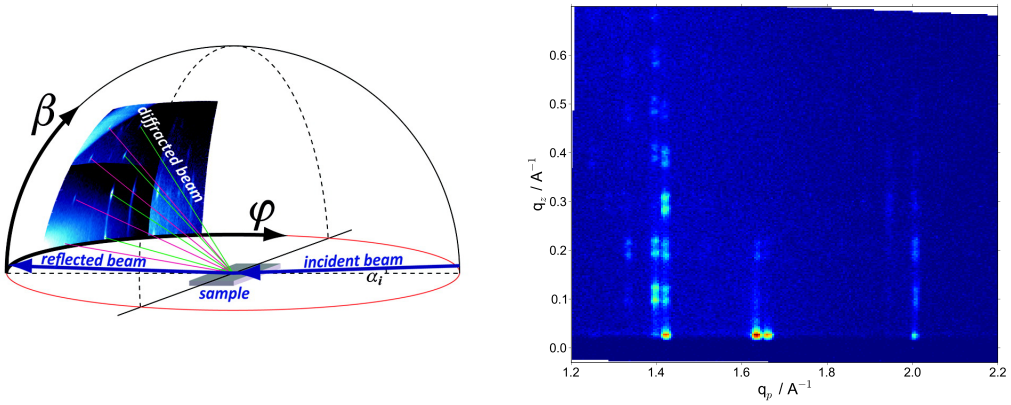

(a) **(b)**

Figure 2.8.: (a) Schematic measurement setup of a GIXD experiment. The detector is moved around the sample and the measured intensity is shown in a contour map. (reprinted from [43]) (b) Example of a reciprocal space map for DOTT where the coordinates were transformed from angular space to reciprocal space.

component of the scattering vector ($\mathbf{q_{xy}} = \mathbf{q_p}$) on the x-axis and the out-of-plane component ($\mathbf{q_z}$) on the y-axis. A detailed description of this transformation can be found in [42]. An example of a reciprocal space map is shown in figure 2.8b.

2.2. Atomic force microscopy

Atomic force microscopy (AFM) is a scanning probe technique that was first developed by G. Binnig *et al.* in 1986 [44]. It is especially applicable for the investigation of organic thin films, since in contrast to scanning tunneling microscopy (STM) no conducting surface is required. Also the fact that AFMs can operate under ambient conditions makes them popular in a great number of academic and industrial applications. In this work it is a valuable tool to image and measure the morphology of thin films directly (see figure 2.9b) and serves as a second complementary method to challenge the results obtained from the X-ray scattering experiments.

In figure 2.9a, the basic layout of an AFM is depicted. A sharp tip at the free end of a cantilever scans the surface. Close to the surface, the tip interacts with the surface and the cantilever is deflected by a number of forces (e.g. weak attractive, electrostatic and mechanical forces). A photodiode detector receives the laser light that is reflected from the backside of the cantilever. Thereby very fast and small deflections of the cantilever can be measured.

There are three basic modes of operation for an AFM [45].

1. In **contact mode**, the tip is in permanent contact to the sample. The feedback electronics keep either the height of the tip or the force on the tip constant.

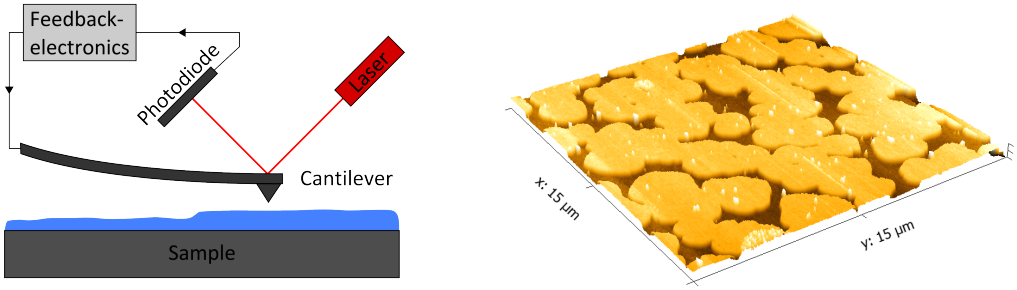

(a) (b)

Figure 2.9.: (a) Basic layout of an AFM. (b) AFM image of a DOTT submonolayer. The morphology of the layer can be seen directly and the height can be measured.

In constant height mode, the force on the sample is used to image the surface height. In constant force mode, the motor position monitors the height of the sample directly. In soft materials the tip can get stuck and the cantilever may be destroyed. Furthermore the sample itself may be damaged by the tip, which is dragged over the surface.

2. These problems are circumvented in **non-contact mode**. The cantilever is oscillated at or near its resonance frequency with the tip positioned above the surface without touching it. Due to the interactions with the surface the frequency is altered. From this frequency shift, information about the sample surface can be extracted.

3. In **tapping mode**, the oscillating tip is closer to the sample and already touches it. The deflection of the cantilever is monitored and the topographic information gained. The contact to the sample and the damage on the surface is minimized and therefore this mode is often used for soft materials.

2.3. Contact angle measurement

In section 1.1.2, the importance of the surface energy of the substrate for thin film growth has already been presented. In this section a simple method to measure the surface energy is explained. The method is based on the measurement of the contact angle of the substrate. If a drop of liquid is placed on a rigid surface, there are three interfaces: The solid/gas (SG), the solid/liquid (SL) and the liquid/gas (LG) interface. The contact angle is defined as the angle between the liquid/gas and the solid/liquid interface. Young's equation connects the contact angle (Θ) with the interface tension[1] of the three interfaces [46]:

$$\gamma_{SG} = \gamma_{SL} + \gamma_{LG} \cos\Theta \tag{2.38}$$

[1]For liquids, the term surface/interface tension if often used instead of surface/interface energy.

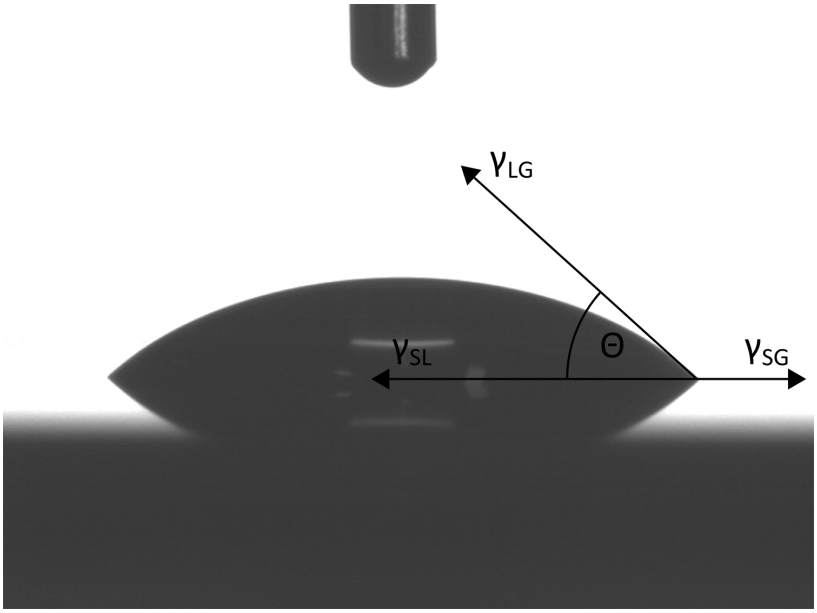

Figure 2.10.: Drop of liquid on a flat surface and the mirror image of the drop with the definition of the three interface tensions and the contact angle for Young's equation.

where γ_{SG}, γ_{SL} and γ_{LG} are the interface tension of the solid/gas, the solid/liquid and the liquid/gas interface respectively. Figure 2.10 shows the image of a contact angle measurement with the liquid drop (and its mirror image) on a surface. The overlay depicts the definition of the contact angle in equation (2.38).

Owens and Wendt argued that the total surface energy can be separated in a dispersive (γ^d) and a polar (γ^p) part, which have their origin in different intermolecular interactions [47]:

$$\gamma = \gamma^d + \gamma^p \tag{2.39}$$

In contact with another phase, the surface energy will be lower due to the interaction between the two phases (phase 1 and phase 2). However, only the respective parts interact with each other and therefore the total interface tension between two phases can be written as

$$\gamma_{12} = \gamma_1 + \gamma_2 - 2\left(\sqrt{\gamma_1^d \cdot \gamma_2^d} + \sqrt{\gamma_1^p \cdot \gamma_2^p}\right) \tag{2.40}$$

Owens, Wendt, Rabel and Kaelble [47, 48] developed a method to calculate the surface energy by measuring the contact angles of two different liquids. Since the difference is small, they set the surface and the interface energy of solids or liquids in contact with a gaseous phase equal ($\gamma_{SG} = \gamma_S$ and $\gamma_{LG} = \gamma_L$). By combining equations (2.38), (2.39) and (2.40) they found

$$\frac{(1+\cos\Theta)\,\gamma_L}{2\sqrt{\gamma_L^d}} = \sqrt{\gamma_S^p}\sqrt{\frac{\gamma_L^p}{\gamma_L^d}} + \sqrt{\gamma_S^d} \tag{2.41}$$

If the contact angles of two liquids, with different and known γ^d and γ^p, are measured, the total surface energy can be calculated.

3. Experimental setup

In the following sections, the experimental setups used in this work are described. First the detailed setup for the XRR and the GIXD measurements is given followed by the parameters used for AFM and contact angle measurements. Last, the sample preparation is explained in detail.

3.1. PANalytical Empyrean

For the XRR measurements, a PANalytical Empyrean Θ/Θ diffractometer was used (see figure 3.1). The tube moves on the ω circle and the detector on the 2Θ circle. With this design, the sample stage does not move but stays horizontal during an experiment.

The diffractometer is equipped with a copper seal tube. A multilayer mirror collimates the beam in horizontal direction but also works as a monochromator to suppress the $Cu_{K\beta}$ radiation. After the multilayer mirror, the X-rays have a wavelength of $\lambda = 0,154178\,\text{nm}$ and the divergence is below $0{,}055\,^\circ$. The sample is placed on a 3-axis cradle with which allows a precise alignment in the beam. The scattered intensity is detected by a PIXcel^{3D} detector which can work in three different modes (0D, 1D, 2D).

The adaptation to the actual measurement is possible due to changeable optics both on the primary and the secondary side. On the primary side there are two slits (the primary slit and the beam mask) to restrain the height and the width of the beam. A programmable beam attenuator with a 0,125 mm Ni plate protects the detector from high intensities that occur at very low angles. On the secondary side, Soller slits decrease the axial divergence. A secondary slit is placed before the detector to improve the angular resolution.

For the XRR measurements in this work the setup in table 3.1 was used, if not noted otherwise.

Table 3.1.: Standard setup for XRR measurements with the PANalytical Empyrean.

primary slit	$1/32\,^\circ$
beam mask	10 mm
secondary slit	0,1 mm
Soller slits	0,02 rad
detector	0D receiving slit mode

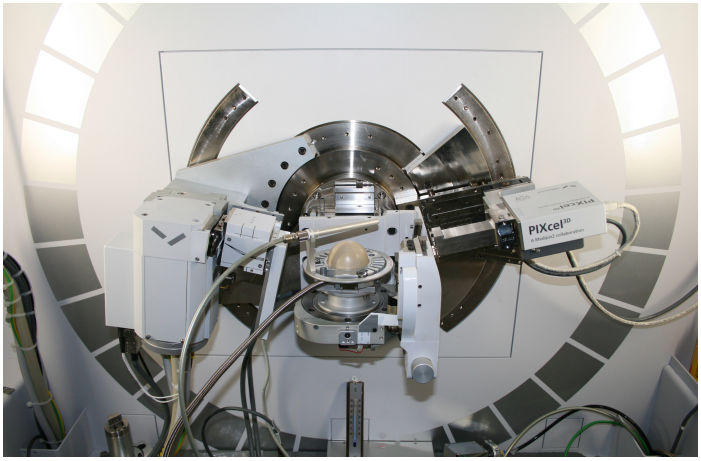

Figure 3.1.: The PANalytical Empyrean diffractometer. The components are explained in the text.

The fits were done with the PANalytical software *X'Pert reflectivity 1.3* based on Parratt's formalism introduced in section 2.1.5.

3.2. Bruker D8 Discover

The in-house GIXD measurements were performed on a Bruker D8 Discover (see figure 3.2). The 4-circle diffractometer is upgraded with the Bruker Ultra-GID add-on. This add-on allows to rotate the X-ray tube and set the incident angle (α_i) between -3,5 ° and 6,5 °. The setup for the GIXD measurements is the following:

1. Copper X-ray tube ($\lambda = 0,154\,\text{nm}$) mounted on the Bruker Ultra-GID add-on (1a) for the rotation of the tube.
2. Multilayer mirror that collimates the beam and acts as monochromator. The equitorial divergence goes down to 0,025 °.
3. Primary slit. (In this work, a primary slit of 0,6 mm is used)
4. Soller slits to decrease the in-plane divergence to 0,35 °.
5. 6-axis cradle to align the sample in the beam. A perfect alignment is crucial for GIXD measurements, therefore M. Neuschitzer describes this process very accurately in the appendix of his thesis [41].
6. Secondary Soller slits. The in-plane detector acceptance is reduced to 0,35 °.
7. PSD Vantec-1 detector. The detector covers an out-of-plane range of 7,3 °.

Since the Bruker D8 Discover and the Vantec-1 detector are not primarily build for GIXD measurements, the data acquisition and visualization needs an adapted

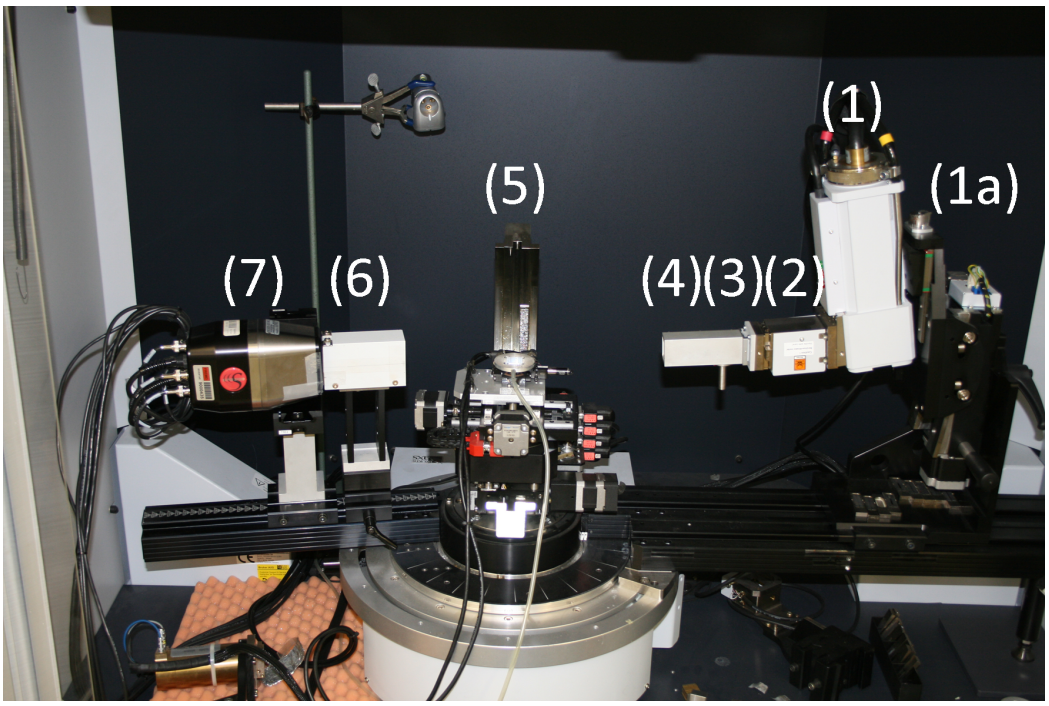

Figure 3.2.: Image of the Bruker D8 Discover with Bruker Ultra-GID add-on for GIXD measurements. A detailed description can be found in the text.

software package. The scripts that are needed next to the original Bruker software XRD Commander and a manual for alignment and data acquisition can be found in [41]. For data visualization and conversion A. Moser developed a Python software called PyGID. This software can import a number of raw data files not only from the Bruker D8 Discover but also from some synchrotron beamlines directly [42]. Data from other sources can be imported as xy-tables. Transformation to reciprocal space and indexation of the Bragg peaks are a feasible task with it.

The standard integration time was 480 s per step and the step size 0,05 °. The incident angle was set to $\alpha_i = 0,18\,°$ which is above the critical angle of DOTT ($\alpha_c = 0,16\,°$) but below the one of silicon oxide which is around $\alpha_c = 0,22\,°$.

The detector is limited to a range of 7,3 ° and can not be rotated to higher out-of-plane angles. Nevertheless M. Neuschitzer *et al.* compared the results of GIXD measurements on the Bruker to those measured at a synchrotron. They showed that the resolution and the intensity of the laboratory equipment is sufficient to resolve Bragg rods of pentacene monolayers [49]. However the measurement time is a limiting factor. To get a comparable quality, a typical measurement of the DOTT samples at the Bruker D8 Discover took around 48 hours compared to 20 min at the beamline W1 at HASYLAB. In section 1.3 it is already noted that organic semiconductors can be unstable in ambient conditions, but also the energy introduced by the X-ray beam can cause chemical or morphological changes [50]. A measuring time of two days can be too long and the properties that one was interested in the experiment may have changed already. This is particularly true for monolayers. To overcome this problem,

a measurement at a synchrotron source is necessary.

3.3. HASYLAB W1 beamline

The beamline W1 was attached to the storage ring DORIS III at DESY in Hamburg before it was shut down in October 2012. A wiggler in combination with a silicon double crystal monochromator allowed the adjustment of the energy in a wide range. For the beamtime in October, where all GIXD measurements, except the in-house ones, presented in this work were performed, the wavelength was set to $\lambda = 0,11807\,\text{nm}$. The resolution and the zero channel of the detector, which are needed for the import in PyGID, were $cpd = 302,353$ and $c_0 = 638,745$. The beamline was equipped with a 6+2 circle heavy load goniometer, which allowed to make both, XRR and GIXD measurements.

The setup of the experiment is shown in figure 3.3 and consists of the following:

- A primary slit system to adjust the beam size.
- The sample stage, which is covered by an X-ray transparent graphite dome. The graphite dome is constantly flushed with Helium to reduce possible beam damage due to the formation of reactive radicals.
- A secondary vertical and horizontal slit system and a flight tube. The resolution can be adjusted by changing the size of the window with the slits.
- The detector is a one-dimensional position sensitive MYTHEN detector. An out-of-plane range of $4\,^\circ$ is covered in one shot and the detector can be rotated to reach higher out-of-plane values.

3.4. Asylum Research AFM

Atomic force microscopy was done with an Asylum Research MFP-3D Stand Alone AFM in tapping mode in ambient conditions. The measurements were performed at the Montanuniversität Leoben. NT-MDT high resolution non-contact silicon cantilevers with gold coating on the reflective side and a tip curvature radius of 10 nm (NSG30) were used. All images were processed with the open source data visualization and analysis software *Gwyddion* [51].

3.5. Krüss DSA100

A Krüss DSA100 contact angle measuring system at the TU Graz Institute for Chemistry and Technology of Materials was used for the contact angle measurements. Drop shape analysis of the static sessile drops was done with the software *DropShapeAnalysis* provided by Krüss together with the instrument. The drops had a volume of

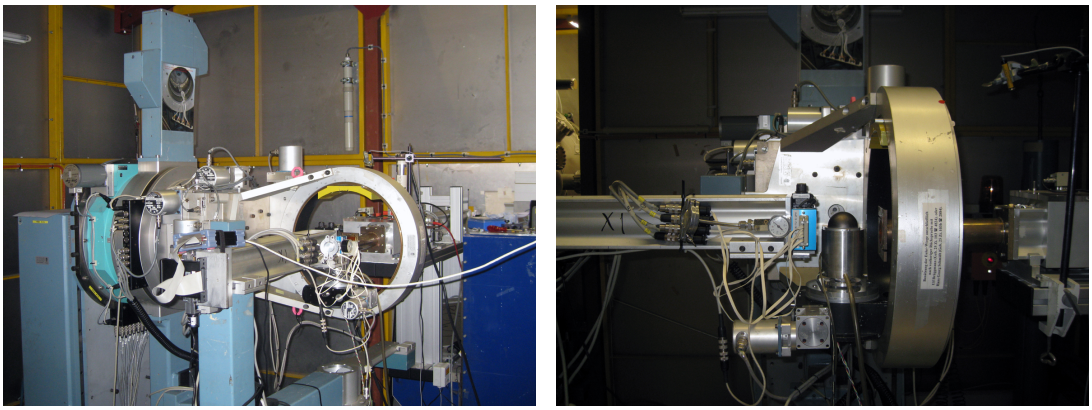

(a) (b)

Figure 3.3.: (a) 6+2 circle heavy load goniometer at the beamline W1. The beam enters from the right side. (b) The sample stage with graphite dome followed by the slit system and the flight tube towards the detector.

3 μl and were placed with a speed of 200 μl/min. The contact angle was measured for different liquids: Diiodomethane, benzyl alcohol, water and glycerol. Surface energies were calculated with the method of Owens, Wendt, Rabel and Kaelble (see section 2.3).

3.6. Anton Paar DHS 900

For the annealing measurements, the standard sample stage of the PANalytical Empyrean was exchanged with an Anton Paar DHS 900 heating stage. This stage allows to control the temperature in-situ in a range from 25 - 900 °C. The heating and cooling rates can be adjusted from 1 - 200 °C/min. Furthermore, the sample is covered with a highly X-ray transparent plastic dome. The dome has a separate gas supply for helium or nitrogen. It is used to avoid oxidation during the heating experiments.

3.7. Sample preparation

All samples in this work were produced by spin coating DOTT solution on a wafer substrate. Since already slight variations in the preparation can have a severe impact on the films, all parameters, despite the ones under investigation, were kept as constant as possible throughout the whole work.

3.7.1. The silicon substrate

Silicon wafers (150 mm diameter, $\langle 1\,0\,0 \rangle$ orientation) with a 150 nm thermally grown SiO_2 layer on top were used as substrates. The wafers were cut into 20 x 20 mm

pieces and provided by *Siegert Wafer*. The roughness of the wafers before cleaning was determined by XRR and was around 0,5 nm. To ensure stable conditions, a time-tested standard cleaning process was used and conducted directly before spin coating:

- First, the samples are cleaned and rinsed with acteone and dried with compressed CO_2.
- Followed by cleaning and rinsing with isopropyl alcohol and drying with CO_2.
- Then the samples are put in an ultrasonic bath with acetone for 15 minutes.
- When taken out of the ultrasonic bath, they are rinsed with isopropyl alcohol immediately and dried with CO_2.

The cleaning result was checked both with XRR and optical microscopy. After the cleaning process the samples had a roughness of around 0,3 nm (see appendix B).

3.7.2. The solution

Based on the experience of the earlier work of O. Werzer [32], tetrahydrofuran (THF) was used to dissolve DOTT. For some experiments, the solution was heated above the transition temperature of DOTT to the crystal G and liquid crystal phases. For this purpose, toluene was chosen as solvent because of its boiling point of 111 °C compared to the one of THF which is 66 °C. Also, the results at room temperature with THF are compared to the ones with toluene to show the influence of the solvent.

A wide range of differently concentrated solutions was prepared to vary the resulting film thickness. The lowest molecular concentration was 0,12 mg/ml. This leads to films in the submonolayer regime. The highest concentration of 1,88 mg/ml results in films which are around 30 nm thick.

The results vary, if a few days old solution is used (see appendix A for more details). A possible explanation is that DOTT slowly agglomerates in the solution. To avoid an influence of the aging solution, all solutions were prepared directly before they were used.

3.7.3. Spin coating

The samples were produced by spin coating the solution on the wafers as it is shown in figure 3.4. The parameters are the following: 120 μl of solution is placed on the wafer. The wafer is rotated with 1000 rpm for 9 sec followd by 30 sec with 1500 rpm. The same parameters were used for all samples in this work.

For the spin coated samples that were produced at elevated temperature, the whole sample holder made out of copper was heated to the target temperature together with the solution (in a closed flask) and the wafer before spin coating.

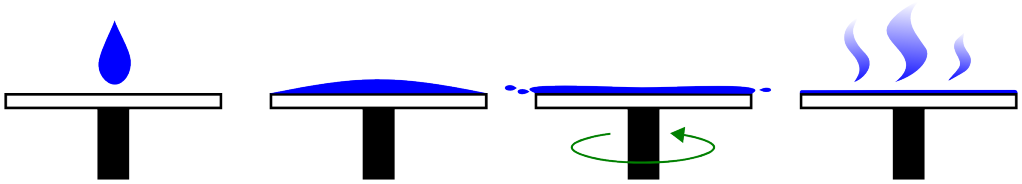

Figure 3.4.: Spin coating process. From left to right: A drop of solution is placed on the substrate. The substrate is wetted. The sample holder is rotated and excess solution is removed by the rotational forces. The remaining solution evaporates and a uniform film remains.

3.8. Crystal growth

Single crystals were grown from toluene solution. The solution was made with around 50 mg of DOTT and 5 ml of toluene was added. The solution was stirred overnight and filtered with a 0,45 μm PTFE filter. 1 ml of the solution was then pipetted onto a watch glass. The watch glasses were covered with beakers and aluminum foil to vary the evaporation rate.

4. Results and discussion

From the earlier work of Oliver Werzer *et al.* [32] a number of different phases of DOTT are already known (see also section 1.4). The work so far was focused on thick films in the range of 100 nm. The question arises: How do these films evolve? How does the surface influence the formation of the different phases and is it possible to control, which phase is present? In this chapter it is tried to answer these questions. The starting point for the considerations is the bare substrate. From there, the first layer of DOTT (section 4.2) and then thicker films are added step by step in section 4.3. Finally, the influence of the temperature is studied. During the sample preparation, it is varied from 25 °C to 55 °C. In a separate annealing step after the preparation, the samples are heated above the transition temperature to the crystal G phase (section 4.5). A single crystal phase is explored in the first section. The crystallographic unit cell of this phase is used to calculate the position of the surface induced phases in terms of the thermodynamic stability and the equilibrium state.

4.1. A single crystal phase

Single crystals were grown according to section 3.8. A structure solution was performed by Roland Fischer from the Institute of Inorganic Chemistry at the Graz University of Technology.

The solution found has an R-factor of 5,4 % and a wR^2-factor of 11,7 %. The space group is P c a 2_1. The asymmetric unit cell consists of four and the unit cell of 16 molecules. The complete solution can be found in table 4.1. Figure 4.1 shows the resulting structure. The molecules adopt a herringbone packing which is a common arrangement for conjugated organic molecules. The volume of the orthorhombic unit cell is 10348 Å^3. To be able to compare the volume and the density of this single crystal phase with surface induced phases, the parameter **a** is divided by two and the parameter **c** by four. The resulting unit cell contains two molecules and can be compared directly with the found unit cells in the following sections. From this values, the density can be calculated: $\rho_{sc} = 1,21\,\mathrm{g/cm^3}$. This serves as a reference point for a phase without the influence of a surface.

4.2. The monolayer

To learn how the first monolayer evolves, a number of samples were prepared from solutions with a low concentration between 0,12 mg/ml and 0,43 mg/ml.

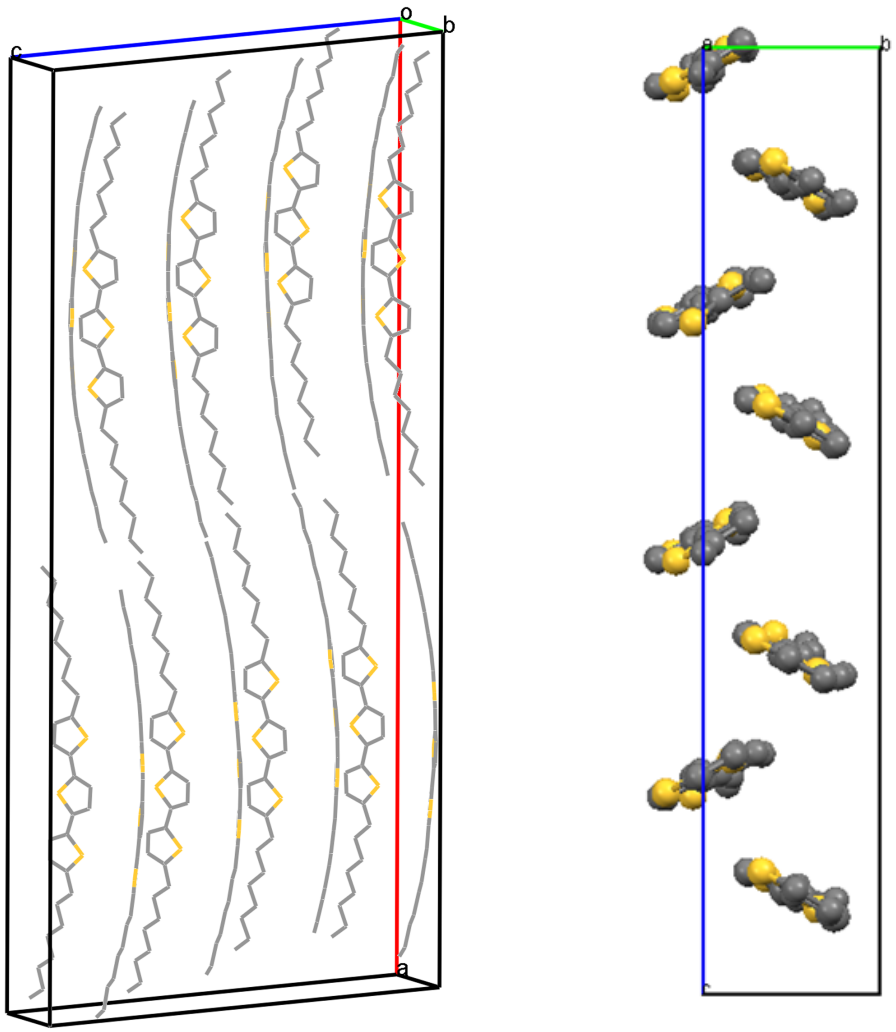

(a) **(b)**

Figure 4.1.: (a) Three dimensional representation of the packing structure of a DOTT single crystal solution. (b) Top view on the packing structure with the herringbone packing clearly visible.

Table 4.1.: Single crystal solution for DOTT crystals grown from toluene solution.

DOTT	
Formula	$C_{28}H_{40}S_3$
Space group	P c a 2_1
Crystal system	orthorhombic
Cell lengths (Å)	
a	63,465(2)
b	5,5248(2)
c	29,5109(12)
Cell angles (°)	
α	90,00
β	90,00
γ	90,00
Cell volume (Å^3)	10347,5(7)
Molecules in unit cell	16
Total number of reflections	26474
R-factor (%)	5,39
wR^2-factor (%)	11,72

4.2.1. Optical microscopy

First, optical microscopy images were made with an Olympus BX51 microscope to reveal the morphology of the films. A blue filter was used to increase the contrast between substrate and organic layer. The images of six samples from different solutions are shown in figure 4.2. It is worth mentioning that the layer thickness is in the nanometer range but there is still enough contrast to distinguish the substrate and the different layers in the optical microscopy images.

At very low concentration (0,12 mg/ml) a huge number of small single layer DOTT islands is visible. With increasing concentration, the empty spaces between the islands decreases. At 0,37 mg/ml, the substrate is completely covered with DOTT and only a small number of voids is visible. For higher concentrations, the next layers start to grow on top of the monolayer in small islands.

The ratio between covered and total substrate area is measured with image analysis techniques. The determined coverage for the six samples in figure 4.2 can be found in table 4.2. The dependence between the concentraton and the surface coverage is depicted in figure 4.3. From the linear fit, the concentration to achieve a complete layer is found to be $(0,37 \pm 0,01)$ mg/ml.

4.2.2. X-ray reflectivity

To gain information about the out-of-plane molecular order of the first layer, XRR measurements were performed. The measured curves of four samples with increas-

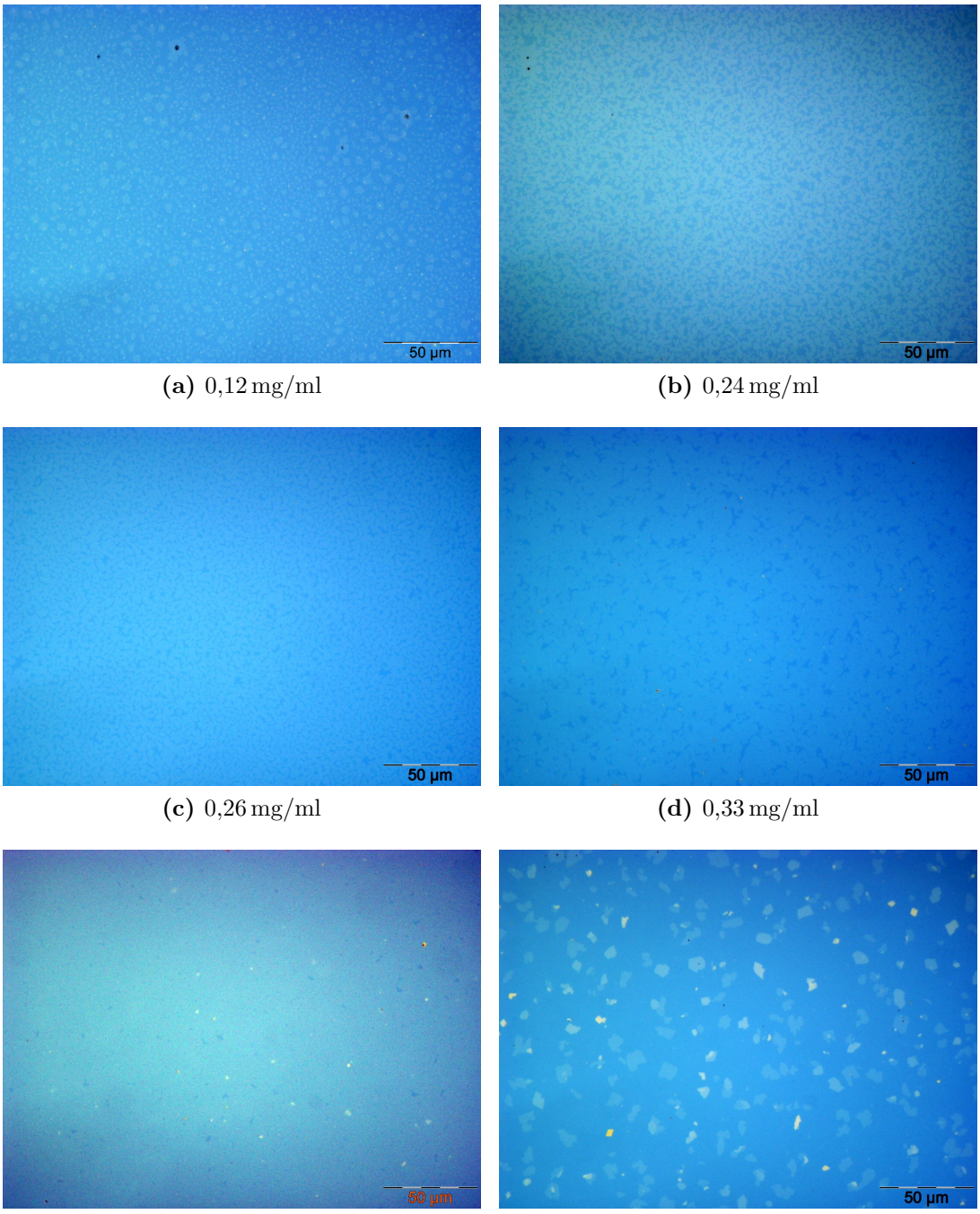

(a) 0,12 mg/ml **(b)** 0,24 mg/ml

(c) 0,26 mg/ml **(d)** 0,33 mg/ml

(e) 0,37 mg/ml **(f)** 0,43 mg/ml

Figure 4.2.: Comparison of optical microscopy images of samples from six different solutions with increasing concentration. The darker blue in images (a) to (e) is the substrate and the lighter blue is the organic layer. In image (f), the first DOTT layer is closed and the light blue small islands belong to the next layers already.

Table 4.2.: Ratio of the covered and total substrate area for the six images in figure 4.2 with the respective concentration of the solution.

concentration / mg/ml	coverage / monolayers
0,12	0,28
0,24	0,70
0,26	0,80
0,33	0,91
0,37	0,98
0,43	1,11

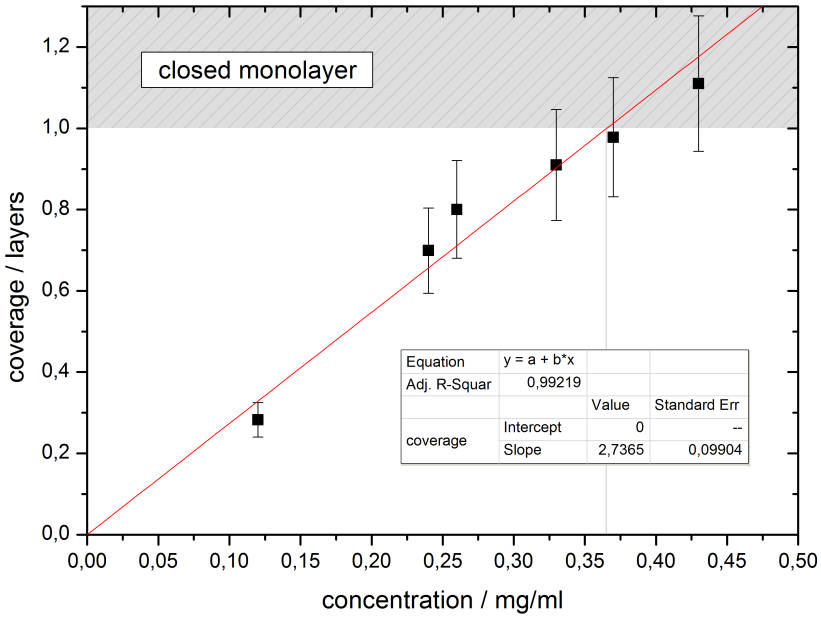

Figure 4.3.: Surface coverage of the DOTT layer as a function of the concentration of the solution used. From the linear fit ($\bar{R}^2 = 0,99$), a slope of $(2,7 \pm 0,1)$ ml/mg can be found. For a completely covered surface, a solution with $(0,37 \pm 0,01)$ mg/ml DOTT has to be used.

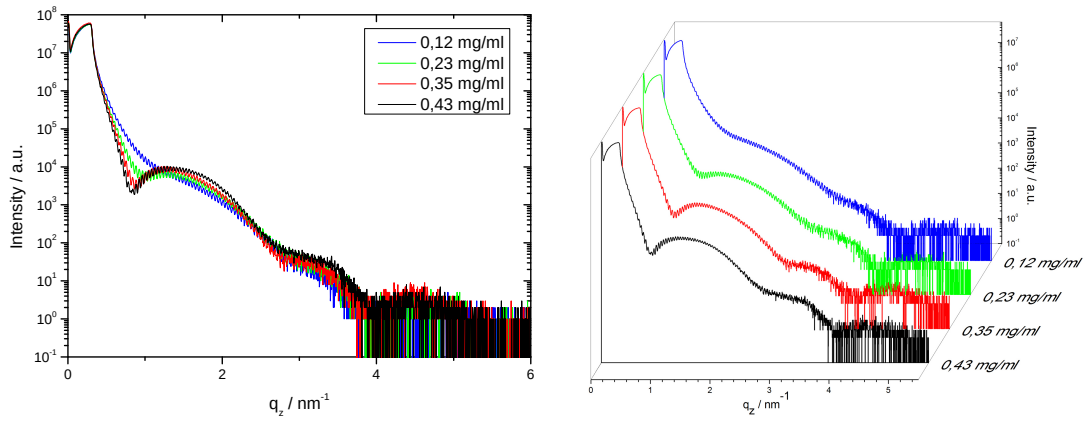

(a) **(b)**

Figure 4.4.: XRR measurements of four samples with increasing concentration of the solution. The fringes get more and more pronounced until the first layer is closed at around 0,37 mg/ml.

ing concentration are displayed in figure 4.4. Already for the lowest concentration (0,12 mg/ml), fringes are visible. Since only around 30 % of the surface are covered at this concentration, the fringes are not very pronounced. With increasing concentration, the fringes get more distinct. For a higher concentration than around 0,37 mg/ml, the layer is completely closed and therefore the fringes of the 0,43 mg/ml sample look very similar to the ones at 0,35 mg/ml. By inspecting the curves the results from the optical microscopy images can be confirmed. The beam size is around the size of the sample, and therefore the measured curves are an average result over the whole sample. Since the fringes are well pronounced, the film is uniform over the whole sample.

By fitting the curve, the thickness of the layer can be obtained. The software *X'Pert reflectivity* fits the data based on a model. A more complex model (i.e. including more layers) will always lead to an apparently better fit since more variables are introduced. However from a physical point of view, one should try to find the best solution with the least layers possible.

Some a priori knowledge is needed to find a suitable model. For dihexyl-terthiophene, a molecule similar to DOTT, Bernhard Wedl *et al.* showed that the molecules are upright standing in the first layer on SiO_x [28]. This is used as a starting point. The electron density is not equal throughout the whole DOTT molecule. The two octyl chains have a smaller density than the molecular backbone in the middle. Based on this considerations, the model in figure 4.5 is used for a fit of a 0,34 mg/ml sample.

Figure 4.6 shows the measured XRR curve and the fit based on figure 4.5. Apparently, the fit has all the features of the measured data. However the values in table 4.3 reveal a problem. The thickness of the octyl chain next to the substrate is 1,58 nm. This is more than the stretched out octyl chain and also the complete DOTT molecule would measure 3,76 nm which is again more than the stretched out

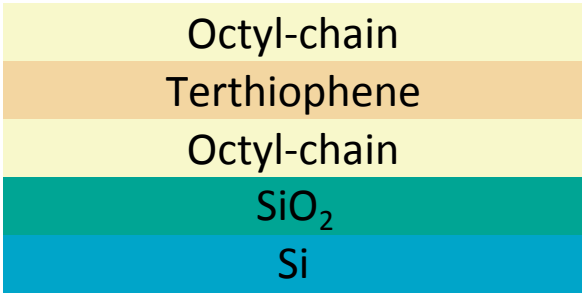

Figure 4.5.: Basic model for the fit of a DOTT monolayer. The upright standing layer of molecules on top of the silicon oxide is separated into three parts: Two octyl chains as first and topmost layer and the terthiophene backbone in the middle.

Table 4.3.: Values for the fit in figure 4.6.

Layer description	Density / g/cm^3	Thickness / nm	Roughness / nm
Octyl	0,8	1,02	0,39
Terthiophene	1,4	1,16	0,46
Octyl	0,6	1,58	0,48
SiO_2	2,2	145,40	0,43

molecule itself. This suggests that the model does not include enough layers. Since the result for the uppermost octyl, the terthiophene in the middle and the SiO_2 layer are in good agreement with the expected values, the second octyl chain is separated into two layers. Next to the substrate, a so called wetting layer is introduced. An analog layer was also found for similar systems [28, 52]. The updated model is shown in figure 4.7.

The updated model (figure 4.7) is used to repeat the fit of the 0,34 mg/ml sample. The result is depicted in figure 4.8. The values in table 4.4 are in good agreement with the expected ones. The two octyl chains have nearly the same density and thickness. The total thickness of the molecule from the fit is 3,26 nm. This means that the molecules are nearly upright standing on the substrate surface. The underlying wetting layer has a density of 0,8 g/cm^3 and a thickness of 0,61 nm. It possibly consists of lying DOTT molecules but also a contribution from the remaining solvent could be an explanation.

4.2.3. Grazing incidence X-ray diffraction

The in-plane-order of the first layer of DOTT on silicon oxide was investigated by GIXD measurements. The reciprocal space map of a 0,44 mg/ml sample is shown in figure 4.9a. Instead of Bragg points, Bragg rods are observed. The strongest intensity for all three rods is found at the critical angle ($q_z = q_c$). This is the typical result of a two dimensional crystal and means that there is only one monolayer of DOTT. It also

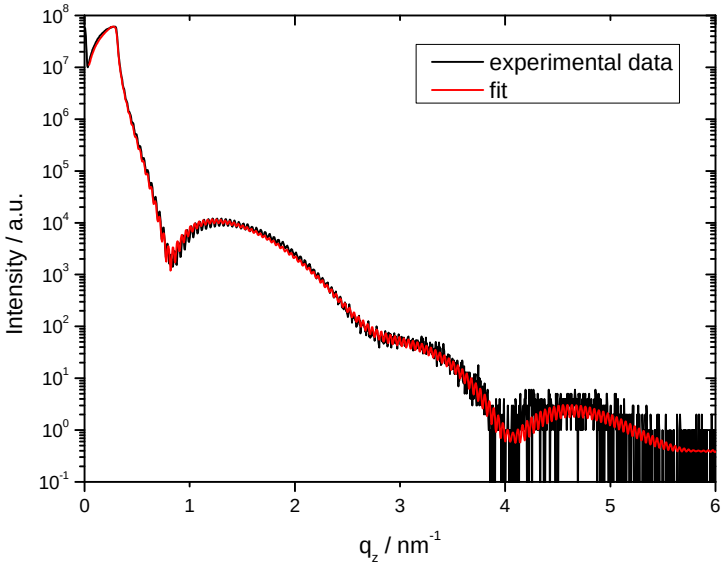

Figure 4.6.: Measured XRR curve for a 0,34 mg/ml sample with fit based on figure 4.5. The values of the fit can be found in table 4.3.

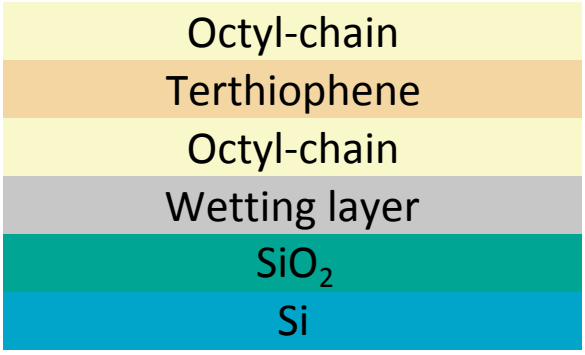

Figure 4.7.: Updated model for the fit of a DOTT monolayer. Below the three layers of the DOTT molecule, a so called wetting layer is included.

Table 4.4.: Values for the fit in figure 4.8.

Layer description	Density / g/cm^3	Thickness / nm	Roughness / nm
Octyl	0,7	0,97	0,35
Terthiophene	1,4	1,24	0,52
Octyl	0,6	1,05	0,47
Wetting layer	0,8	0,61	0,25
SiO_2	2,2	145,30	0,38

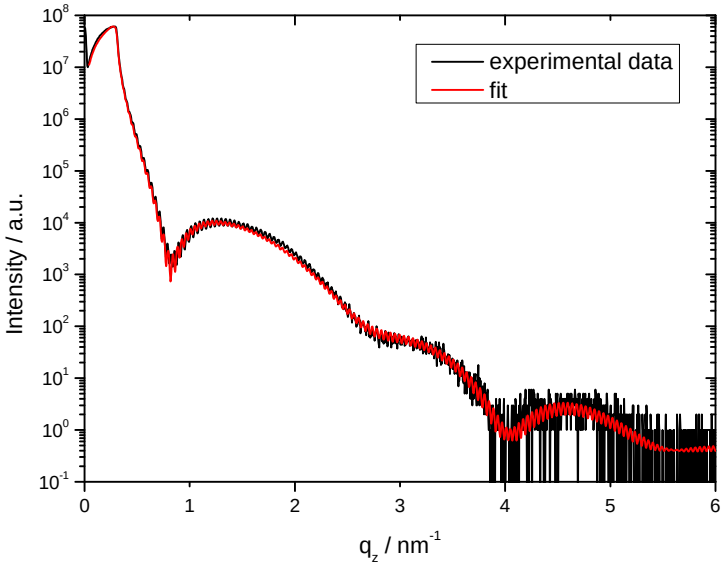

Figure 4.8.: Measured XRR curve for a 0,34 mg/ml sample with fit based on the updated model in figure 4.5. The values of the fit can be found in table 4.4.

approves the results from the XRR measurements in section 4.2.2 that the molecules are upright standing. The three rods in figure 4.9b can be indexed to calculate the in-plane crystallographic unit cell:

$$\mathbf{a} = 0,55\,\text{nm} \quad \mathbf{b} = 0,77\,\text{nm} \quad \gamma = 90\,^\circ \tag{4.1}$$

The presence of an interface monolayer was already noted by O. Werzer [32] (see section 1.4). The indexation above reveals that the molecular order is different to the already known b- and s-phase of thicker films. Therefore another phase of DOTT is found. From now on this phase is referred to as the monolayer- or ml-phase.

With the layer thickness $d = 3,26\,\text{nm}$, the volume and the density of the ml-phase unit cell can be calculated: $V_{ml} = 1,387\,\text{nm}^3$ and $\rho_{ml} = 1,13\,\text{g/cm}^3$.

4.2.4. Atomic force microscopy

Atomic force microscopy images were made to check the layer thickness obtained from the XRR measurements. The images in figure 4.10 also show the morphology of the sub-monolayer to the monolayer region. In figure 4.10a (0,26 mg/ml), the analysis of the height profile gives a layer thickness of 2,9 nm. For figure 4.10b (0,33 mg/ml), the thickness is 3,2 nm. This is in good agreement with the XRR result, which is 3,26 nm for a 0,34 mg/ml sample. With increasing concentration, the first layer gets more and more closed. In figure 4.10c (0,43 mg/ml), the first layer is closed and an island of the second layer is already visible. The height of this second layer is 3,0 nm.

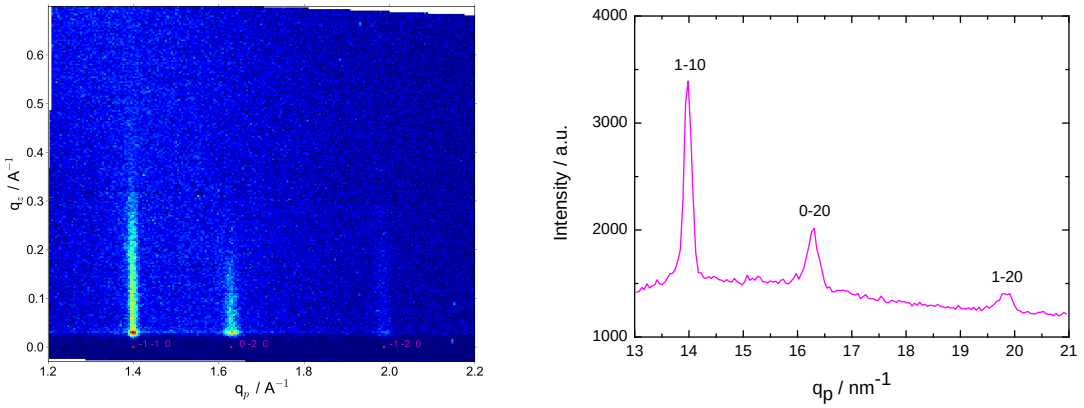

(a) **(b)**

Figure 4.9.: GIXD measurement of a 0,44 mg/ml DOTT sample. (a) Reciprocal space map and (b) integrated linescan (range: $q_z = 0,01 - 0,35\,\mathrm{nm}^{-1}$). Three rods are found and indexed.

Table 4.5.: Values for the fit of the XRR measurement of a DOTT sample from toluene solution in figure 4.11.

Layer description	Density / g/cm^3	Thickness / nm	Roughness / nm
Octyl	0,6	0,88	0,43
Terthiophene	1,0	1,24	0,33
Octyl	0,6	0,90	0,30
Wetting layer	0,8	0,49	0,29
SiO_2	2,2	147,16	0,37

4.2.5. Toluene solution

Threlfall [53] argued that the choice of the solvent may play an important role in the crystallization. Therefore a second solvent, toluene, was used for the sample preparation. The results are similar to the ones with THF. The XRR measurement of a 0,30 mg/ml sample in figure 4.11 is successfully fitted with the updated model, which includes a wetting layer. The layer thickness is 3,02 nm (see table 4.5 for the values). This is consistent with the AFM analysis, where the layer thickness of the 0,26 mg/ml sample is 2,9 nm and therefore also smaller than the one of the closed monolayer (3,2 nm in figure 4.10b).

The same three peaks as in figure 4.9 are visible in the GIXD reciprocal space maps of a toluene monolayer sample with 0,40 mg/ml (see figure 4.12). The peaks are at the same position and therefore the crystallographic unit cell is the same as for THF:

$$\mathbf{a} = 0,55\,\mathrm{nm} \quad \mathbf{b} = 0,77\,\mathrm{nm} \quad \gamma = 90\,^\circ \tag{4.2}$$

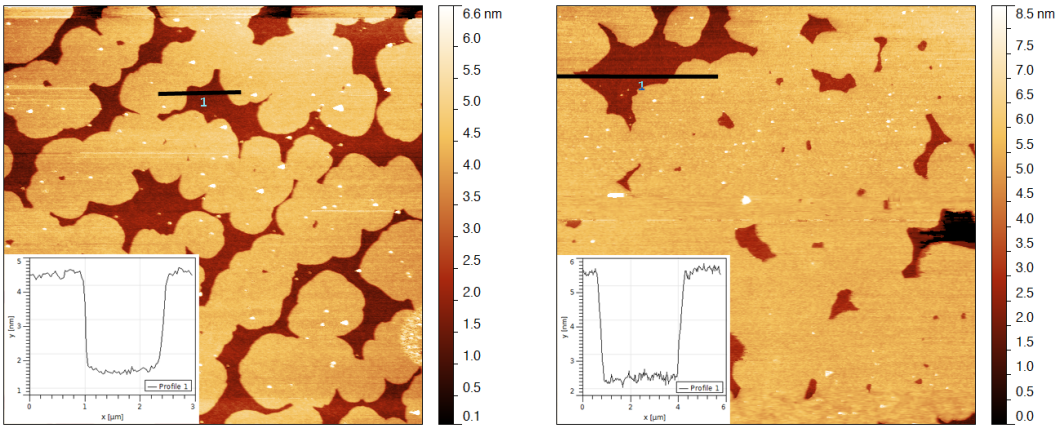

(a) 0,26 mg/ml **(b)** 0,33 mg/ml

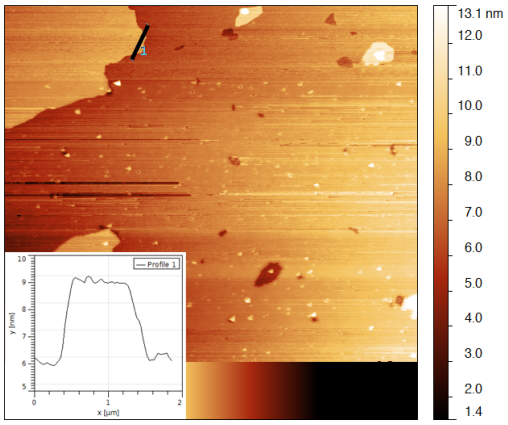

(c) 0,43 mg/ml

Figure 4.10.: 15x15 μm AFM images of three DOTT samples from THF solution with different concentration. The insets show the height profile for region 1 in the images.

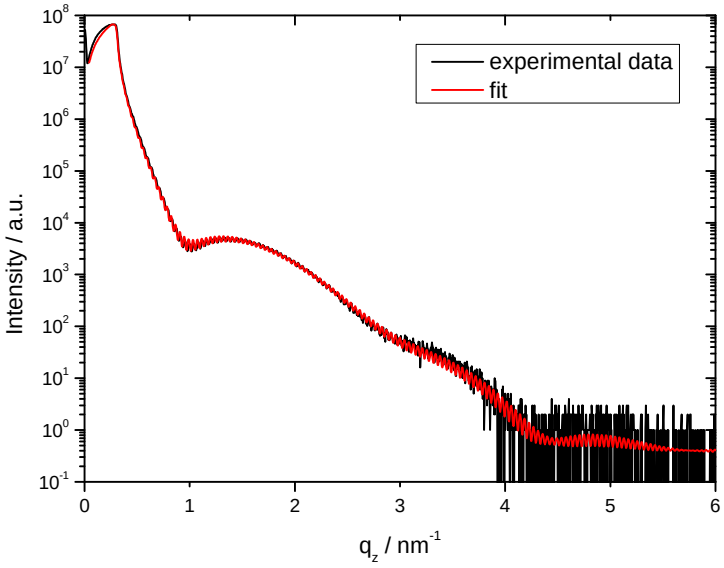

Figure 4.11.: XRR measurement of a 0,30 mg/ml DOTT sample made from toluene solution. The fit is based on the model with a wetting layer included. Fit values are in table 4.5.

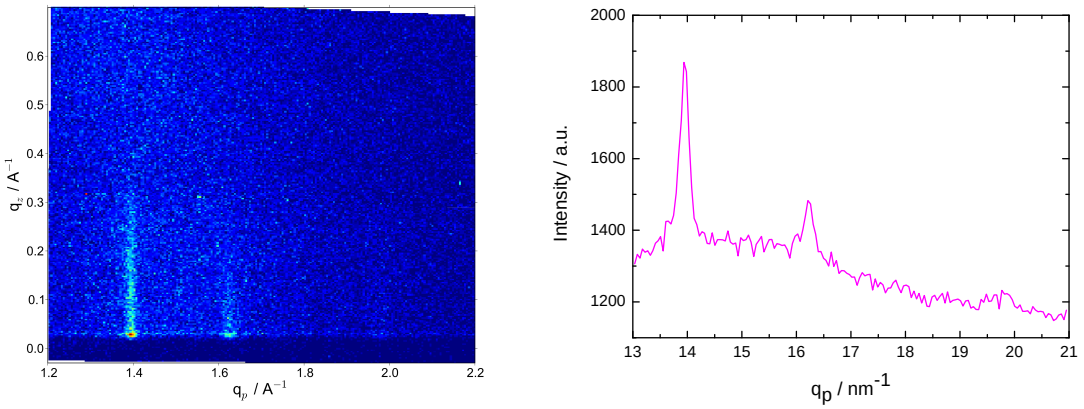

(a) **(b)**

Figure 4.12.: GIXD measurement of a 0,40 mg/ml DOTT sample from a toluene solution. (a) Reciprocal space map and (b) integrated linescan (range: $q_z = 0,01 - 0,35\,\mathrm{nm}^{-1}$). Three rods are found and indexed.

4.3. Thicker films

In the previous section the evolution of the first monolayer was analyzed. The optical and atomic force microscopy images showed that the first layer is closed before the next layers start to grow. The fit and the indexation of the XRR and GIXD measurements revealed a new phase, the ml-phase. In this section the further development of the film is observed. Higher concentrations lead to thicker films. Again I will first concentrate on the morphology and then continue to the molecular order and the crystal structure of the films.

4.3.1. Optical microscopy

The optical microscopy images in figure 4.13 show the morphology of the films with higher concentration. On top of the monolayer, islands start to grow. The number of islands increases with increasing concentration. Different colors indicate that some of the islands are higher than one layer. No closed layer is formed. DOTT therefore grows in layer plus island mode on top of silicon oxide.

4.3.2. X-ray reflectivity

For thicker films, Bragg peaks start to appear on top of the fringes from the monolayer (see figure 4.14a). The diffraction features from the monolayer do not vanish and the fringes are nearly the same for all concentrations. This shows that the monolayer stays intact while the islands grow on top of it. The position of the Bragg peaks can be used to calculate the layer thickness with equation (2.19). From the position of the third and fourth Bragg peak in figure 4.14b, a layer thickness of 3,24 nm is obtained. This is very similar to the value of the b-phase from O. Werzer (3,21 nm) [32]. The width of the Bragg peaks is a measure for the number of layers of the islands. The 1,88 mg/ml sample has islands with a height of approximately 10 layers.

4.3.3. Grazing incidence X-ray diffraction

The GIXD reciprocal space maps (figure 4.15) show the development from a single layer to a typical multilayer 2D powder. The rods start to split into separate peaks. However, the peaks are still on a straight line perpendicular to the sample horizon and at certain q_p-values. For 4.15b the indexation with the ml-phase is sufficient. In 4.15d, the b- and the ml-phase are present. In 4.15f the b-phase is dominant and the intensity of the monolayer rods is too weak compared to the intensity of the b-phase, so they are not visible (The color code in the GIXD images is not constant but scales with the highest intensity). Another meaningful way to plot the GIXD results in two dimensions is to sum up the intensity of a certain range q_z and plot it against the in-plane scattering vector q_p, which is called an integrated linescan. The linescan in figure 4.16 (range $q_z = 0,01 - 0,35\,\mathrm{nm}^{-1}$) supports the findings of the GIXD reciprocal space maps. The linescan of the 0,44 mg/ml sample shows clearly the ml-phase. The

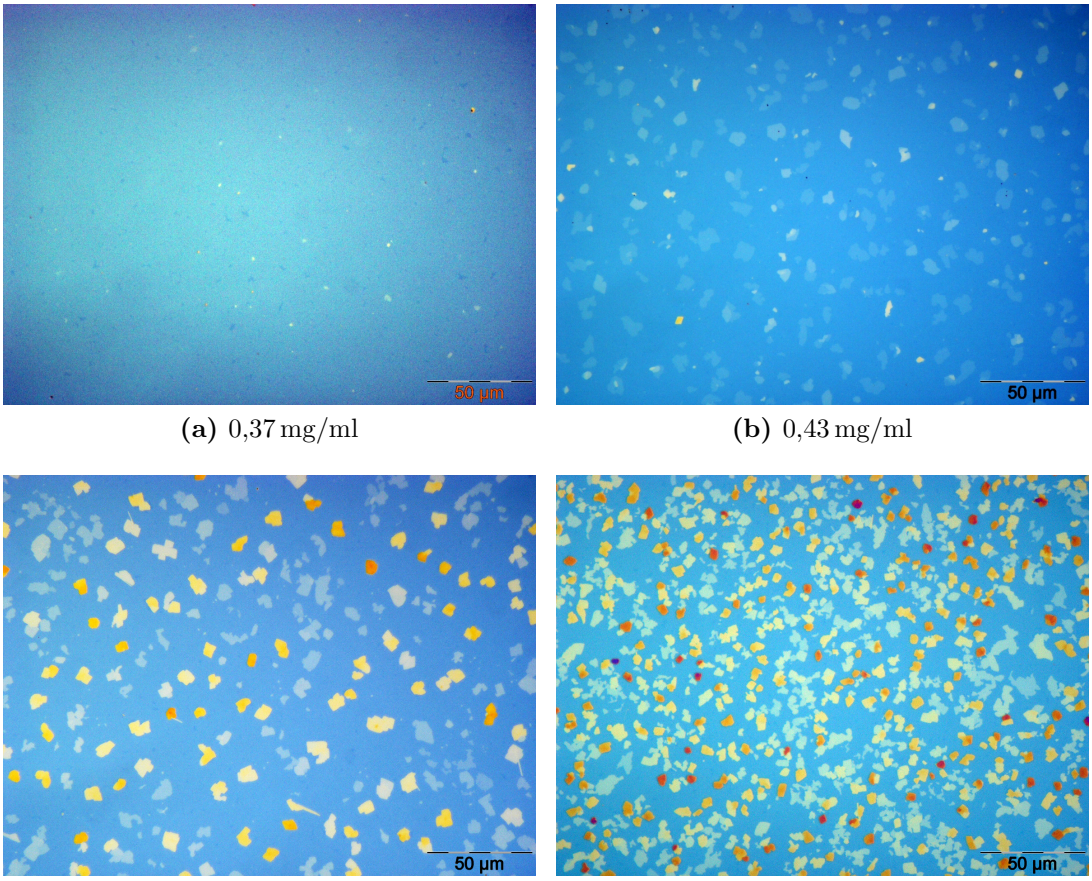

(a) 0,37 mg/ml **(b)** 0,43 mg/ml

(c) 0,92 mg/ml **(d)** 1,88 mg/ml

Figure 4.13.: Comparison of optical microscopy images of DOTT thin film samples from four different THF solutions with increasing concentration. (a) Closed monolayer. (b) - (d) On top of the monolayer, islands start to grow. For higher concentration, the number of islands and (indicated by the different colors) the height of the islands increases but no closed layer is formed any more.

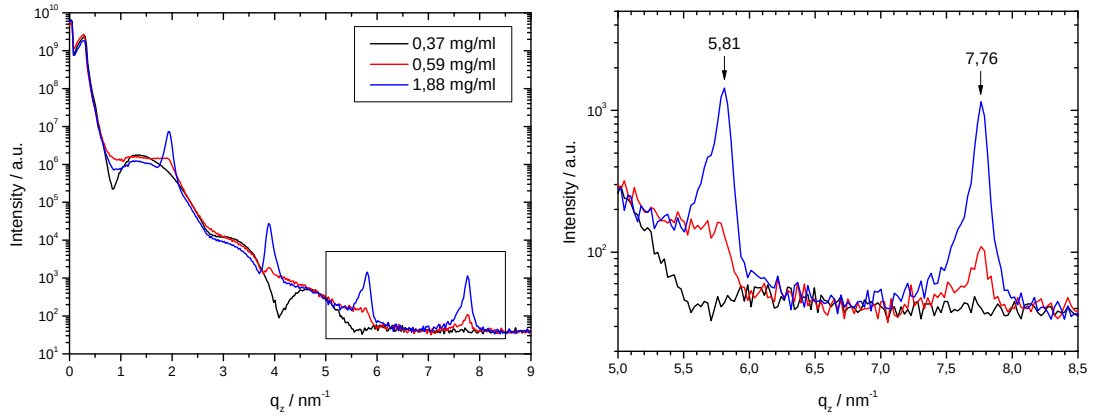

(a) **(b)**

Figure 4.14.: (a) XRR measurements of three DOTT thin films with increasing concentration of the THF solution. On top of the signal from the monolayer, Bragg peaks evolve. Note that the fringes from the monolayer do not vanish. (b) Zoom into the part indicated in the left figure with the position of the peaks.

1,88 mg/ml linescan is dominated by the b-phase and the 0,59 mg/ml one is a mixture of both. The first peak of the 1,88 mg/ml linescan has a small peak on the right side. This peak (and the small one on the left side of the second peak) belongs to the already known s-phase, which is also present in a small amount. The s-phase will be dealt with in section 4.5 and is not further discussed here. The indexation of the b-phase gives the following in-plane unit cell:

$$\mathbf{a} = 0,56\,\text{nm} \quad \mathbf{b} = 0,76\,\text{nm} \quad \gamma = 90\,^\circ \tag{4.3}$$

The peaks in figure 4.15c and 4.15e are split into double peaks. The phenomenon can be explained with the dynamic scattering theory. For more details see [54]. The splitting makes a determination of the unit cell parameter **c** error-prone. Therefore the layer thickness $d = 3,24\,\text{nm}$ from the XRR measurements is taken as the third unit cell parameter. This value has to be doubled to hit all Bragg peaks in figure 4.15f. The resulting unit cell for the b-phase is orthorhombic with the following unit cell parameters:

$$\mathbf{a} = 0,56\,\text{nm} \quad \mathbf{b} = 0,76\,\text{nm} \quad \mathbf{c} = 3,24\,\text{nm} \tag{4.4}$$

The density, that can be calculated from the values above, is $\rho_b = 1,15\,\text{g/cm}^3$. This is considerably higher than the density of the ml-phase ($\rho_{ml} = 1,13\,\text{g/cm}^3$) and indicates that the b-phase is an energetically more favorable phase.

4.3.4. Toluene solution

The thicker samples made from toluene solution have a different morphology than the ones from THF. The optical microscopy image of the toluene sample in figure 4.17b

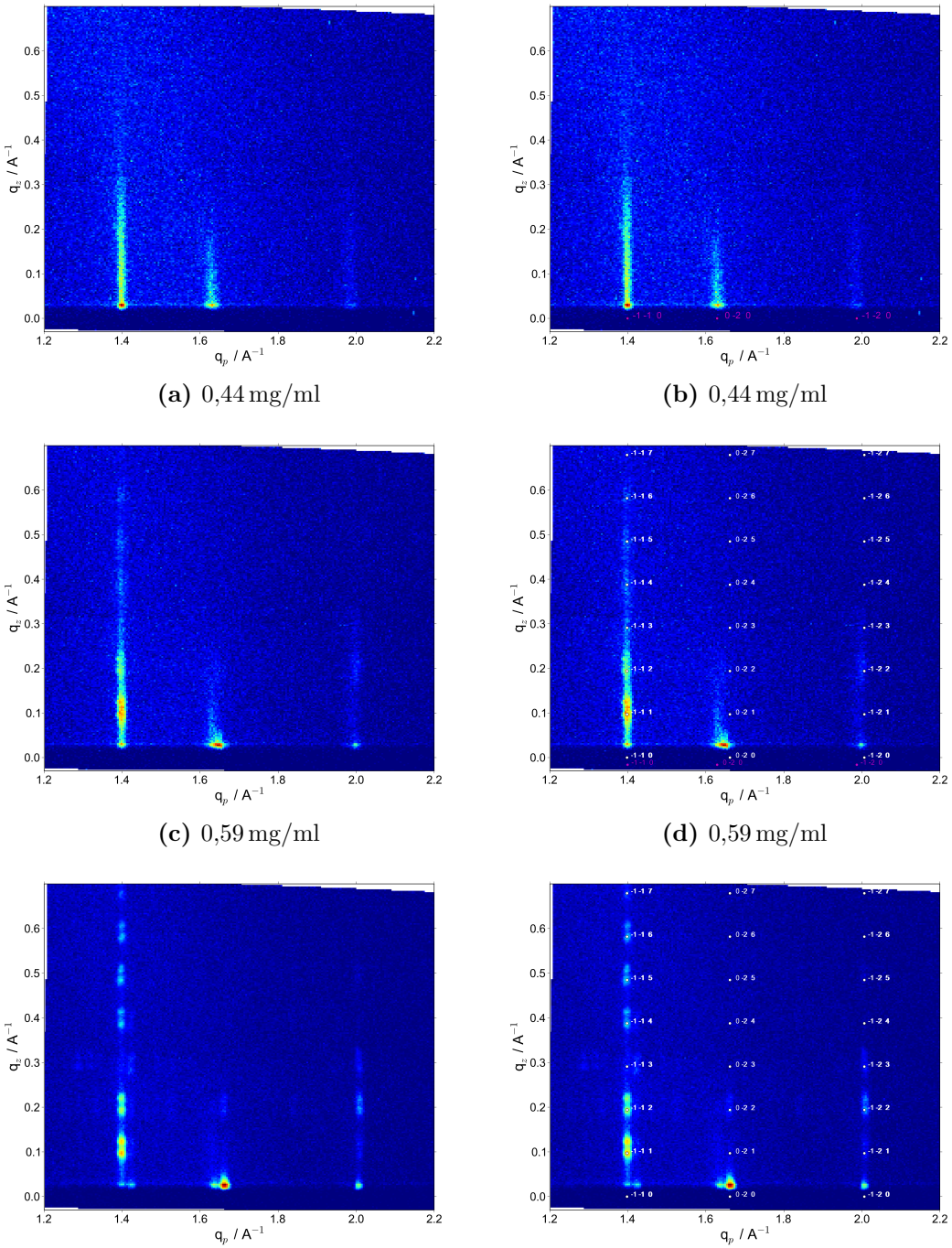

(a) 0,44 mg/ml **(b)** 0,44 mg/ml

(c) 0,59 mg/ml **(d)** 0,59 mg/ml

(e) 1,88 mg/ml **(f)** 1,88 mg/ml

Figure 4.15.: GIXD measurements of three DOTT samples with increasing concentration of the THF solution. (a),(c) and (e) Reciprocal space maps and (b), (d) and (f) indexation with the ml-phase (magenta) and the b-phase (white). For higher concentration, the rods start to split into separate peaks.

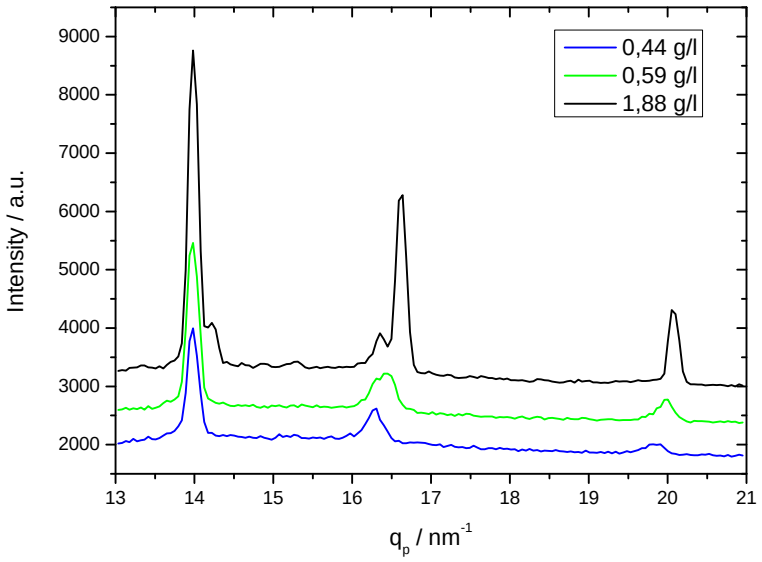

Figure 4.16.: Integrated linescan of the three different GIXD reciprocal space maps from figure 4.15 in the range $q_z = 0,01 - 0,35\,\mathrm{nm}^{-1}$. Curves are shifted for clarity.

also has islands but they do not have sharp edges but have a more drop-like shape with blurred edges.

Despite the different morphology, the X-ray scattering results of the toluene samples are very similar to THF samples. The XRR measurements in figure 4.18 feature the monolayer fringes and the Bragg peaks already observed in the previous section. While the general character is the same, the quality of the films, indicated by the less pronounced fringes and the lower intensity of the Bragg peaks, is worse when toluene is used.

This is also supported by the GIXD images in figure 4.19. Compared to figure 4.16, the measured intensities are lower by roughly a factor of two. The THF and the toluene samples were aligned in the X-ray beam with the same automated script. Since the lower intensity is observed for all toluene samples alike, an alignment effect can be excluded. Also the s-phase peaks next to the ones of the b-phase could be missing because the intensity is lower and therefore they do not emerge from the background. Besides the lower intensity, the features are the same for THF and toluene solution: The rods of the monolayer sample split into separate peaks and a change from the ml- to the b-phase is apparent.

4.4. Plasma etching

It has been shown that the growth mode of organic semiconductors can be controlled by changing the surface-molecule interactions [55]. One way to do this is a modifica-

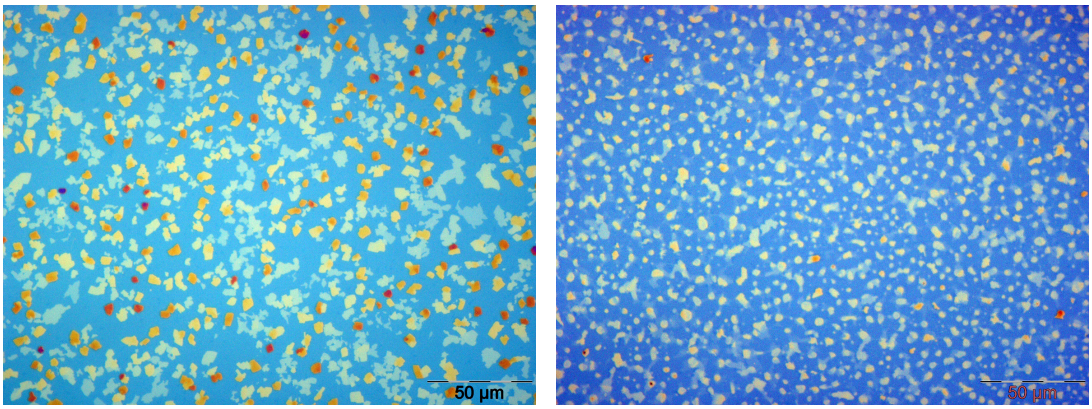

(a) 1,88 mg/ml THF **(b)** 1,82 mg/ml toluene

Figure 4.17.: Comparison of two DOTT samples with similar concentration but from different solution. (a) THF sample with crystalline shaped and sharp edged islands and (b) toluene sample with a drop-like shape and blurred edges.

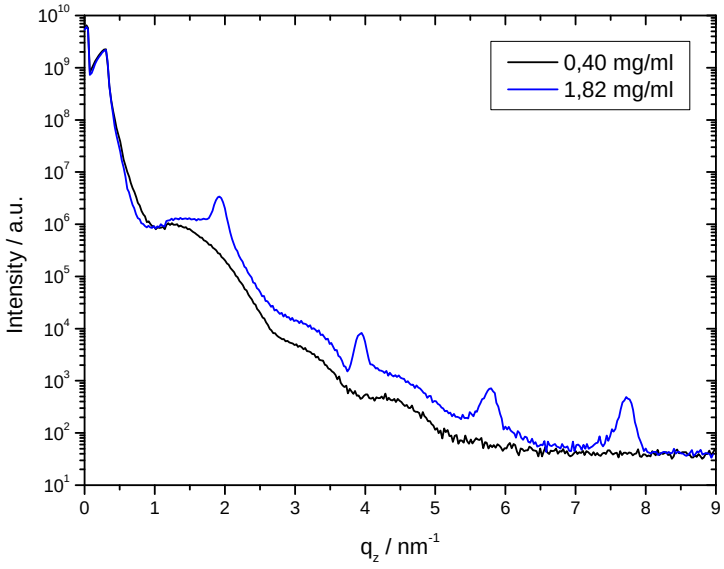

Figure 4.18.: XRR measurement of two DOTT samples from toluene solution with a concentration of 0,40 mg/ml and 1,82 mg/ml. Also with toluene, the monolayer stays intact and the fringes are present next to the Bragg peaks in the 1,82 mg/ml sample.

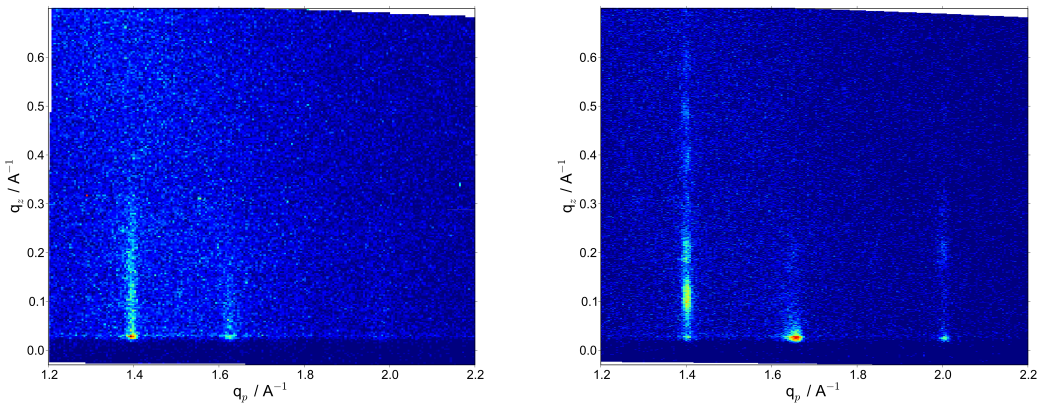

(a) 0,40 mg/ml **(b)** 1,82 mg/ml

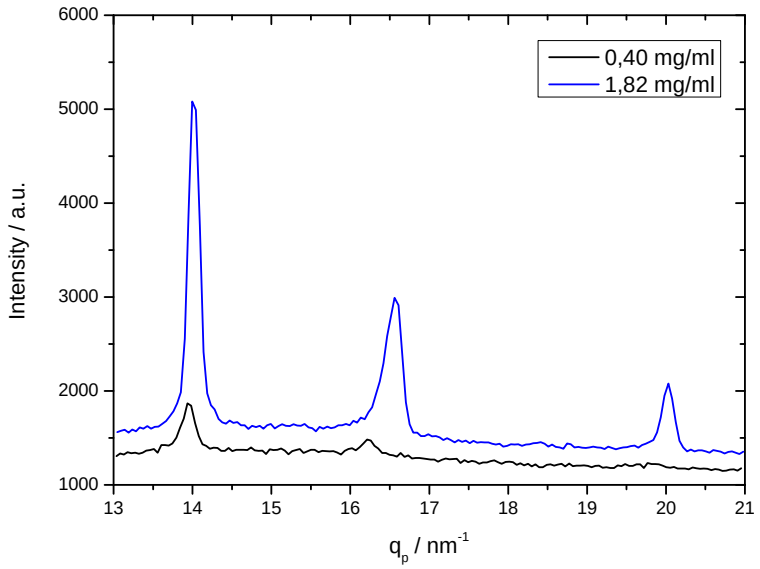

(c)

Figure 4.19.: GIXD measurements of two DOTT samples made from toluene solution. (a) and (b) Reciprocal space maps of a 0,40 mg/ml and a 1,82 mg/ml sample respectively. (c) Linescan in the range of $q_z = 0,01 - 0,35\,\mathrm{nm}^{-1}$. The splitting of the rods into separate peaks and the change from the ml- to the b-phase are observed.

tion of the surface itself. In this section the influence of oxygen plasma etching of the substrate on the DOTT films is investigated.

The substrates were RF-plasma etched for 30 sec with a power of 100 W directly before spin coating. The effect of the etch on the substrate was monitored by contact angle measurements. The surface energy is significantly higher after plasma etching. This is mainly because the polar component of the surface energy increases [56].

Ultra-thin films

The optical microsocopy images of an etched and an unetched DOTT sample from the same 0,37 mg/ml THF solution in figure 4.20 reveal a changed morphology of the ultra-thin films. The first monolayer is closed for both, the unmodified and the plasma etched sample. This can also be seen in the XRR measurements (figure 4.20c), which are basically the same. In the second layer however, the islands have a considerably higher lateral size, if the substrate was plasma etched. The higher surface energy of the substrate therefore leads to a more 2D growth. The GIXD linescans in figure 4.20d confirm that the ml-phase is the predominant one in the first monolayer. As indicated by the position of the missing peaks, no contribution from the b- or s-phase can be seen in both samples.

Thicker films

For thicker films, the change in morphology is not that obvious but the size of the islands is still bigger if the substrate was plasma etched (figure 4.21a and 4.21b). The XRR and GIXD images reveal an interesting development. In the XRR results (figure 4.21c), the two curves are identical but the third and fourth peak. While the curve of the etched sample superposes the non-etched sample on the right side of the peaks, the intensity on the left side is significantly higher. The right side is the position of the b-phase and therefore the same amount of b-phase is found in both samples. The position of the left peak corresponds to the s-phase and thus the amount of s-phase in the etched sample is higher. The plasma etched sample seems to have a higher crystallinity. This is also supported by the GIXD linescan in figure 4.21e. The same situation is found: The b-phase peaks are nearly as high in both samples but the s-phase peaks are considerably higher in the etched sample. Therefore the higher surface energy of the substrate surface after plasma etching enhances the formation of s-phase grains.

4.5. Effects of temperature

In previous works, the s-phase was found to be predominant close to the substrate and the b-phase further away from it. In the last section, an increased surface energy also led to a higher amount of s-phase. In this section the influence of temperature on the ratio between s- and b-phase is investigated in order to get a better understanding of the stability of the different phases. First, the temperature is altered during the

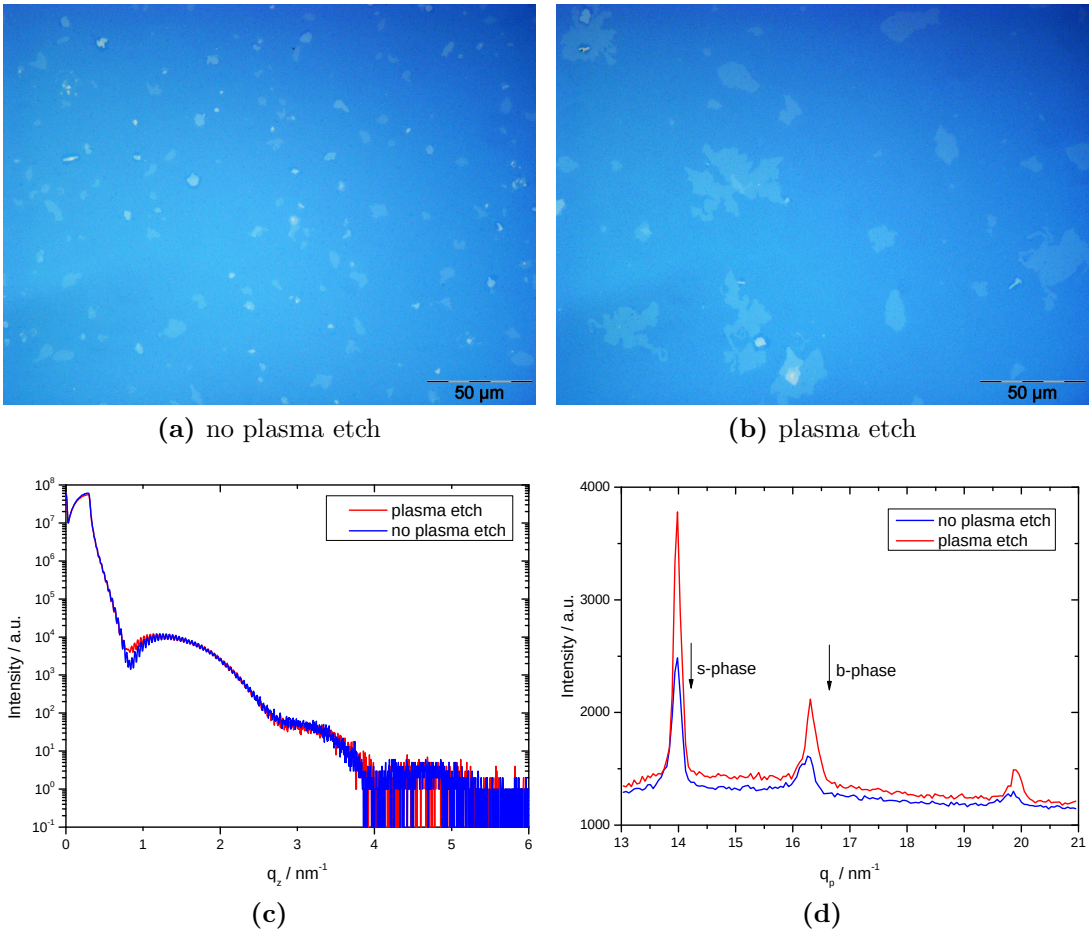

(a) no plasma etch **(b)** plasma etch

(c) **(d)**

Figure 4.20.: Optical microscopy images of a closed DOTT monolayer (0,37 mg/ml THF solution) with some islands on top on (a) an unmodified and (b) a plasma etched substrate. (c) XRR measurement and (d) linescans of GIXD reciprocal space maps of an unmodified and a plasma etched sample. The position of the missing s- and b-phase peaks is indicated.

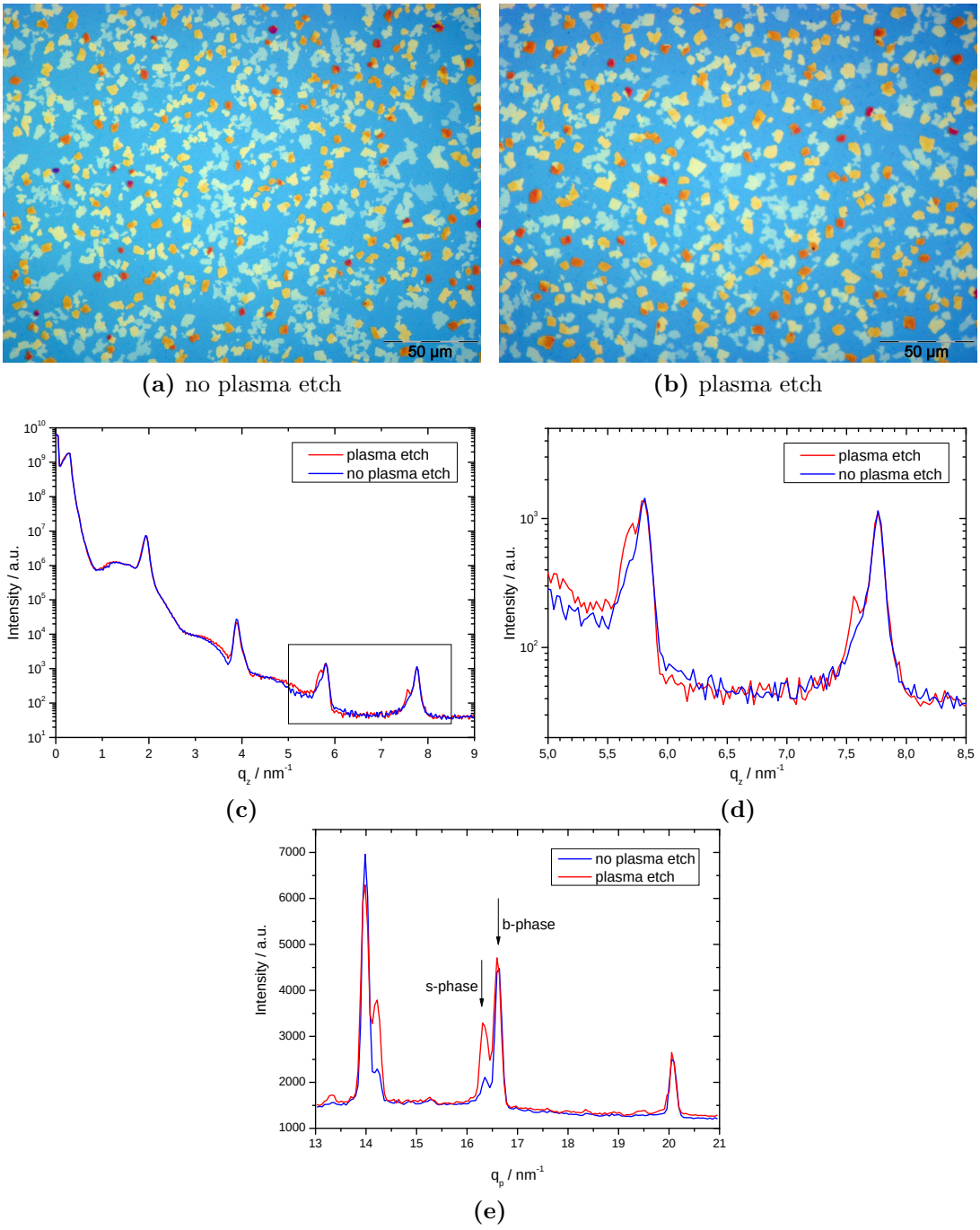

(a) no plasma etch **(b)** plasma etch

(c) **(d)**

(e)

Figure 4.21.: Comparison of optical microscopy images of 1,88 mg/ml samples made from (a) an unmodified and (b) a plasma etched substrate. (c) XRR measurements and (d) zoom into the indicated region. (e) Linescans of GIXD reciprocal space maps.

spin-coating process. This means the samples are fabricated at different temperatures but then kept and measured at room temperature. Then the samples are also heated (or annealed) after the fabrication in section 4.5.2.

4.5.1. Spin-coating temperature

By increasing the temperature during the spin-coating process, the crystallization time is decreased because the solution evaporates faster. A lower temperature on the other hand would give the molecules more time to rearrange into a more stable arrangement. The investigation of samples, made at different temperature, can give more insight into the formation of the different phases and the driving forces behind it.

The samples were produced at three different temperatures: At 25 °C, 40 °C and 55 °C. These temperatures were chosen because of the following reasons:

- From the DSC curve, figure 1.10 in section 1.4.1, it is known that there is a transition to a crystal G phase at 64 °C. This transition can result in completely different films and is therefore not wanted in this section. This is an upper limit for the temperature.
- Samples made from THF showed in general the better results in the last sections which makes it the preferred solution. The boiling point of THF is 66 °C. At temperatures close to the boiling point, the solution evaporates too fast for the spin-coating process to be completed. Around 10 °C below this point is a good value for the highest temperature.
- Due to the simple heating mechanism, the uncertainty of the reached temperature is rather high. A large number of measuring points between room temperature and the highest reasonable temperature is therefore not required.

The elevated temperatures are reached by a heating plate. The sample and the solution are heated on top of it for around 5 min, to give the solution enough time to heat up uniformly. The sample holder of the spin-coater is also heated together with the solution. The heavy metal holder should keep the sample at the target temperature for a long enough time. The temperature was monitored on a roline 305 digital thermometer with a K-type thermocouple on top of the heating plate.

Optical microscopy

Already the optical microscopy images demonstrate a substantial change of the morphology. There is still island growth, but the shape as well as the size of the islands is different in all the images in figure 4.22. The shape at lower temperature is compact while there is a transition to elongated, needle like islands at higher temperature. With increasing temperature, the size of the islands increases as well. While at 25 °C, the typical island diameter is below 10 μm, it is some tens of microns at 55 °C. The

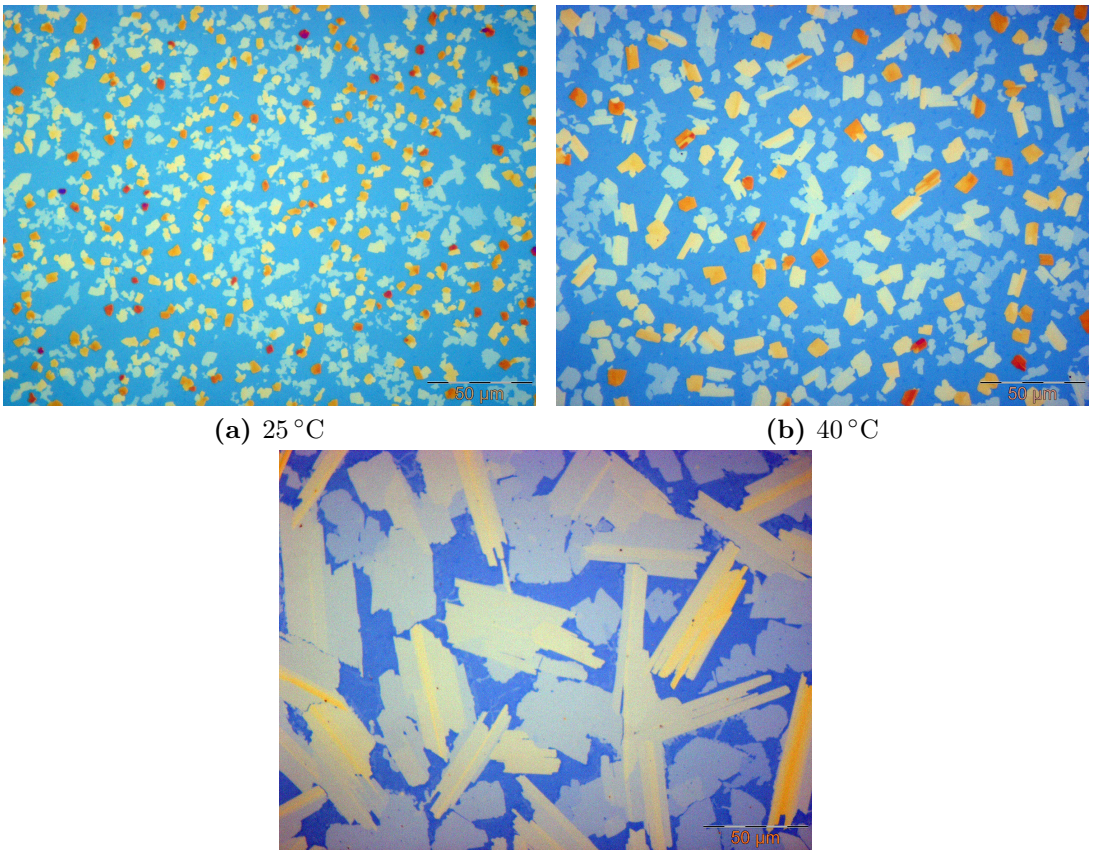

(a) 25 °C **(b)** 40 °C

(c) 55 °C

Figure 4.22.: Comparison of optical microscopy images of 1,88 mg/ml samples spin-coated at (a) 25 °C, (b) 40 °C and (c) 55 °C respectively. The main differences are the larger island size and the change from a compact to a needle like shape.

higher evaporation rate at higher temperatures leaves less time for reorientation but enhances the migration of DOTT molecules on the surface on the other hand. This leads to an increased island size. The 40 °C sample lies in the middle. It has both middle sized and partly compact, partly elongated islands and thus the transition is a continuous one.

X-ray reflectivity

The XRR measurements of three 1,88 mg/ml samples spin-coated at 25 °C, 40 °C and 55 °C in figure 4.23 look very similar at first sight. The most obvious change is found at around 0,9 nm^{-1}. The already known minimum of the fringe from the monolayer is deep at lower temperature but gets less pronounced at higher temperatures. There are two possible reasons for that: First, in the optical microsopy images (figure 4.22) there is less substrate visible in between the islands at higher temperature. This means that only a weaker signal from the monolayer can be detected. However, the signal

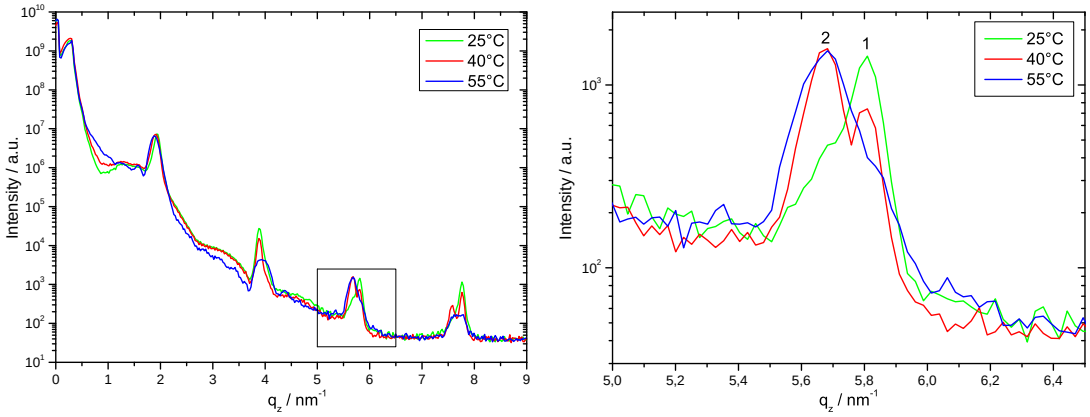

(a) **(b)**

Figure 4.23.: (a) XRR measurements of three 1,88 mg/ml samples spin-coated at 25 °C, 40 °C and 55 °C and (b) zoom into the indicated region. The position of the peak labeled "1" is at 5,81 nm^{-1} which corresponds to a layer thickness of $d = 3,24$ nm. Peak "2" is at 3,68 nm^{-1} and therefore the layer thickness is $d = 3,32$ nm.

Table 4.6.: Position of the peaks in figure 4.23 and the calculated layer thickness. The two peaks belong to different phases, the b- and the s-phase.

Peak	q_z / nm^{-1}	d / nm	Phase
1	5,81	3,24	b
2	5,68	3,32	s

could also be weaker because the monolayer vanishes more and more with increasing temperature.

A zoom into the third peak (figure 4.23b) reveals another interesting change. At room temperature, the peak labeled "1" has its maximum at 5,81 nm^{-1}. A shoulder can be seen on the left side of the peak. At 40 °C, the strongest peak is at the position of this shoulder and the primary peak is found to be weaker. Finally at 55 °C the remaining peak "1" has diminished and only a shoulder on the right side of peak "2" remains. The maximum of peak "2" is found at 5,68 nm^{-1}.

The two peaks belong to different phases. While peak "1" belongs to the already known b-phase, peak "2" gives a layer thickness of $d = 3,32$ nm (see table 4.6). Therefore this phase corresponds to the s-phase in [32]. By increasing the temperature during spin-coating from room temperature to higher temperatures, it can be controlled which phase is formed preferentially. At 25 °C, the sample consists mainly of b-phase islands. At 40 °C, the two phases are observed in similar proportions and at 55 °C, the s-phase is the predominant one.

Grazing incidence X-ray diffraction

The GIXD images in figure 4.24 support the results, found in the last section. The general appearance of the GIXD reciprocal space maps stays the same. The peaks are ordered in three rods, the $(\bar{1}\,\bar{1}\,l)$, the $(\bar{2}\,0\,l)$ and the $(\bar{2}\,\bar{1}\,l)$ rods. The position of the third peak is the same for the b- and the s-phase. The other two can be used to determine, which phase is present. At 25 °C, the b-phase is dominant. With increasing temperature, the $(\bar{1}\,\bar{1}\,l)$ peaks shift from left to right whereas the $(\bar{2}\,0\,l)$ peaks shift from right to left. This implies a change from b- to s-phase.

The linescans in figure 4.25 show the findings in a very clear way. The ratio of the intensities (without background) of the s-phase to the b-phase in the 25 °C sample is 13%. At 40 °C the ratio between the b- and s-phase peaks is 60% and therefore a similar amount of both phases is present. At 55 °C it is 39 %. The s-phase is the predominant one in this sample. From the linescans, the unit cell of the s-phase can be calculated (The specular XRD Bragg peak is used as parameter **c**):

$$\text{s-phase:} \quad \mathbf{a} = 0,54\,\text{nm} \quad \mathbf{b} = 0,77\,\text{nm} \quad \mathbf{c} = 3,32\,\text{nm} \tag{4.5}$$

The volume of the unit cell is then $V_s = 1,390\,\text{nm}^3$ and the density $\rho = 1,13\,\text{g/cm}^3$. These, together with the results in section 4.4 are an indication that thermodynamic effects also play an important role in the selection of the phases. Following Drummy *et al.* [57], the phase with the lower surface energy is going to be the predominant one. The unit cells of both phases are very similar and therefore one can assume that the surface energy of both phases is similar as well. However, there can be a difference in the temperature dependence of the surface energy.

Next to thermodynamics, also kinetic effects have to be considered. It is often the case that the thermodynamic stable phase can not be reached because the transformation is kinetically hindered [8]. In this case, a metastable phase is formed. Spin-coating in general is a fast crystallization process and one would expect that a kinetically favored, metastable phase is preferentially formed, if the samples are spin-coated. An elevated temperature further increases the evaporation rate and therefore the crystallization speed. For DOTT thin films, the crystallization at room temperature seems to be slow enough for the more stable b-phase to be formed but at 55 °C the increased evaporation rate makes the kinetically favored s-phase the predominant one.

Toluene solution

The dependency of the results on the solvent was again checked by preparing samples from a toluene solution. The concentration of the solution was 1,82 mg/ml and hence in the same order as the THF samples in this section. Similar to section 4.3.4, the results indicate a generally worse film quality. In figure 4.26a, the maximum intensity is around 50% lower than the one measured in the THF linescans (figure 4.25). The selection of the different polymorphs at different spin-coating temperatures can also be observed when toluene is used. In figure 4.26b, which is a zoom into the second

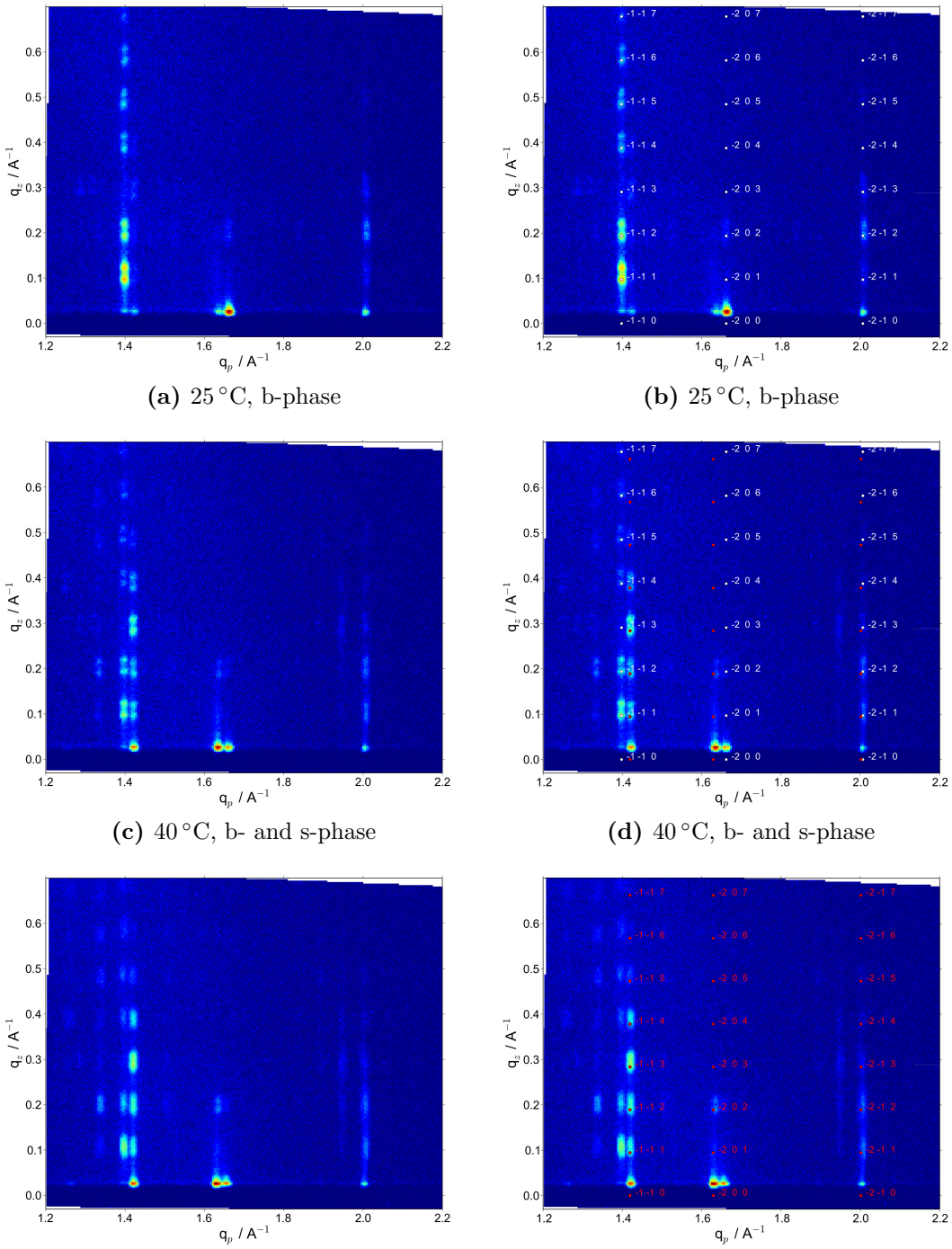

(a) 25 °C, b-phase **(b)** 25 °C, b-phase

(c) 40 °C, b- and s-phase **(d)** 40 °C, b- and s-phase

(e) 55 °C, s-phase **(f)** 55 °C, s-phase

Figure 4.24.: GIXD measurements of three samples spin-coated at different temperautres. (a) 25 °C and (b) indexation with the b-phase (white). (c) 40 °C and (d) indexation with b- (white) and s-phase (red). (e) 55 °C with (f) s-phase indexation (red). With increasing temperature the $(\bar{1}\,\bar{1}\,l)$ peaks shift from left to right whereas the $(\bar{2}\,0\,l)$ peaks shift from right to left.

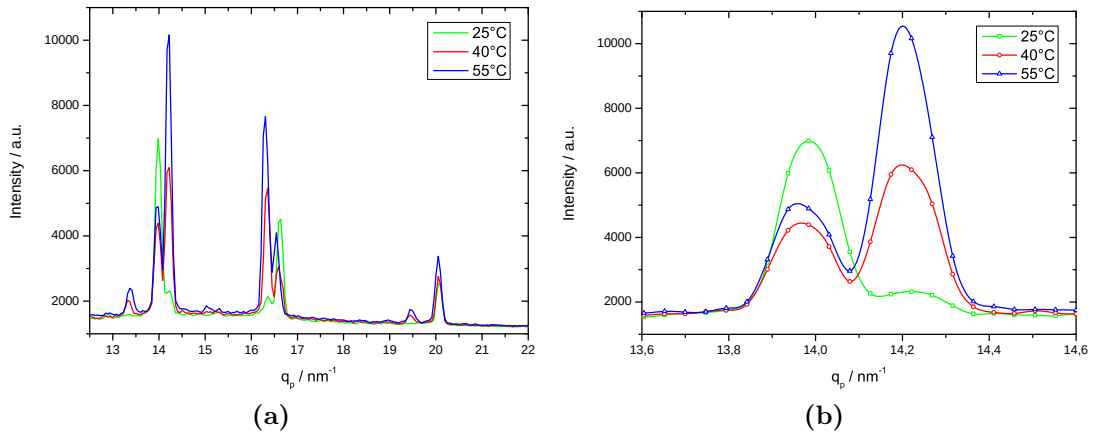

Figure 4.25.: (a) Linescans of the three GIXD reciprocal space maps from figure 4.24 in the region $q_z = 0,1 - 3,5\,\mathrm{nm}^{-1}$. (b) Enlarged region of the first peak. The shift from b- to s-phase is clearly visible.

peak, one can see the shift from the b-phase at room temperature, to a majority of s-phase at 55 °C. However, the amount of s-phase in the 55 °C sample is only slightly higher than the amount of b-phase. And, in contrast to the THF samples, the b-phase is the dominant one at 40 °C. This suggests that the higher boiling point of toluene and therefore the lower evaporation rate enhances the crystallization into the thermodynamic more stable form also at 40 °C and 55 °C.

4.5.2. Annealing

A way to improve the properties of organic thin films is to anneal the samples after film deposition. Especially for liquid crystalline materials this approach is promising because of the ability for self-organization in the liquid crystalline mesophases [58]. DOTT samples were annealed with the DHS 900 at 70 °C (transition to crystal G at 64 °C; see section 1.4.1) followed by cooling to room temperature. The dome was constantly flushed with nitrogen. An interesting effect was found, when the cooling was performed at different rates.

The cycle for the slow cooling rate is depicted in figure 4.27 and consists of the following steps: The samples is heated to 70 °C and kept at this temperature for 20 min. Then it is cooled down with a cooling rate of 1 °C/min. At 55 °C, the cooling is paused for an XRR measurement and then continued to room temperature.

Three samples were chosen for the annealing. A b-phase sample that was spin-coated at 25 °C, one that contains both phases (spin-coated at 40 °C) and an s-phase sample (produced at 55 °C). The results in figure 4.28 reveal that after the annealing cycle, all three samples are b-phase. This shows that even the samples where the s-phase was predominant before annealing, can be changed to b-phase by a transition to the crystal G phase and a slow cooling down to room temperature.

If the s-phase is a kinetically favored phase, a fast cooling rate should result in

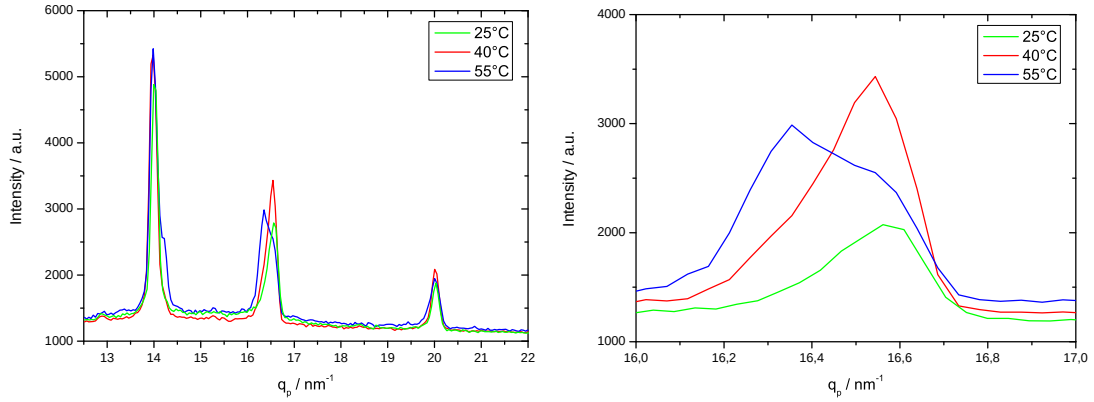

Figure 4.26.: (a) Linescans in the region $q_z = 0,1 - 3,5\,\mathrm{nm}^{-1}$ of three samples spin-coated from 1,82 mg/ml toluene solution at different temperatures. (b) Enlarged region of the second peak. The shift from b- to s-phase is visible.

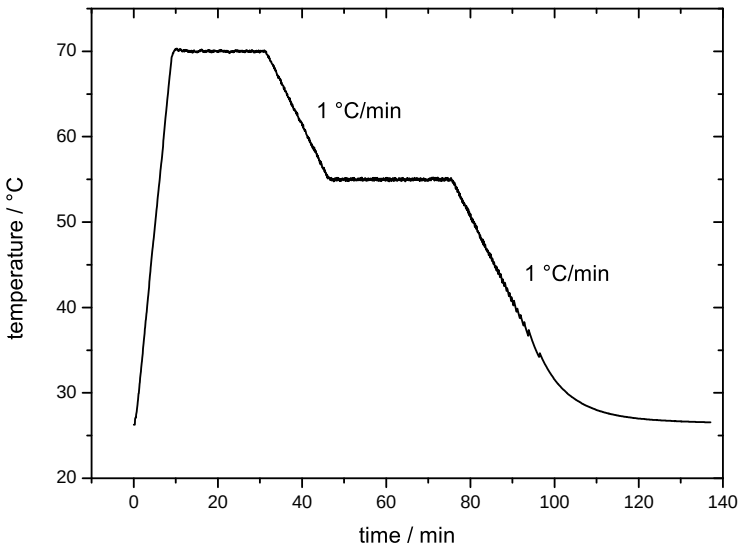

Figure 4.27.: Annealing cycle with slow cooling rate.

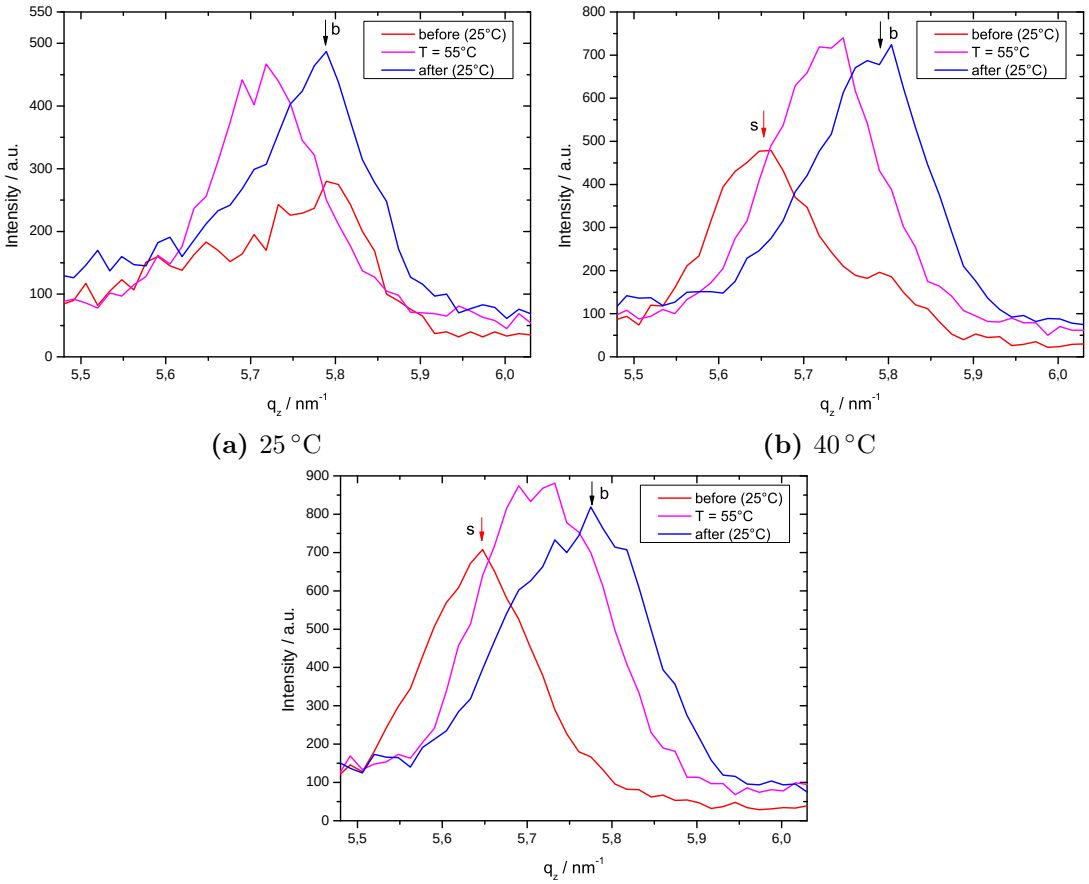

(a) 25 °C **(b)** 40 °C

(c) 55 °C

Figure 4.28.: (0 0 3) Bragg peak position of samples that originally contained (a) mainly b-phase, (b) both phases and (c) mainly s-phase, before and after the annealing cycle with slow cooling

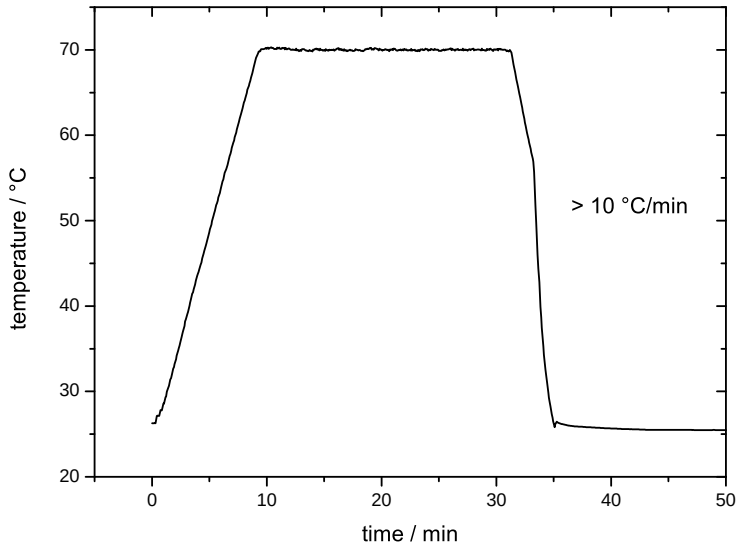

Figure 4.29.: Annealing cycle with fast cooling rate. The sample is first heated to 70 °C with a heating rate of 5 ^{circ}C/min. After 20 min at this temperature, the sample is cooled with a cooling rate of around 10 °C/min.

a higher amount of s-phase in the sample. To verify this theory, the fast cooling cycle in figure 4.29 was used to anneal a sample that had a majority of b-phase after spin-coating at 25 °C.

After the annealing cycle, the predominant phase is the s-phase (but with a still high amount of b-phase). The fast phase transition from the crystal G phase does not leave the molecules enough time to rearrange in the more stable b-phase but the kinetically favored s-phase is preserved (figure 4.30a). Next to the s-phase, a significant amount of the sample remains frozen in the crystal G phase. In figure 4.30b, the crystal G phase peaks are present after the annealing cycle.

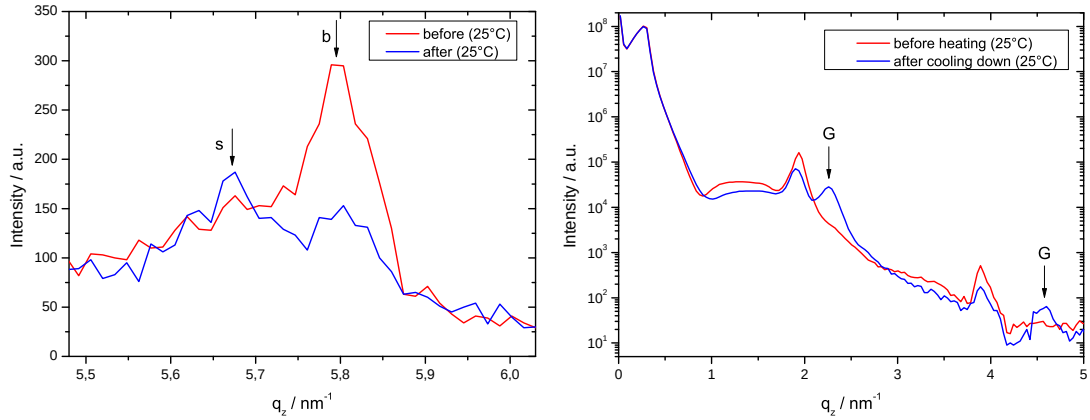

(a) **(b)**

Figure 4.30.: (a) Bragg peak of a sample with the b-phase being the predominant one before the fast annealing cycle. After annealing, the maximum of the peak is shifted to the s-phase position ($5{,}68\,\mathrm{nm}^{-1}$). (b) After annealing, the peaks labeled "G" indicate that parts of the sample are frozen in the crystal G phase.

5. Conclusion

The morphology and the molecular order of DOTT ultrathin films in the range of less than one to around ten molecular layers were investigated by a combined X-ray reflectivity, grazing incidence X-ray diffraction and microscopy study.

It is demonstrated that a closed monolayer is formed on top of the silicone oxide substrate. The molecules arrange in an upright standing position. This first layer crystallizes in a monolayer phase with distinct unit cell parameters which are given, together with the density, in table 5.1. Since it was only found in the first layer, it is called the monolayer or ml-phase. XRR measurements revealed the existence of a thin wetting layer underneath it. In the schematic drawing of the monolayer (figure 5.1), this layer consists of lying DOTT molecules.

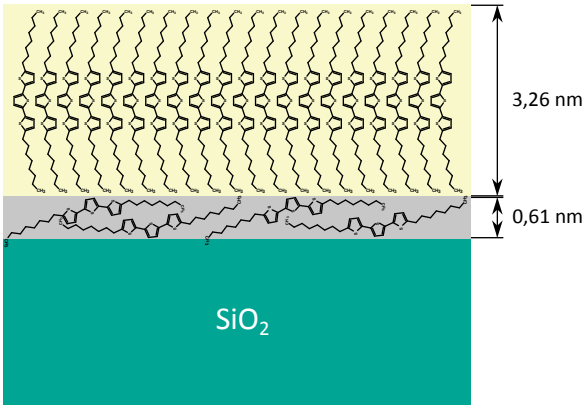

Figure 5.1.: Schematic representation of the first monolayer with underlying wetting layer.

Table 5.1.: Crystallographic unit cell and density of the four phases of DOTT at room temperature.

phase	**a** / nm	**b** / nm	d / nm	ρ / g/cm^3
ml-phase	0,552	0,771	3,26	1,13
s-phase	0,543	0,771	3,32	1,13
b-phase	0,559	0,756	3,24	1,15
single crystal	0,552	0,738	3,18	1,21

On top of this monolayer, DOTT grows in island mode. Samples that were spin-coated at room temperature show a majority of b-phase. By increasing the spin-coating temperature, the s-phase is becoming the predominant one. This is schematically shown in figure 5.2.

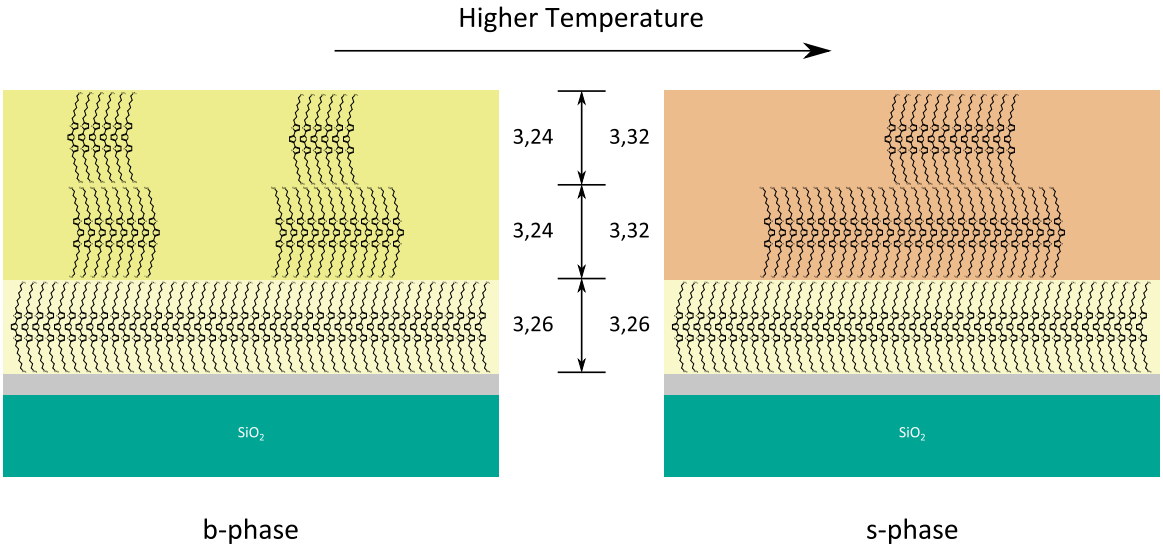

Figure 5.2.: Schematic representation of the b- and the s-phase with subjacent mono- and wetting layer.

It is argued that the s-phase is a kinetically favored phase. The faster crystallization speed at higher temperatures does not leave enough time for the more stable b-phase to be formed throughout the whole sample. The migration of the molecules on the surface is enhanced due to the higher temperature. This leads to a different morphology. The shape of the b-phase islands is compact while the s-phase islands are, despite the faster evaporation, larger and have a more elongated shape. The crystallographic unit cells of the b- and s-phase from Werzer *et al.* [32] were corrected. A comparison of this unit cells with the monolayer and the single crystal phase, including the densities, is given in table 5.1. The density is used as a measure for the thermodynamic stability of the phases. The densities of the ml- and the s-phase are the lowest, which means they are the energetically least favorable. The density of the b-phase lies between the s- and the single crystal phase. It is therefore the most stable surface induced phase at room temperature. However the density of the single crystal phase is again considerably higher.

These results were supported by the annealing experiments. A fast cooling rate results in a metastable film. The molecules freeze mainly into the thermodynamic less but kinetically favorable s-phase. Because of the high cooling rate, parts of the sample remain frozen in the crystal G phase. If the molecules have more time to rearrange into a more stable phase, the b-phase is found as the predominant one after slow cooling.

The same behavior can be found, if the preparation parameters are altered. A different solvent, toluene, does not change the overall appearance of the phases. Fur-

thermore, the first monolayer is not affected by a plasma etched surface. However, the hydrophilic surface influences the following layers, where a higher amount of s-phase is found.

Appendix

A. Aging of the solution

For the results in this work, the solution was prepared directly before the film deposition or the day before. The use of older solution led to unwanted results that are shown subsequently.

The difference is depicted in figure A.1b. Figure A.1a is a 0,33 mg/ml sample made from new solution with the familiar appearance, while figure A.1b shows a 0,35 mg/ml sample made from a two weeks old solution. Small white dots are visible which are mostly situated in the middle of an island. Most likely these white dots serve as nucleation centers for the crystallization. Furthermore some larger white dots can be observed. The AFM images in figure A.2 reveal that the small dots are up to 20 nm high and therefore stick out of the DOTT layer.

The XRR measurement of samples from old and new solution in figure A.3 indicate significant changes of the layer structure. It is supposed that the changes are due to small DOTT crystallites which aggregate in the solution. Heating the solution prior to film fabrication could probably dissolve the particles again. However, these findings were not investigated any further but freshly made solution was used for all samples in the main part of this work.

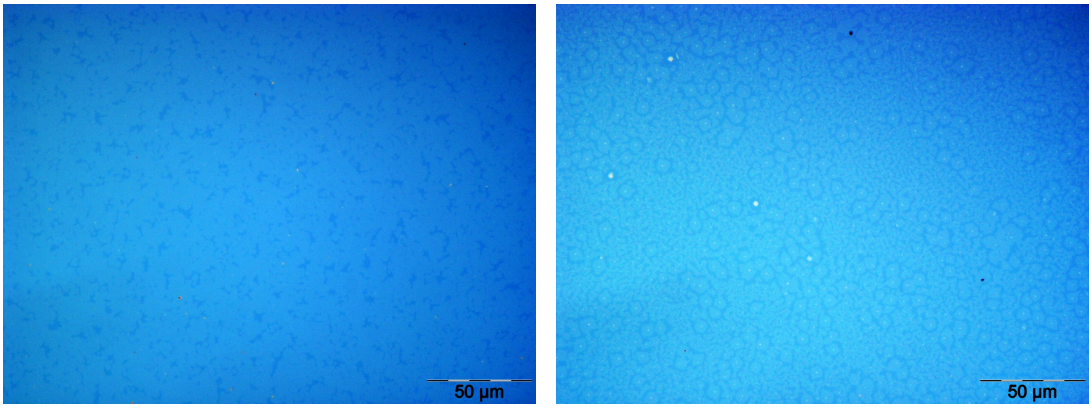

(a) **(b)**

Figure A.1.: Comparison of two optical microscopy images of (a) a 0,33 mg/ml sample made from new and (b) a 0,35 mg/ml sample made from old solution.

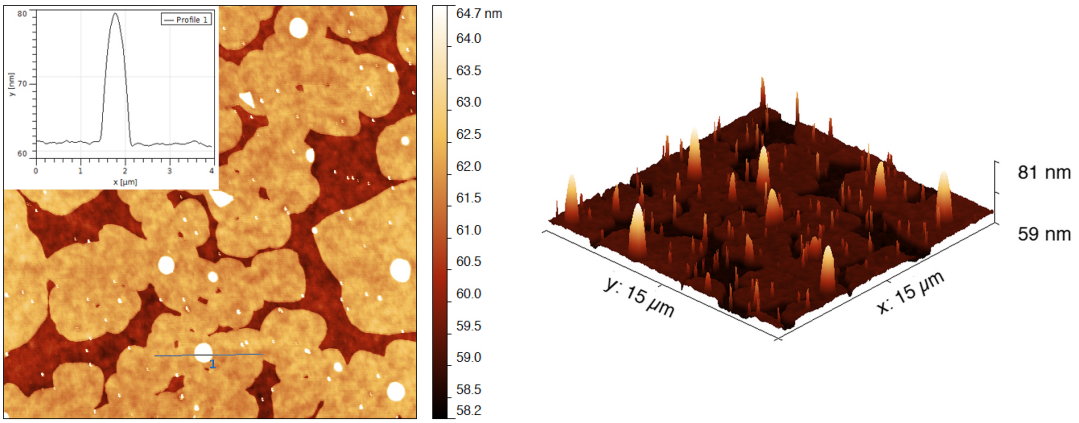

(a) **(b)**

Figure A.2.: Atomic force microscopy image of a sample made from old solution. Large columns stick out of the surface. The inset in (a) shows the height profile of the indicated region "1".

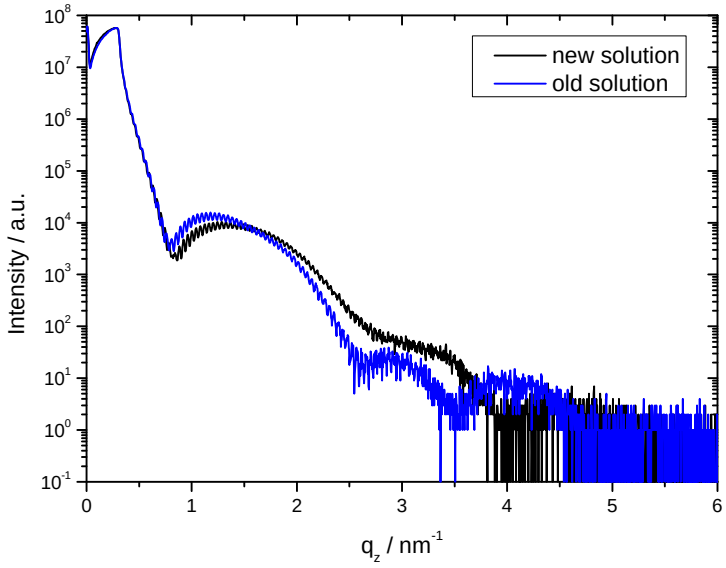

Figure A.3.: Comparison of XRR measurements of two samples. One spin-coated with fresh solution and the other one with a two weeks old solution.

B. Cleaning results

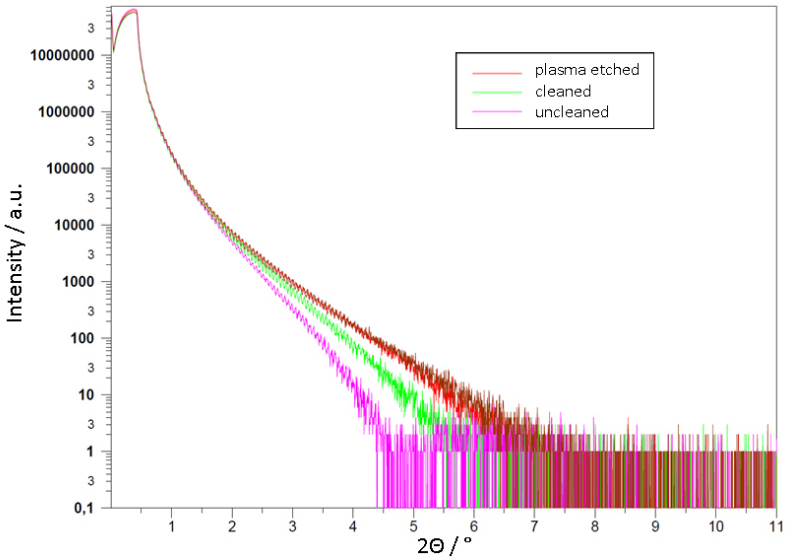

Figure B.1.: Comparison of XRR measurements of differently treated substrates. By cleaning the substrate, the roughness is decreased and the thin layer of unknown origin is reduced. Plasma etching further decreases the roughness.

The results of cleaning the substrates were checked with XRR measurements. In figure B.1, the effect of cleaning is obvious. The roughness is decreased from around 0,5 nm before cleaning to around 0,3 nm after cleaning. Plasma etching further decreases the roughness to a value of 0,2 nm. Furthermore, the XRR curve of the uncleaned substrate indicates a thin layer on top of the silicon oxide (thickness from fit: around 0,6 nm). This layer of unknown origin is almost completely removed by cleaning.

Acknowledgments

First and foremost I would like to thank my supervisor Roland Resel for his guidance and his comments about the work but also for the likeable and pleasant way he manages his group. Next I want to thank the whole "k-Raum" for the mostly productive and always cheerful time.

I would like to thank Prof. Günther Leising and Prof. Roland Fischer, who made the single crystal solution possible. Thank you Quan Shen and Prof. Christian Teichert for the help with the AFM in Leoben. Special thanks to the Universite Libre de Bruxelles: Prof. Michele Sferrazza for the discussions and the input and Prof. Yves Geerts for providing the material. Thank you Ingo Salzmann for the fruitful and interesting time at the HASYLAB in Hamburg. I owe an important debt to Harald Kerschbaumer, Birgit Kunert and Elisabeth Stern from the Institute of Solid State Physics.

Last but not least I want to thank Eva Ellmaier for her patience and encouragement and my family for the support in every moment of my life.

List of abbreviations

a, **b**, **c**	lattice vectors
α, β, γ	angle between lattice vectors
AFM	atomic force microscopy
b-phase	polymorphic phase of DOTT
d	interplanar spacing
DOTT	dioctyl-terthiophene
DSC	differential scanning calorimetry
GIXD	grazing incidence X-ray diffraction
LC	liquid crystal
LCD	liquid crystal display
OFET	organic field effect transistor
OLED	organic light emitting device
OPVC	organic photovoltaic cell
q	scattering vector
s-phase	polymorphic phase of DOTT
SmA, SmB, SmC, ...	smectic mesophases
THF	tetrahydrofuran
XRR	X-ray reflectivity

Bibliography

[1] H. Shirakawa, E. J. Louis, A. G. MacDiarmid, C. K. Chiang, and A. J. Heeger, "Synthesis of electrically conducting organic polymers: Halogen derivatives of polyacetylene, $(CH)_x$," *J. Chem. Soc., Chem. Commun.*, vol. 16, pp. 578–580, 1977.

[2] P. M. Martin, *Handbook of Deposition Technologies for Films and Coatings*. William Andrew, 3rd ed., 2010.

[3] K. Blodgett, "Monomolecular films of fatty acids on glass," *J. Am. Chem. Soc.*, vol. 56, p. 495, 1934.

[4] K. B. Blodgett and I. Langmuir, "Built-up films of barium stearate and their optical properties," *Phys. Rev.*, vol. 51, pp. 964–982, 1937.

[5] W. Ostwald, "Studien über die Bildung und Umwandlung fester Körper," *Zeitschrift f. physik. Chemie*, vol. 22, pp. 289–330, 1897.

[6] J. A. Venables, G. Spiller, and M. Hanbücken, "Nucleation and growth of thin films," *Rep. Prog. Phys.*, vol. 47, pp. 399–459, 1984.

[7] W. Brütting, *Physics of Organic Semiconductors*. Wiley-VCH, 2005.

[8] G. Hlawacek and C. Teichert, "Nucleation and growth of thin films of rod-like conjugated molecules," *Condens. Matter*, vol. 25, 2013.

[9] D. Demus, J. Goodby, G. Gray, H.-W. Spiess, and V. Vill, eds., *Physical Properties of Liquid Crystals*. Wiley-VCH, 1999.

[10] R. Resel, "Soft-Matter-Physik." Lecture notes, 2012.

[11] M.-K. Dai, J.-T. Lian, T.-Y. Lin, M.-C. Chen, Y. Tai, and Y.-F. Chen, "High-performance polythiophene thin-film transistors with nematic liquid crystal modification," *Org. Electron.*, vol. 13, pp. 2229–2234, 2012.

[12] H. Iino and J. Hanna, "Liquid crystalline thin films as a precursor for polycrystalline thin films aimed at field effect transistors," *J. Appl. Phys.*, vol. 109, 2011.

[13] L. Schmidt-Mende, "Self-organized discotic liquid crystals for high-effciency organic photovoltaics," *Science*, vol. 293, pp. 1119–1122, 2001.

[14] M. Baron, "Definitions of basic terms relating to low-molar-mass and polymer liquid crystals," *Pure Appl. Chem.*, vol. 73, pp. 845–895, 2001.

[15] D. Gray, "Introduction to liquid crystals." `http://barrett-group.mcgill.ca/tutorials/liquid_crystal/LC01.htm`. Online; accessed in april 2013.

[16] I. W. Hamley, *Introduction to soft matter*. John Wiley & Sons, 2000.

[17] D. Kahng and M. M. Atalla, "Silicon-silicon dioxide field induced surface devices," in *IRE Solid-State Devices Research Conference, Carnegie Institute of Technology, Pittsburgh, PA*, 1960.

[18] H. Koezuka, A. Tsumura, and T. Ando, "Field-effect transistor with polythiophene thin film," *Synth. Met.*, vol. 18, pp. 699–704, 1987.

[19] J. H. Burroughes, D. D. C. Bradley, A. R. Brown, R. N. Marks, K. Mackay, R. H. Friend, P. L. Burns, and A. B. Holmes, "Light-emitting diodes based on conjugated polymers," *Nature*, vol. 347, pp. 539–541, 1990.

[20] M. A. Baldo, S. Lamansky, P. E. Burrows, M. E. Thompson, and S. R. Forrest, "Very high-efficiency green organic light-emitting devices based on electrophosphorescence," *Appl. Phys. Lett.*, vol. 75, pp. 4–6, 1999.

[21] "Toshiba develops world's first 260,000-color polymer organic light emitting display." `http://barrett-group.mcgill.ca/tutorials/liquid_crystal/LC01.htm`, 2001. Online; accessed in april 2013.

[22] Z. Bao and J. Locklin, eds., *Organic Field-Effect Transistors*. CRC Press, 2007.

[23] C. D. Dimitrakopoulos and D. J. Mascaro, "Organic thin-film transistors: A review of recent advances," *IBM J. Res. & Dev.*, vol. 45, pp. 11–27, 2001.

[24] V. C. Sundar, J. Zaumseil, V. Podzorov, E. Menard, R. L. Willett, T. Someya, M. E. Gershenson, and J. A. Rogers, "Elastomeric transistor stamps: Reversible probing of charge transport in organic crystals," *Science*, vol. 303, pp. 1644–1646, 2004.

[25] S. F. Nelson, Y. Y. Lin, D. J. Gundlach, and T. N. Jackson, "Temperature-independent transport in high-mobility pentacene transistors," *Appl. Phys. Lett.*, vol. 72, pp. 1854–1856, 1998.

[26] M. Halik, H. Klauk, U. Zschieschang, G. Schmid, S. Ponomarenko, S. Kirchmeyer, and W. Weber, "Relationship between molecular structure and electrical performance of oligothiophene organic thin film transistors," *Adv. Mater.*, vol. 15, pp. 917–922, 2003.

[27] C. D. Dimitrakopoulos, A. R. Brown, and A. Pomp, "Molecular beam deposited thin films of pentacene for organic field effect transistor applications," *J. Appl. Phys.*, vol. 80, pp. 2501–2508, 1996.

[28] B. Wedl, R. Resel, G. Leising, B. Kunert, I. Salzmann, M. Oehzelt, N. Koch, A. Vollmer, S. Duhm, O. Werzer, G. Gbabode, M. Sferrazza, and Y. Geerts, "Crystallisation kinetics in thin films of dihexyl-terthiophene: The appearance of polymorphic phases," *RSC Adv.*, vol. 2, pp. 4404–4414, 2012.

[29] M. Funahashi and J. Hanna, "High ambipolar carrier mobility in self-organizing terthiophene derivative," *Appl. Phys. Lett.*, vol. 76, pp. 2574–2576, 2000.

[30] J. Leroy, J. Levin, S. Sergeyev, and Y. Geerts, "Practical one-step synthesis of symmetrical liquid crystalline dialkyloligothiophenes for molecular electronic applications," *Chem. Lett.*, vol. 35, pp. 166–167, 2006.

[31] V. Lemaur, S. Bouzakraoui, Y. Olivier, P. Brocorens, C. Burhin, J. El Beghdadi, A. Martin-Hoyas, A. M. Jonas, D. A. Serban, A. Vlad, N. Boucher, J. Leroy, M. Sferrazza, P. O. Mouthuy, S. Melinte, S. Sergeev, Y. Geerts, R. Lazzaroni, J. Cornil, and B. Nysten, "Structural and charge-transport properties of a liquid-crystalline α,ω-disubstituted thiophene derivative: A joint experimental and theoretical study," *J. Phys. Chem. C*, vol. 114, pp. 4617–4627, 2010.

[32] O. Werzer, N. Boucher, J. P. De Silva, G. Gbabode, Y. H. Geerts, O. Konovalov, A. Moser, J. Novak, R. Resel, and M. Sferrazza, "Interface induced crystal structures of dioctyl-terthiophene thin films," *Langmuir*, vol. 28, pp. 8530–8536, 2012.

[33] J. Als-Nielsen and D. McMorrow, *Elements of Modern X-Ray Physics*. John Wiley & Sons, 2001.

[34] M. Birkholz, *Thin Film Analysis by X-Ray Scattering*. Wiley-VCH, 2006.

[35] L. Spieß, R. Schwarzer, H. Behnken, and G. Teichert, *Moderne Röntgenbeugung*. B. G. Teubner Verlag, 2005.

[36] C. Kittel, *Introduction to solid state physics*. John Wiley & Sons, 2005.

[37] M. Tolan, *X-Ray Scattering from Soft-Matter Thin Films*. Springer-Verlag Berlin Heidelberg, 1999.

[38] H. Kiessig, "Interferenzen von Röntgenstrahlen an dünnen Schichten," *Ann. Phys.*, vol. 10, pp. 769–788, 1931.

[39] L. G. Parratt, "Surface studies of solids by total reflection of x-rays," *Phys. Rev.*, vol. 95, pp. 359–369, 1954.

[40] M. Yasaka, "X-ray reflectivity measurement," *The Rigaku Journal*, vol. 26, pp. 1–9, 2010.

[41] M. Neuschitzer, "Grazing incidence in-plane x-ray diffraction on ultra-thin organic films using standard laboratory equipment," Master's thesis, Graz University of Technology, 2012.

[42] A. Moser, *Crystal Structure Solution Based on Grazing Incidence X-ray Diffraction*. PhD thesis, Graz University of Technology, 2012.

[43] I. Salzmann, D. Nabok, M. Oehzelt, S. Duhm, A. Moser, G. Heimel, P. Puschnig, C. Ambrosch-Draxl, J. Rabe, and N. Koch, "Structure solution of the 6,13-pentacenequinone surface-induced polymorph by combining x-ray diffraction reciprocal-space mapping and theoretical structure modeling," *Cryst. Growth Des.*, vol. 11, pp. 600–606, 2011.

[44] G. Binnig, C. Quate, and C. Gerber, "Atomic force microscope," *Phys. Rev. Lett.*, vol. 56, pp. 930–933, 1986.

[45] N. Jalili and K. Laxminarayana, "A review of atomic force microscopy imaging systems: Application to molecular metrology and biological sciences," *Mechatronics*, vol. 14, pp. 907–945, 2004.

[46] T. Young, "An essay on the cohesion of fluids," *Phil. Trans. R. Soc. Lond.*, vol. 95, pp. 65–87, 1805.

[47] D. Owens and R. Wendt, "Estimation of the surface free energy of polymers," *J. Appl. Polym. Sci.*, vol. 13, pp. 1741–1747, 1969.

[48] W. Rabel, "Einige Aspekte der Benetzungstheorie und ihre Anwendung auf die Untersuchung und Veränderung der Oberlächeneigenschaften von Polymeren," *Farbe und Lacke*, vol. 77, pp. 997–1005, 1971.

[49] M. Neuschitzer, A. Moser, A. Neuhold, J. Kraxner, B. Stadlober, M. Oehzelt, I. Salzmann, R. Resel, and J. Novák, "Grazing-incidence in-plane x-ray diffraction on ultra-thin organic films using standard laboratory equipment," *J. Appl. Crystallogr.*, vol. 45, pp. 367–370, 2012.

[50] A. Neuhold, J. Novák, H. Flesch, A. Moser, T. Djuric, L. Grodd, S. Grigorian, U. Pietsch, and R. Resel, "X-ray radiation damage of organic semiconductor thin films during grazing incidence diffraction experiments," *Nucl. Intrum. Meth. B*, vol. 284, pp. 64–68, 2012.

[51] D. Nečas and P. Klapetek, "Gwyddion: An open-source software for SPM data analysis," *Cent. Eur. J. Phys.*, vol. 10, pp. 181–188, 2012.

[52] M. Dohr, "Temperature induced effects of dioctyl-benzothieno-benzothiophene thin films," Master's thesis, Graz University of Technology, 2012.

[53] T. Threlfall, "Crystallisation of polymorphs: Thermodynamic insight into the role of solvent," *Org. Process Res. Dev.*, vol. 4, pp. 384–390, 2000.

[54] A. Pichler, "Crystal structure resolution from thin films," Master's thesis, Graz University of Technology, 2013.

[55] S. Verlaak, S. Steudel, P. Heremans, D. Janssen, and M. S. Deleuze, "Nucleation of organic semiconductors on inert substrates," *Phys. Rev. B: Condens. Matter*, vol. 68, pp. 1954091–19540911, 2003.

[56] B. Lang, "Oberflächenenergie von {100} Silizium-Wafern nach O_2 Plasmabehandlung." Bachelor's thesis, Graz University of Technology, 2012.

[57] L. F. Drummy and D. C. Martin, "Thickness driven orthorhombic to triclinic phase transformation in pentacene thin films," *Adv. Mater.*, vol. 17, pp. 903–907, 2005.

[58] M. O'Neill and S. M. Kelly, "Ordered materials for organic electronics and photonics," *Adv. Mater.*, vol. 23, pp. 566–584, 2011.